博士論文

Theoretical study of high-intensity hadron beam stability in linear and circular accelerators

(線形および円形加速器中の
大強度ハドロンビームの
安定性に関する理論的研究)

広島大学大学院先進理工系科学研究科
量子物質科学専攻
小島　邦洸

2023年3月

Contents

Abstract

Recent progress in accelerator technologies has made it feasible to produce high-power and/or high-brightness hadron beams for diverse applications. As a result, mutual Coulomb interaction among accelerated particles is playing a crucial role in the beam stability. A detailed understanding of collective effects induced by the space-charge potential is indispensable to make a reliable design of any next-generation hadron machine. Such information is also essential to achieve the performance improvement of high-intensity accelerators currently operating around the world. The purpose of the present work is to elucidate the basic mechanisms of resonant instabilities expected to occur in high-intensity hadron beams. Emphasis is placed upon two main subjects described in detail in Chapter 3 and Chapter 4. The first two chapters are for providing fundamental beam-dynamics information that will help in understanding the contents of the following chapters.

In Chapter 3, we pay attention to resonant instabilities in circular accelerators. Since the beam goes through a huge number of lattice periods, even a weak nonlinear resonance may affect the beam stability. The machine operating point must be chosen carefully in betatron tune space to avoid dangerous stop bands of various resonances. For this purpose, we need to predict the locations of those stop bands, taking the space-charge effect into account. It is particularly important to consider the beam behavior in a self-consistent manner because the motions of individual particles are no longer independent at high density but rather correlated through the Coulomb potential. The so-called "incoherent resonance condition" and "necktie diagram", commonly used in the community to look for an optimum operating point, are not self-consistent. We should, therefore, be careful in using these conventional concepts for the optimization of machine parameters. In fact, the main body (core) of the beam turns out to be stable even though the core particles satisfy the incoherent resonance condition.

According to the self-consistent analytic theory developed by Okamoto and Yokoya for one-dimensional (1D) sheet beam, the core of an intense beam matched to an alternating-gradient (AG) lattice may become unstable when the tune of a coherent core oscillation mode is close to half integers. We here empirically generalize their 1D "coherent resonance condition" to predict the core stability of a coasting beam. The proposed two-dimensional (2D) resonance condition is applicable to a long bunch typical in modern high-intensity hadron rings. A self-consistent simulation technique, namely, the particle-in-cell (PIC) code "WARP" is employed to check the validity of the 2D condition. It is found that the present resonance theory can explain systematic PIC simulation data fairly well. We also show that it is possible to suppress a specific difference resonances strongly by adjusting the ratio of initial horizontal and vertical emittances to a specific value. Based on the 2D coherent resonance condition, a new type of stability tune diagram is constructed to visualize the preferable operating areas in betatron tune space. The new diagram reveals not only the distribution of coherent resonance bands where the beam core may be affected seriously but also incoherent resonance regions where large amplitude particles

in the beam tail may become unstable. As an example, we take the lattice design of the rapid cycling synchrotron (RCS) at the Japan Proton Accelerator Research Complex (J-PARC) and demonstrate that our stability chart is consistent with the current RCS operating condition.

In Chapter 4, we explore the stability of intense short hadron bunches propagating through linear accelerators. Unlike in the case of circular machines, beams in linacs pass through only a limited number of AG focusing periods. They, however, have much higher density in phase space, so space-charge effects can be very severe even in a short timescale. Moreover, the bunch shape is ellipsoidal or even spherical due to the strong longitudinal focusing force, which makes the role of synchrotron oscillation more important. Further generalization of the 2D resonance theory in Chapter 3 is then necessary to include the effect of synchrobetatron coupling as well as the synchrotron resonance. We thus introduce the three-dimensional (3D) version of the coherent resonance condition in this chapter.

Extra caution is required in the linac situation where the external potential generated by beam focusing magnets and accelerating gaps is not strictly periodic as in the case of storage rings. The operating betatron and synchrotron tunes per unit AG cell are no longer fixed but move in the tune space as the beam is accelerated. We employ the 3D PIC code "IMPACT" to incorporate these complications and apply it to investigate the stability of high-intensity proton beams in the drift-tube linac (DTL) at J-PARC. A few possible sources of the emittance growth actually observed in the DTL are suggested and studied in detail.

In addition to IMPACT simulations with the exact design parameters of the J-PARC DTL, a systematic numerical study is performed over a wide parameter range, based on an analytic model assuming the most typical Alvarez-type DTL structure. It is confirmed that a serious emittance exchange occurs when the operating point crosses a low-order synchrobetatron difference resonance band. Such an emittance exchange effect can, however, be weakened significantly by choosing a proper ratio of the initial emittances of the three directions, similarly to the 2D case discussed in the previous chapter. The equipartitioned linac design is found to automatically achieve the magic emittance ratio for the suppression of low-order difference resonances, which broadens the usable operating area in the tune space.

Acknowledgements

I express sincere thanks to my supervisor Prof. Hiromi Okamoto for his continuous support and guidance. I would like to thank Dr. Katsuhiro Moriya for his helpful discussions and comments on my study. I also would like to thank Yuji Tokashiki for his valuable discussion on beam physics issues. I wish to thank Dr. Kei Fukushima and Dr. Hiroyuki Harada for their useful discussion. I received generous support from Dr. Hiroyuki Higaki and other members of the Beam Physics Group of Hiroshima University. A part of the numerical simulations in Chapter 4 was performed with the supercomputer at Research Institute for Information Technology, Kyushu University.

Chapter 1

Basic theory

1.1 Hamiltonian formalism in the Frenet-Serret coordinate system

The motion of the charged particle can be divided into a reference orbit and the small amplitude displacement around it. It is convenient to define the spatial coordinate along the reference orbit. Thus the coordinate system illustrated in Fig. 1.1, which is referred to as the "Frenet-Serret system", is adopted in this paper [1]. The particle position vector is given by

$$\boldsymbol{u} = x\boldsymbol{n} + y\boldsymbol{b} + s\boldsymbol{t}, \tag{1.1}$$

where x and y are betatron coordinates. $\boldsymbol{n}$, $\boldsymbol{b}$, and $\boldsymbol{t}$ are principal normal unit vector, binormal unit vector, and tangent unit vector to the reference orbit respectively. s denotes the length measured along the reference orbit from an initial point. Then the Lagrangian using time t as the independent variable is given by

$$L_t = -mc^2\sqrt{1 - \left(\frac{1}{c}\frac{d\boldsymbol{u}}{dt}\right)^2} + q\left(\boldsymbol{A}\cdot\frac{d\boldsymbol{u}}{dt} - \phi\right), \tag{1.2}$$

where m and q are the rest mass and charge of the particle. c is the speed of light in the vacuum. $\boldsymbol{A}$ is the sum of $\boldsymbol{A}^{(\mathrm{sc})}$ comes from the beam current and $\boldsymbol{A}^{(\mathrm{mag})} = (A_x, A_y, A_s)$ comes from accelerator components, and ϕ denotes the scalar potential. In general, the transversal velocities of the particle dx/dt and dy/dt are much smaller than longitudinal velocity ds/dt, and we

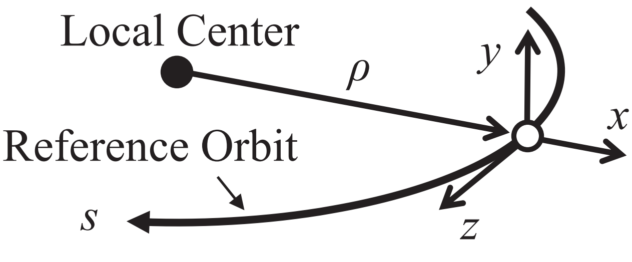

Figure 1.1: The Frenet-Serret system

can approximate the vector potential by $\boldsymbol{A}^{(\mathrm{sc})} = \beta_{\mathrm{s}}\phi_{\mathrm{sc}}\boldsymbol{t}$ where β_{s} and ϕ_{sc} are Lorentz factor and scalar potential generated by particles' charge. Then the total vector potential becomes $\boldsymbol{A} = (A_x, A_y, A_s + \beta_{\mathrm{s}}\phi_{\mathrm{sc}})$.

It is often useful to take s instead of t as the independent variable because the distribution of $\boldsymbol{A}^{(\mathrm{mag})}$ are spatially fixed. The new Lagrangian can be written

$$L_s \equiv L_t\frac{dt}{ds} = -mc^2\sqrt{\left(\frac{dt}{ds}\right)^2 - \left(\frac{1}{c}\frac{d\boldsymbol{u}}{ds}\right)^2} + q\left(\boldsymbol{A}\cdot\frac{d\boldsymbol{u}}{ds} - \phi_{\mathrm{sc}}\frac{dt}{ds}\right). \tag{1.3}$$

Ignoring the torsion of the reference orbit, $d\boldsymbol{u}/ds$ can be written

$$\frac{d\boldsymbol{u}}{ds} = \frac{dx}{ds}\boldsymbol{n} + \frac{dy}{ds}\boldsymbol{b} + \left(1 + \frac{x}{\rho}\right)\boldsymbol{t}, \tag{1.4}$$

where ρ is the local curvature of the reference orbit.

According to the least action therm, Hamiltonian derived from Eq. (1.3) is

$$\begin{aligned} &H(x, y, t, p_x, p_y, p_t; s) = \\ &-\left(1 + \frac{x}{\rho}\right)\sqrt{\left(\frac{p_t + q\phi_{\mathrm{sc}}}{c}\right)^2 - mc^2 - (p_x - qA_x)^2 - (p_y - qA_y)^2} - q\left(1 + \frac{x}{\rho}\right)(A_s + \beta_{\mathrm{s}}\phi_{\mathrm{sc}}). \end{aligned} \tag{1.5}$$

Note that the longitudinal canonical coordinate is no longer the spacial coordinate z, and the conjugate momentum p_t is equal to just the negative of the total energy of the particle. The canonical momentums p_x and p_y are usually much smaller than the total kinetic momentum $p = \sqrt{(p_t + q\phi_{\mathrm{sc}})^2/c^2 - m^2c^2}$. Assuming $|p_x/p| \ll 1$ and $|p_y/p| \ll 1$, we can expand the first term on the right-hand side of Eq. (1.5) as

$$H \approx -\left(1 + \frac{x}{\rho}\right)\left[p - \frac{(p_x - qA_x)^2 + (p_y - qA_y)^2}{2p} + q(A_s + \beta_{\mathrm{s}}\phi_{\mathrm{sc}})\right]. \tag{1.6}$$

Here, we transform the longitudinal canonical momentum from p_t to the energy deviation ΔE for later convenience. If we use the design energy E_0, the energy deviation can be written by $\Delta E = -p_t - E_0$. The canonical transformation from (t, p_t) to $(t', \Delta E)$ is realized by the generating function

$$F_1(t, -\Delta E) = -(\Delta E + E_0)t. \tag{1.7}$$

And the new Hamiltonian is

$$\begin{aligned} &\tilde{H}(x, y, t', p_x, p_y, \Delta E; s) \approx \\ &\left(1 + \frac{x}{\rho}\right)\left[\frac{(p_x - qA_x)^2 + (p_y - qA_y)^2}{2p_0} - qA_s + \frac{q\phi_{\mathrm{sc}}}{\beta_{\mathrm{s}}c\gamma_{\mathrm{s}}^2} - \frac{\Delta E}{\beta_{\mathrm{s}}c} + \frac{1}{2p_0}\left(\frac{\Delta E}{\beta_{\mathrm{s}}c\gamma_{\mathrm{s}}}\right)^2\right], \end{aligned} \tag{1.8}$$

where $p_0 \equiv m\beta_\mathrm{s}\gamma_\mathrm{s}c$ is design moment. The following relation is used to derive Eq. (1.8).

$$\begin{aligned} p &\approx p_0\sqrt{1+\frac{2p_0}{p_0^2c^2}(\Delta E - q\phi_\mathrm{sc}) + \frac{1}{p_0^2c^2}(\Delta E - q\phi_\mathrm{sc})^2} \\ &\approx p_0 + \frac{1}{\beta_\mathrm{s}c}(\Delta E - q\phi_\mathrm{sc}) - \frac{\Delta E^2}{2p_0(\beta_\mathrm{s}c\gamma_\mathrm{s})^2}\,. \end{aligned} \tag{1.9}$$

1.2 Multipole expansion of magnetic components

Ideally, only the longitudinal vector potential is enough to describe Lorentz forces from multipole magnets, and we assume $\boldsymbol{A}^{(\mathrm{mag})} = A_s\boldsymbol{t}$. Let us consider the expansion of magnetic components in a power series in the betatron coordinates. Using time-independent Maxwell's equations in a vacuum $\nabla \times \boldsymbol{B} = 0$ and $\boldsymbol{B} = \nabla \times \boldsymbol{A}$, we have

$$\nabla^2 A_s = 0. \tag{1.10}$$

In 2D cylindrical coordinates (r, θ), the general solution of A_s can be obtained through power series expansion in r as follows.

$$\begin{aligned} A_s(r,\theta) = &\sum_{n=1}^{\infty}({}_1d_n\cos n\theta +{}_2\, d_n\sin n\theta)\left({}_3d_nr^n + \frac{{}_4d_n}{r^n}\right) \\ &+({}_1d_0\theta +{}_2\, d_0)({}_3d_0\log r +{}_4\, d_0), \end{aligned} \tag{1.11}$$

where ${}_1d_n, {}_2\, d_n, {}_3\, d_n$, and ${}_4d_n$ $(n = 0, 1, 2...)$ are constants. Here we are interested in the components that do not diverge at $r = 0$ and keep only them to obtain

$$A_s(r,\theta) = \sum_{n=1}^{\infty}\left(\frac{r}{r_0}\right)^n(a_n\cos n\theta + b_n\sin n\theta), \tag{1.12}$$

where a_n and b_n are nth multipole coefficients. r_0 is a normalization constant. The components with a_n are called the normal component, and the components with b_n are called the skew component. The low-order components obtained from Eq. (1.12) are listed in Table 1.1. The lowest ($n = 1$) and second lowest ($n = 2$) terms in Eq. (1.12) are essential in any accelerators. The former is a source of dipole fields that are used to guide the reference orbit. It is also used to make a closed orbit in circular accelerators. The latter is a source of quadrupole fields that focus or defocus the beam in the transverse plane. Especially, the normal quadrupole field that focuses the beam in the horizontal direction is "focusing-quadrupole", and the contrary one is "defocusing-quadrupole". The so-called "alternating gradient (AG) focusing" is realized by alternately aligning the focusing-quadrupole and defocusing-quadrupole.

1.3 Linear theory of transverse dynamics

In this section, we explain the basic linear theory of beam dynamics constructed by Courant and Snyder with zero self field ($\phi_\mathrm{sc} = 0$) [2]. Then the motion of charged particles in an accelerator can be separated in the transverse and longitudinal direction, and we focus on only the former

Table 1.1: Low-order magnetic components

order	Normal component	Skew component
1	$a_1 x/r_0$	$b_1 y/r_0$
2	$a_2(x^2 - y^2)/2r_0^2$	$b_2(xy)/r_0^2$
3	$a_3(x^3 - 3xy^2)/6r_0^3$	$b_3(y^3 - 3x^2 y)/6r_0^3$
4	$a_4(x^4 - 6x^2y^2 + y^4)/24r_0^4$	$b_4(x^3 y - xy^3)/6r_0^4$

one for simplicity. Considering the general case of AG focusing lattice, the Hamiltonian of the transverse degree of freedom can be obtained from Eq. (1.8)

$$H(x, y, p_x, p_y; s) = \frac{p_x^2 + p_y^2}{2} + \frac{K(s)}{2}(x^2 - y^2), \tag{1.13}$$

where $K(s)$ is the s-depedent function determined by the lattice structure and is periodic with lattice period L; namely $K(s + L) = K(s)$. In Eq. (1.13) the canonical moments and the Hamiltonian are normalized as $\tilde{H}/p_0 \longrightarrow H,\ p_{x(y)}/p_0 \longrightarrow p_{x(y)}$. Here we introduce the phase coordinate $\psi_{x(y)}$ and the action $J_{x(y)}$ for a better understanding of the particle motion governed by the Hamiltonian. The generating function F_2 of the transformation can be written as

$$F_2(x, y, \psi_x, \psi_y; s) = -\frac{x^2}{2\beta_x}\left(\tan\psi_x - \frac{1}{2}\frac{d\beta_x}{ds}\right) - \frac{y^2}{2\beta_y}\left(\tan\psi_y - \frac{1}{2}\frac{d\beta_y}{ds}\right), \tag{1.14}$$

where β_x satisfies

$$\frac{1}{2}\frac{d^2\beta_x}{ds^2} + K\beta_x - \frac{1}{\beta_x}\left[1 + \left(\frac{1}{2}\frac{d\beta_x}{ds}\right)^2\right] = 0, \tag{1.15}$$

and similarly for β_y except for the sign of $K(s)$. Equation (1.14) gives us the relation

$$\begin{cases} x = \sqrt{2J_x\beta_x}\cos\psi_x \\ p_x = -\sqrt{\dfrac{2J_x}{\beta_x}}\left(\sin\psi_x - \dfrac{1}{2}\dfrac{d\beta_x}{ds}\cos\psi_x\right). \end{cases} \tag{1.16}$$

It can be interpreted as a pseudo harmonic oscillation, which is called “betatron oscillation”. Then $\psi_{x(y)}$ represents the phase of the betatron oscillation. $J_{x(y)}$ is equal to the phase space area enclosed by the torus of a particle. Using Eq. (1.14), we find the new Hamiltonian

$$\hat{H}(\psi_x, \psi_y, J_x, J_y; s) = \frac{J_x}{\beta_x} + \frac{J_y}{\beta_y}. \tag{1.17}$$

$J_{x(y)}$ is invariant because the new Hamiltonian is independent of $\psi_{x(y)}$ [3]. Figure 1.2 shows the schematics of the torus for a particle. In the figure, $\alpha_{x(y)}$ and $\gamma_{x(y)}$ are defined by

$$\alpha_x = -\frac{1}{2}\frac{d\beta_x}{ds}, \quad \gamma_x = \frac{1 + \alpha_x^2}{\beta_x}. \tag{1.18}$$

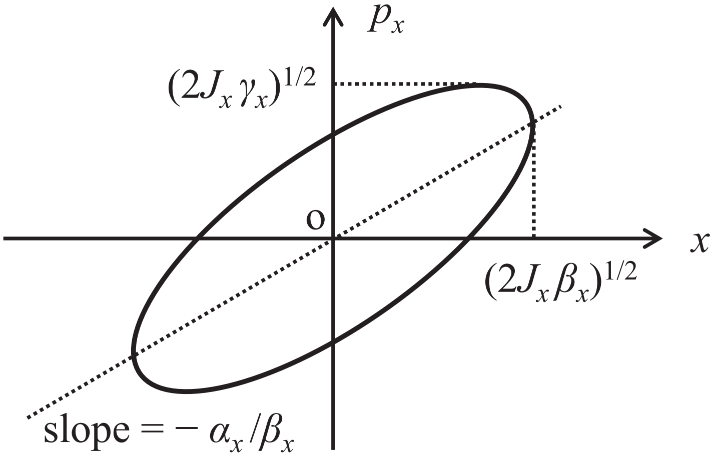

Figure 1.2: A torus for a particle in x-p_x phase space with action J_x.

The functions $\beta_{x(y)}$, $\alpha_{x(y)}$, and $\gamma_{x(y)}$ are called "Twiss parameters" and are often used in beam dynamics. We also obtain the canonical equation $d\psi_{x(y)}/ds = 1/\beta_{x(y)}$. The relation suggests that the phase advance of the betatron oscillation per length is given by $1/\beta_{x(y)}$, and we can define the "tune $\nu_{x(y)}$" per one AG period length by

$$\nu_x = \frac{1}{2\pi}\int_{s_0}^{s_0+L}\frac{ds}{\beta_x}, \tag{1.19}$$

where s_0 is a constant. The important point is that $\nu_{x(y)}$ is independent of the amplitude of the particle; in other words, the tune can be defined for the whole beam. In addition, the tune is the oscillation frequency of the betatron oscillation and is essential to discuss the resonant instability in accelerators. In this paper, the tune with zero self field is especially called "bare tune " and is represented by $\nu_{0x(0y)}$.

1.4 Single-particle resonance conditions

The periodic nature of particle accelerators is the source of various resonant instabilities. Since the resonant instabilities can degrade the beam quality seriously in some cases, much effort was devoted to understanding and avoiding them. If we consider the single-particle case where no Coulomb repulsive force acts, the classical resonance condition derived by Courant and Snyder for circular accelerators given by [2]

$$k\nu_{0x} + \ell\nu_{0y} = n, \tag{1.20}$$

where k, ℓ, and n are integers, and the order of the resonance is $m \equiv |k| + |\ell|$. This is one of the most basic and important formulas in beam dynamics and can be found in any textbooks [1,4–6]. The resonance is driven by external fields whose sources are mainly misalignments of the magnets and nonlinear multipole magnets.

Let us consider the feature of the resonances. The starting point of single-particle resonance theory is the Hamiltonian of Eq. (1.17) with a nonlinear driving term

$$\hat{H}(\psi_x, \psi_y, J_x, J_y; s) = \frac{J_x}{\beta_x} + \frac{J_y}{\beta_y} + K_{\mathrm{p}}(s)(2J_x\beta_x)^{|k|/2}(2J_y\beta_y)^{|\ell|/2}\cos^{|k|}\psi_x \cos^{|\ell|}\psi_y, \tag{1.21}$$

where $K_{\mathrm{p}}(s)$ is periodic perturbation with the same period of $K(s)$. We assume that the amplitude of $K_{\mathrm{p}}(s)$ is small enough not to distort the non-perturbated state. It is useful to make the phase advance smoothed by using the generating function

$$F_3(\psi_x, \psi_y, \bar{J}_x, \bar{J}_y) = \left(\psi_x - \int^s \frac{ds}{\beta_x} + \nu_{0x}\theta\right)\bar{J}_x + \left(\psi_y - \int^s \frac{ds}{\beta_y} + \nu_{0y}\theta\right)\bar{J}_y, \tag{1.22}$$

and the Hamiltonian becomes

$$\bar{H}(\bar{\psi}_x, \bar{\psi}_y, \bar{J}_x, \bar{J}_y; \theta) = \nu_{0x}\bar{J}_x + \nu_{0y}\bar{J}_y + \frac{2\pi K_{\mathrm{p}}(s)}{L}(2\bar{J}_x\beta_x)^{|k|/2}(2\bar{J}_y\beta_y)^{|\ell|/2}\cos^{|k|}\Phi_x \cos^{|\ell|}\Phi_y, \tag{1.23}$$

where

$$\Phi_x = \bar{\psi}_x + \int^s \frac{ds}{\beta_x} - \nu_{0x}\theta, \quad \Phi_y = \bar{\psi}_y + \int^s \frac{ds}{\beta_y} - \nu_{0y}\theta. \tag{1.24}$$

The Hamiltonian is rescaled by $L/2\pi$ to change the time coordinate from s to $\theta(\equiv 2\pi s/L)$. Then the phase advance is proportional to θ as $d\bar{\psi}_{x(y)}/d\theta = \nu_{0x(0y)}$.

The resonances are roughly classified into two types: non-coupling resonance and coupling resonance. The former develops in one degree of freedom, the other in two or three degrees of freedom. The following two sections are devoted to showing the feature of each type with 3rd external nonlinear field for example.

1.4.1 Non-coupling resonance

The driving term can be expanded in Fourier harmonics. Assuming $k = 3$ and $\ell = 0$, the Fourier components include the term that is proportional to $\cos(3\bar{\psi}_x - n\theta + \zeta_{3,0,n})$ where $\zeta_{3,0,n}$ is the Fourier phase. Leaving only the term, we can approximate the Hamiltonian of Eq. (1.23) as

$$\bar{H}_{\mathrm{A}}(\bar{\psi}_x, \bar{J}_x; \theta) = \nu_{0x}\bar{J}_x + G_{3,0,n}\bar{J}_x^{3/2}\cos(3\bar{\psi}_x - n\theta + \zeta_{3,0,n}), \tag{1.25}$$

where $G_{3,0,n}$ is a Fourier amplitude. In order to analyze the third-order resonance, we use the following generating function for a canonical transformation to a rotating system (ψ, J) in phase space.

$$F_{\mathrm{A4}} = \left(\psi_x - \frac{n}{3}\theta + \frac{\zeta_{3,0,n}}{3}\right)J, \tag{1.26}$$

and the Hamiltonian becomes

$$\check{H}_{\mathrm{A}}(\psi, J; \theta) = \delta J + G_{3,0,n}J^{3/2}\cos(3\psi). \tag{1.27}$$

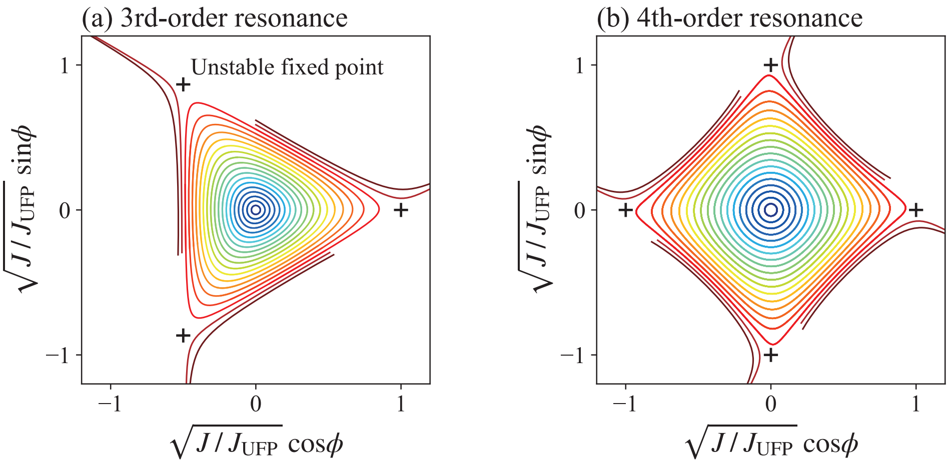

Figure 1.3: Phase spaces for (a) 3rd and (b) 4th-order resonances. Here the normalization constant J_{UFP} is given by $dJ/d\theta = 0|_{J=J_{\mathrm{UFP}}}$.

Here $\delta = \nu_{0x} - n/3$ is the distance of ν_{0x} from the resonance state. The Hamiltonian has three unstable fixed points (UFP) defined by $dJ/d\theta = 0$ and $d\phi/d\theta = 0$. The locations of these UFP are $\psi = \pi, \pm\pi/3$ with $J = |2\delta/3G_{3,0,n}|$ for positive $\delta/G_{3,0,n}$, and $\psi = 0, \pm 2\pi/3$ for negative $\delta/G_{3,0,n}$ similarly. It appears from Eq. (1.27) that J decreases or increases near the UFP and the particle distribution deformed into a triangle-like shape shown in Fig. 1.3 (a). Similar results can be obtained for higher-order driving terms. For example, the deformation caused by 4th-order non-coupling resonance is shown in Fig. 1.3 (b). Therefore we obtain the non-coupling resonance condition driven by mth-order nonlinear external force as

$$m\nu_{0x} = n. \tag{1.28}$$

Note that the term that is proportional to $\cos(\bar{\psi}_x - n\theta + \zeta_{1,0,n})$ is included in Fourier components of the driving term in Eq. (1.23). Thus mth-order nonlinear external force also can drive the resonances with smaller order than m by even numbers. For example, 4th-order nonlinear field can also drive the 2nd-order resonance and can't drive the 3rd-order resonance.

It is easy to see that the resonances can be excited by mth-order nonlinear force of the frequency κ_m under the condition

$$m\nu_{0x} = n \pm \kappa_m. \tag{1.29}$$

1.4.2 Coupling resonance

Assuming $k = 1$ and $\ell = \pm 2$, we focus on the Fourier component that has the harmonic number of $\bar{\psi}_x \pm 2\bar{\psi}_y - n\theta$ and neglect all other non-resonant components. Then Eq. (1.23) becomes

$$\bar{H}_{\mathrm{B}} = \nu_{0x}\bar{J}_x + \nu_{0y}\bar{J}_y + G_{1,\pm2,n}\bar{J}_x^{1/2}\bar{J}_y\cos(\bar{\psi}_x \pm 2\bar{\psi}_y - n\theta + \zeta_{1,\pm2,n}), \tag{1.30}$$

where $G_{1,\pm2,n}$ and $\zeta_{1,\pm2,n}$ are a Fourier amplitude and a Fourier phase. We introduce the rotating system using a canonical transformation, as is the non-coupling case. The generating function for the transformation $(\bar{\psi}_x, \bar{\psi}_y, \bar{J}_x, \bar{J}_y) \longrightarrow (\psi_1, \psi_2, J_1, J_2)$ is

$$F_{\mathrm{B}4} = \left(\bar{\psi}_x \pm 2\bar{\psi}_y - n\theta + \zeta_{1,\pm2,n}\right) J_1 + \bar{\psi}_y J_2, \tag{1.31}$$

which yield the transformation equations

$$\begin{aligned} \psi_1 &= \bar{\psi}_x \pm 2\bar{\psi}_y - n\theta + \zeta_{1,2,n}\ , \quad & J_1 &= \bar{J}_x \\ \psi_2 &= \bar{\psi}_x\ , & J_2 &= \bar{J}_y \mp 2\bar{J}_x, \end{aligned} \tag{1.32}$$

and the Hamiltonian becomes

$$\check{H}_{\mathrm{B}}(\psi_1, \psi_2, J_1, J_2; \theta) = \delta J_1 + \nu_{0y} J_2 + G_{1,\pm2,n} J_1^{1/2} (J_2 \pm 2J_1) \cos\psi_1, \tag{1.33}$$

where $\delta = \nu_{0x} \pm 2\nu_{0y} - n$. We find that J_2 is invariant since the Hamiltonian is independent of ψ_2. Near the resonance condition $\delta \approx 0$, the Hamiltonian equation for J_1 is given by

$$\frac{d^2 J_1}{d\theta^2} - G_{1,\pm2,n}^2 \frac{12J_1^2 \pm 8J_1J_2 + J_2^2}{2} = 0. \tag{1.34}$$

If we chose the upper sign of ± and ∓ in equations (1.30)~(1.34), Eq. (1.34) suggests that the J_1 diverges depending on the initial conditions. Then the resonant instability develops in two degrees of freedom with the weighted difference in actions $\bar{J}_y - 2\bar{J}_x$ left constant. Such resonances are called “sum-resonance” and are of particular concern in accelerator operation. On the other hand, in the case of lower sign (“difference-resonance” case), beam stability is guaranteed due to the invariance of the weighted sum of actions $\bar{J}_y + 2\bar{J}_x$. Consequently, we obtain the resonance condition in Eq. (1.20) whose driving term is proportional to $x^{|k|}y^{|\ell|}$.

Chapter 2

Space-charge effects

2.1 Root-mean-squared envelope equations with space charge

Since the beam is composed of many particles, the approach based on statistical averages rather than single-particle quantities is much more convenient. Considering that the observable quantities in experiments are only the averaged values whole of the beam, such an approach is also practically advantageous. In this section, we review the well-known second-moment equations developed by Sacherer [7, 8].

For example, we assume the 2D case for a continuous beam, and the Hamiltonian from Eq. (1.8) becomes

$$H(x, y, p_x, p_y; s) = \frac{p_x^2 + p_y^2}{2} + \frac{K_x(s)}{2}x^2 + \frac{K_y(s)}{2}y^2 + \frac{q\phi_{\rm sc}}{mc^2\beta_{\rm s}^2\gamma_{\rm s}^3}, \tag{2.1}$$

where the Hamiltonian is normalized by p_0. And the equations of motion are

$$\begin{cases} \dfrac{d^2x}{ds^2} + K_x(s)x - \dfrac{qE_{\rm sc}^x}{mc^2\beta_{\rm s}^2\gamma_{\rm s}^3} = 0, \\ \dfrac{d^2y}{ds^2} + K_y(s)y - \dfrac{qE_{\rm sc}^y}{mc^2\beta_{\rm s}^2\gamma_{\rm s}^3} = 0, \end{cases} \tag{2.2}$$

where $E_{\rm sc}^x$ and $E_{\rm sc}^y$ are electric field generated by $\phi_{\rm sc}$.

Considering 2nd-order moments, we can find the relation

$$\begin{cases} \dfrac{d\langle w^2\rangle}{ds} = \langle wp_w\rangle, \\ \dfrac{d\langle wp_w\rangle}{ds} = \langle p_w^2\rangle - K_w(s)\langle w^2\rangle + \left\langle \dfrac{qwE_{\rm sc}^w}{mc^2\beta_{\rm s}^2\gamma_{\rm s}^3} \right\rangle, \\ \dfrac{d\langle p_w^2\rangle}{ds} = -2K_w(s)\langle wp_w\rangle + 2\left\langle \dfrac{qp_wE_{\rm sc}^w}{mc^2\beta_{\rm s}^2\gamma_{\rm s}^3} \right\rangle, \end{cases} \tag{2.3}$$

where w stands for x or y. $\langle V\rangle$ means taking average of V over the whole phase space. Let us define the rms radius of the beam in w-direction by $r_w \equiv \sqrt{\langle w^2\rangle}$. Combining the Eqs. (2.3) yields

$$\begin{cases} \dfrac{d^2 r_x}{ds} + K_x(s) r_x - \dfrac{\varepsilon_x^2}{r_x^3} - \dfrac{K_{\rm sc}}{2(r_x + r_y)} = 0, \\ \dfrac{d^2 r_y}{ds} + K_y(s) r_y - \dfrac{\varepsilon_y^2}{r_y^3} - \dfrac{K_{\rm sc}}{2(r_x + r_y)} = 0, \end{cases} \tag{2.4}$$

where $K_{\rm sc} = q^2\lambda / 2\pi\epsilon_0 p_0 \beta_{\rm s} c \gamma_{\rm s}^2$ is generalized perveance. λ is the number of particles per unit length. Assuming the distribution with elliptical symmetry, $\langle w E_{\rm sc}^w \rangle$ can be written as

$$\langle w E_{\rm sc}^w \rangle = \frac{q\lambda^2 r_w}{r_x + r_y} . \tag{2.5}$$

ε_w is the rms emittance defined by

$$\varepsilon_w \equiv \sqrt{\langle w^2 \rangle \langle p_w^2 \rangle - \langle w p_w \rangle^2} . \tag{2.6}$$

The rms emittance is equal to the average of the action J_w and represents the phase space area occupied by the beam; the rms emittance is also a useful index of the beam quality.

Let us introduce the rms tune shift in w direction as follows

$$\Delta\bar{\nu}_w = \nu_{0w} - \frac{\varepsilon_w}{2\pi} \int_{s_0}^{s_0+L} \frac{ds}{r_w^2} . \tag{2.7}$$

This quantity represents the decrease of the tune caused by linear space charge force and can be determined uniquely for a beam. For later convenience we define the rms tune depression η_w by

$$\eta_w = 1 - \frac{\Delta\bar{\nu}_w}{\nu_{0w}} . \tag{2.8}$$

where η_w ranges from 0 to 1 and takes 0 for the high-density limit. It is worth noting that rms tune depression can be defined for any beam with elliptical symmetry independent of the particle distribution the beam possesses in real space. Thus we can express the strength of the space charge force universally by using η_w.

2.2 Resonance conditions with space charge

It is indispensable for resonance analysis in high-intensity hadron machines to take the effect of space-charge interaction into account. The Coulomb repulsive force weakens the external focusing force from the quadrupole magnet and leads to the reduction of the effective betatron tune. Thus, the single-particle resonance condition in Eq. (1.20) is not necessarily appropriate once the space-charge effect becomes non-negligible. We here introduce several examples of the resonance condition modified to include the space-charge effect.

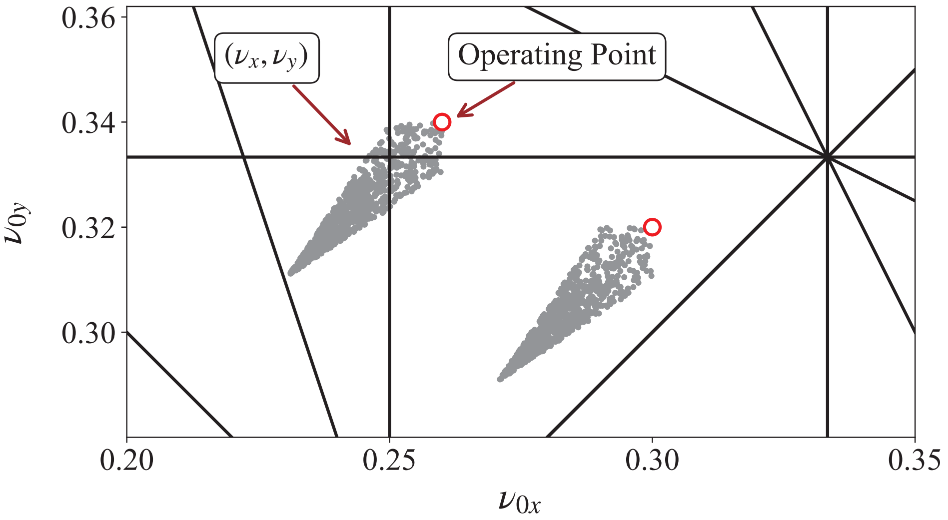

Figure 2.1: Determination of the operating point based on the conventional incoherent picture. The red circle denotes the operating point (ν_{0x}, ν_{0y}), and gray dot denotes the incoherent tune of each particle (ν_x, ν_y). The operating point is chosen so that the incoherent tune spread does not cross the low-order resonance lines shown by solid lines.

2.2.1 Incoherent resonance condition

The starting point is the Hamiltonian in Eq. (1.17) with the self-field potential $\phi_{\rm sc}$

$$\hat{H}(\psi_x, \psi_y, J_x, J_y; s) = \frac{J_x}{\beta_x} + \frac{J_y}{\beta_y} + \frac{q\phi_{\rm sc}}{mc^2\beta_{\rm s}^2\gamma_{\rm s}^3}\,. \tag{2.9}$$

Hamiltonian's equation becomes

$$\frac{d\psi_{x(y)}}{ds} = \frac{1}{\beta_{x(y)}} + \frac{q}{mc^2\beta_{\rm s}^2\gamma_{\rm s}^3}\frac{\partial\phi_{\rm sc}}{\partial J_{x(y)}}\,. \tag{2.10}$$

This yields the incoherent tune per lattice period

$$\nu_{x(y)} = \nu_{0x(0y)} + \frac{q}{2\pi mc^2\beta_{\rm s}^2\gamma_{\rm s}^3}\int_{s_0}^{s_0+L}\frac{\partial\phi_{\rm sc}}{\partial J_{x(y)}}ds. \tag{2.11}$$

The incoherent tunes of particles forming a particular beam are distributed in a finite area that is called "incoherent tune spread" in the tune space schematically shown in Fig. 2.1. Since $\partial\phi_{\rm sc}/\partial J_{x(y)}$ is generally negative, the incoherent tune spread lies lower tune region than the operating point (ν_{0x}, ν_{0y}). With the horizontal and vertical incoherent tunes, the incoherent resonance condition is given by

$$k\nu_x + \ell\nu_y = n. \tag{2.12}$$

In order to avoid the resonance instabilities predicted by the incoherent resonance condition, the operating point is required to be chosen so that the tune spread does not cross the low-order resonance lines. For example, based on this concept, the operating point on the right side of Fig. 2.1 is the better one. As is obvious from this figure, what is important in the incoherent resonance condition is the width of the tune spread.

Adopting the Gaussian model that has been frequently employed to determine the operating point in past theoretical studies, we obtain

$$\max(\Delta\nu_x) \approx (1-\eta_x^2)\nu_{0x}, \tag{2.13}$$

where $\Delta\nu_x(\equiv \nu_{0x} - \nu_x)$ is referred as to "incoherent tune shift" (see appendix A). Eq. (2.13) suggests that the tune spread gets larger as the beam density becomes higher ($\eta_x \to 0$). A similar tendency can be seen for non-Gaussian models.

The incoherent concept mentioned above has practically undesirable features. First of all, it is difficult to obtain the density profile experimentally; in other words, we have to assume some plausible models to obtain J_x and J_y in Eq. (2.11). Considering that the injection painting scheme is employed in modern rings, there is no clear argument for adhering to the Gaussian model despite the fact that it is frequently adopted. In addition, Eq. (2.11) suggests that resonance instabilities are hardly driven when we adopt the Kapchinskij-Vladimirskij (K-V) model that has no tune spread, contrary to the prediction of Vlasov analysis [12]. The incoherent concept, however, has been employed in almost all synchrotrons for decades because it is much easier and simpler than numerical simulations and experiments.

2.2.2 Coherent resonance condition

The space-charge dominant beam behaves as a sort of continuum, rather than a group of particles independent of each other. In this case stability of the beam is seriously affected by the collective nature. The resonance condition of the collective motion is referred to as the "coherent resonance condition" studied by many researchers [8,12–23]. If we ignore the Coulomb collisions whose effect is negligible in general beams, the use of the Vlasov-Poisson formalism is one of the most trustable manners to explore the collective motion [24,25]. The first coherent resonance condition derived in the pioneering work of Sacherer is

$$m(\nu_{0x} - C_{mh}\Delta\nu) = n, \tag{2.14}$$

where C_{mh} is a constant depending on the azimuthal (m) and radial (h) mode numbers [8]. Assuming a spatially uniform beam propagating through a continuous focusing lattice, Sacherer analytically solved the 1D Vlasov-Poisson equations. Since the space-charge force is completely linear, all particles have an identical tune shift $\Delta\nu$. R. L. Gluckstern extended Sachere's theory to a round coasting beam [14]. After that, I. Hofmann *et al.* solved 2D Vlasov-Poisson equations under AG-focusing lattice with a help of the spatially uniform distribution and proposed the coherent resonance condition

$$k\nu_x + \ell\nu_y + \Delta\upsilon = n, \tag{2.15}$$

where $\Delta\upsilon$ represents the coherent tune shift and is a complicated function of several parameters [22].

2.2.3 Okamoto and Yokoya theory

Self-field-driven resonance

One of the works based on the Vlasov-Poisson formalism was done by H. Okamoto and K. Yokoya [20]. They assumed the 1D sheet-beam propagating through an AG lattice. Adopting the waterbag model, which has a uniform density in phase space, they concluded that the coherent resonance condition for that case is given by

$$m[\nu_{0x} - C_m(1-\eta_x)\nu_{0x}] = \frac{k}{2}, \tag{2.16}$$

where m is the order of the resonance. C_m is a constant, and we call it "tune shift factor" in this paper. Theoretically, C_m is lower than one for all m numbers. It is worthy to mention that they assume no external driving field to derive Eq. (2.16); in other words, various resonances can occur due to the nonlinearity of space-charge force in AG lattice even if there is no external driving force, unlike the case of single particle resonances shown in Chapter 1. It is also important that the right-hand side of Eq. (2.16) is half integers. This implies the existence of twice as many resonances as predicted by common theories. Then the width of mth resonance band Δw_m can approximately be written (see Appendix B)

$$\Delta w_m = 2(1-C_m)\frac{1-\eta_x}{\eta_x}\nu_{0x}. \tag{2.17}$$

External-field-driven resonance

They also derived the resonance condition in which an external driving field is introduced

$$m[\nu_{0x} - C_m(1-\eta_x)\nu_{0x}] = n \pm \kappa_m, \tag{2.18}$$

where κ_m is the oscillation frequency of mth-order nonlinear driving field [26]. This relation suggests that the tune shift factor is kept unchanged regardless of whether the resonance is driven by the self field or the external field. In the general case where the driving field oscillates with the same frequency of lattice period (namely κ_m is an integer), the right-hand side of Eq. (2.18) is not half integers. Thus this is identical to Eq. (1.28) or Eq. (1.29) at the zero-intensity limit.

Chapter 3

Resonance in circular accelerators

3.1 Introduction

The resonance can be of great danger in AG-focusing modern accelerators. Such instability causes the degradation of beam quality or particle loss inside the accelerator. In order to avoid this instability, the operating point given by the horizontal and vertical bare tunes (ν_{0x}, ν_{0y}) is kept sufficiently away from the resonance conditions. The conventional single-particle resonance condition in Eq. (1.20) derived by Courant and Snyder is one of the most popular formulas [2]. However, the increasing demand for high beam intensity and performance made it essential to modify the resonance condition by considering the space charge effect. The incoherent resonance condition in Eq. (2.12) is one of the most widely used such resonance conditions [9–11]. On the other hand, the incoherent tune can't be determined by experiments because we can't track each particle's trajectory. It is important to note that the incoherent resonance condition is based on the single particle motion rather than the collective nature of the beam since Eq. (2.12) can be obtained simply by exchanging bare tunes and incoherent tunes in Eq. (1.20). Considering that the particle motion in dense beam core interacts with each other by Coulomb repulsive force, the instability of the beam core is expected to develop collectively. It is thus valuable for high-intensity accelerators to establish the "coherent resonance condition" based on the collective manner. Much effort has been devoted to establishing the coherent resonance condition because of its practical importance [8, 12, 13, 16–19, 22, 27, 28].

The motivation of this study is to verify the 2D coherent resonance condition that we proposed in recent years. We conducted self-consistent numerical simulations with the help of a particle-in-cell (PIC) code "W$_{\text{ARP}}$" for the purpose [29]. In this chapter, we concentrate on the transverse 2D dynamics of coasting beams propagating through circular accelerators, ignoring the longitudinal motion and energy spreads. We first give an overview of the 2D coherent resonance condition in Sec. 3.2. After presenting the simulation conditions, Sec. 3.4 is devoted to figuring out the difference between the tail and core resonance mechanisms. In Sec. 3.5, we compare the distribution of resonance stop bands driven solely by the self-field with the indication of the coherent resonance condition to see if the proposed conditions are consistent with numerical results. We then proceed to the evaluation of tune shift factors in Sec. 3.6. Finally, we apply the coherent resonance condition to the current states of J-PARC RCS.

3.2 2D coherent resonance condition

In recent years, our group generalized the conclusion of linearized Vlasov analysis in Eq. (2.16) and proposed a hypothesis of 2D coherent resonance condition,

$$k(\nu_{0x} - C_m \Delta\bar{\nu}_x) + \ell(\nu_{0y} - C_m \Delta\bar{\nu}_y) = \frac{n}{2} \,. \tag{3.1}$$

This formula is identical to the single particle resonance condition in Eq. (1.20) at zero intensity limit when n is even. In the case of non-coupling resonances ($k = 0$ or $\ell = 0$), Eq. (3.1) is also identical to Eq. (2.16). Eq. (3.1) has three important features that distinguish it from conventional resonance conditions. First, the right-hand side is half integers, not integers. As mentioned in Subsection 2.2.3, it indicates the two-fold resonance band increase in the tune space. Second, the tune shift factor C_m depends only on the resonance order $m(= |k| + |\ell|)$. In the previous works, the factors corresponding to C_m are more complicated and depend on several beam properties such as the ellipticity and bare tunes [12, 22, 23, 30]. Finally, the formula is expected to be model-independent and includes only the statical averages that can be defined for any beams. Eq. (3.1), however, still remains to be only an empirical hypothesis. Since it is hopeless to solve the 2D Vlasov-Poisson equations mathematically for arbitrary focusing lattices and phase-space distributions, we rely on the numerical simulation to verify those features in later sections.

3.3 Self-consistent numerical simulation

The self-consistent numerical simulations have become a powerful tool to investigate accelerator systems with space charge. Numerical simulations are routinely used to identify the cause of beam instabilities and accelerator designs in beam dynamics. There are many simulation codes for such purposes, and we adopted the WARP code in this study [29]. This code is developed originally for the research of inertial confinement fusion driven by heavy-ion and is equipped with a versatile set of functions that enables a wide variety of simulations.

3.3.1 Sinusoidal focusing lattice

As illustrated in Fig. 3.1, we replace the K_x and K_y with stepwise τ dependence by the sinusoidal function, which is the most dominant harmonics of the standard FODO (Focusing-Drift-Defocusing-Drift) lattice. Then the K_x and K_y can be written by

$$\begin{aligned} K_x &= V_0 \sin(2\pi\tau/L) + U_0, \\ K_y &= -V_0 \sin(2\pi\tau/L) - U_0, \end{aligned} \tag{3.2}$$

where, V_0 and U_0 are constants. The horizontal and vertical bare tunes can be set at arbitrary values by choosing the proper V_0 and U_0. The resonance features of the sinusoidal lattice have been confirmed to be almost the same as those of the FODO lattice [31, 32]. Additionally, the exception of higher harmonics in $K_{x(y)}$ leads to better convergence with relatively few time steps.

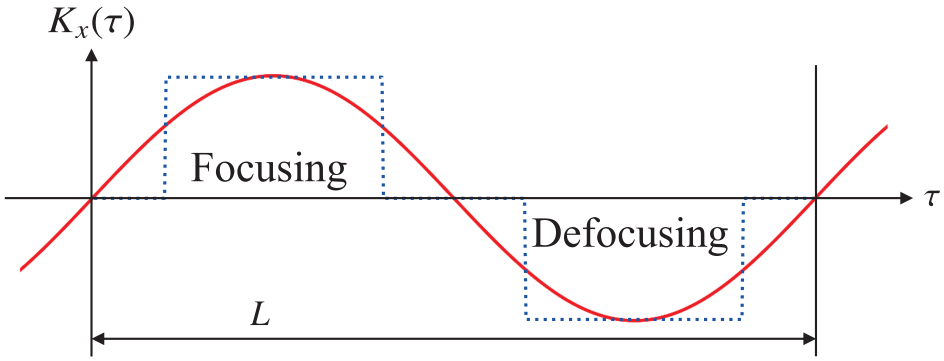

Figure 3.1: Sinusoidal focusing lattice.

Table 3.1: Distribution functions

TE (Thermal Equilibrium)	$f(H_b) = f_0 \exp\left(-\frac{m\gamma_s\beta_s^2c^2H_b}{T}\right)$
WB (WaterBag)	$f(H_b) = f_0\Theta(H_b - H_0)$
PA (PArabolic)	$f(H_b) = f_0(H_b - H_0)\Theta(H_b - H_0)$

3.3.2 Phase-space matching of an initial particle distribution

In this study, we adopted not one but three models Gaussian (TE), WaterBag (WB), and PArabolic (PA) for two reasons. First, it is difficult to obtain precise density profiles in the phase-space for high-power hadron beams. It is thus dangerous to adhere to only one model since the detail of the actual beam profile is ambiguous. In particular, the behavior of the Gaussian beam is relatively peculiar among the three as shown in the later sections, even though the Gaussian model is frequently employed. Second, it is informative to investigate the model dependency of the coherent resonance condition in Eq. (3.1) as mentioned above. In order to ensure good generality, we decided to compare the simulation results across the three models.

It is required for the simulations of high-intensity beams that the initial distributions are well adapted to the lattice. The Vlasov equation indicates that the distribution functions defined by the Hamiltonian describe the equilibrium state. However, due to the mathematical difficulties to solve the Vlasov-Poisson formula self-consistently under an arbitrary periodic focusing force, the rms matching concept in which the beam rms radius is set properly based on the rms envelope Eq. (2.4) is generally employed [7, 13]. The rms matching inevitably leads to an emittance blowup or halo formation [28, 33, 34]. Especially the matching error is considerably enhanced at high beam density. In our study, a more sophisticated method than rms matching is employed. The method, which is called Pseudo-equilibrium distribution, is proposed by Lund and his co-workers and equipped with the WARP code [35]. The essence of the method is to

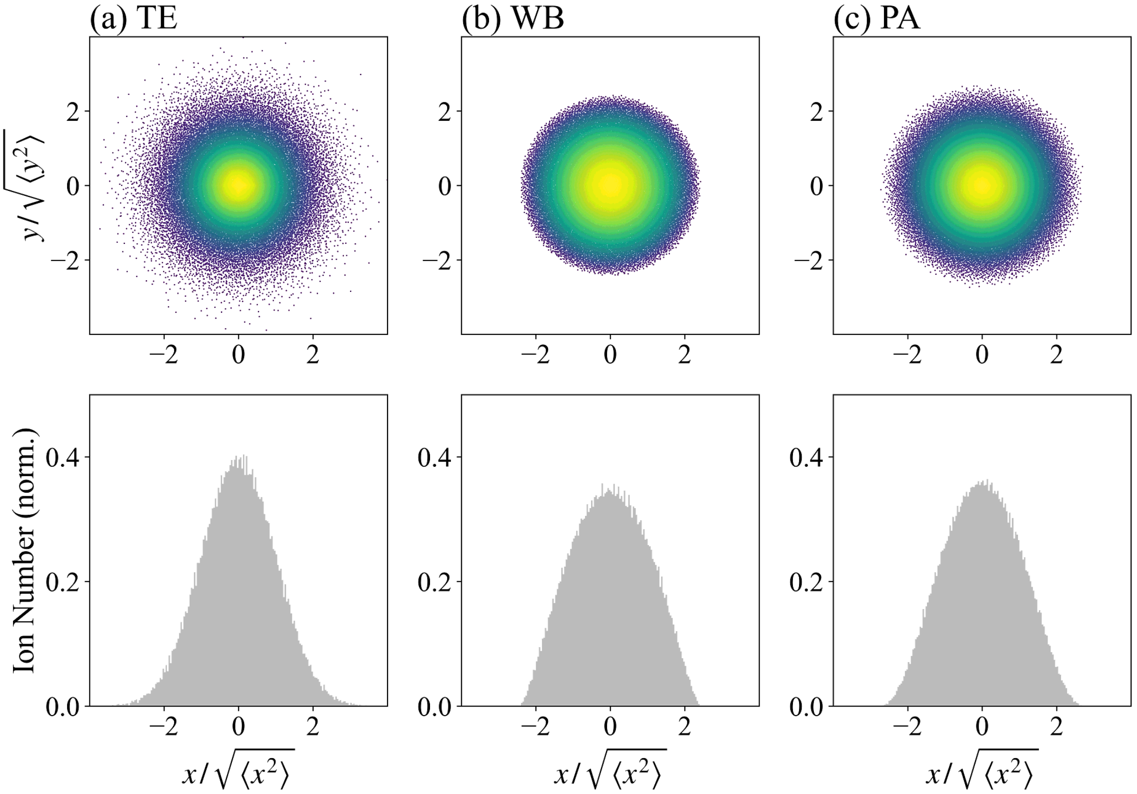

Figure 3.2: The upper panels show the initial particle distributions in the real space. The lower panels show particle number histograms.

approximate the Hamiltonian by the time-independent 1D Hamiltonian written as

$$H_b = \frac{p^2}{2} + \frac{k_b^2 r^2}{2} + \frac{q\phi_{\mathrm{sc}}}{m\gamma_{\mathrm{s}}^3\beta_{\mathrm{s}}^2c^2}, \tag{3.3}$$

where $r = \sqrt{x^2+y^2}$ and $k_b \equiv \sqrt{K_{\mathrm{sc}}/r_b^2 + \varepsilon_b^2/r_b^4}$ is the time-independent focusing strength given with the averaged beam radius $r_b = \sqrt{r_x r_y}|_{\tau=0}$ and the averaged rms emittance $\varepsilon_b = \sqrt{\varepsilon_x\varepsilon_y}$. The distribution functions defined with H_b are shown in Table 3.1 where H_0 and f_0 are constants. T denotes the temperature. We can obtain the pseudo equilibrium distribution by processing the rms matching to the circular symmetric stationary state given by the distribution functions.

The real space profiles of the three particle distributions are shown in Fig. 3.2. The particles are color-coded by relative density. The horizontal and vertical tune depressions are set at 0.95, which is a typical simulation condition in this chapter. The WB distribution has the flattest density profile of the three, followed by the PA distribution. The Gaussian distribution is distinctive and has a high-density beam core and a wide low-density region (tail region).

3.3.3 Simulation parameters

We assume a proton coasting beam propagating through a periodic focusing lattice, and the focusing force acting on the beam is perfectly linear. The beam profile is then uniform in the longitudinal direction, and the 2D PIC simulation is suitable for this case. The basic simulation parameters are shown in Table 3.2. The parameters related to the PIC method are carefully

Table 3.2: Basic parameters of 2D PIC simulations.

Grid size	0.072 [mm]
Number of macro particles	50000
Number of macro particles per grid cell	20 ~ 40
Simulation region	21.5×21.5 [mm^2]
Steps per cell	200
Ion Specie	H$^+$
Kinetic Energy	1 [MeV]
Lattice period	1.38 [m]

optimized to guarantee the accuracy of the calculation [36]. The Dirichlet boundary condition for self-field potential is imposed on the edge of the simulation area. On the other hand, the width of the simulation area is sufficiently large that the boundary condition does not affect the beam motion.

3.4 Resonance instabilities for round beams

Before proceeding to 2D cases, we investigate the stop band distributions assuming round beams when the horizontal and vertical motions are symmetric. The resonances are then expected to develop one-dimensionally since the horizontal and vertical systems are effectively equivalent. In this case, the beam parameters such as the bare tunes and initial emittances are set equal in horizontal and vertical directions. We have conducted numerical simulations to explore the resonance instabilities driven by the space charge force. It is demonstrated that the coherent resonance conjecture in Eq. (3.1) can predict the approximate position of the 2nd, 3rd, and 4th-order collective non-coupling resonances. We also show that the three different resonance mechanisms exist on the well-known envelope instability band; namely the 2nd-order, 4th-order coherent resonances, and the 4th-order incoherent resonance.

3.4.1 Comparison of simulation results and 1D Vlasov analysis

Figure 3.3 shows the emittance growth $\Delta\varepsilon^{\mathrm{avg}}$ vs the bare tune $\nu_0(\equiv \nu_{0x} = \nu_{0y})$ where the emittance growth is defined as

$$\Delta\varepsilon^{\mathrm{avg}} = \left[\frac{\varepsilon_x^{\mathrm{fin}} + \varepsilon_y^{\mathrm{fin}}}{\varepsilon_x^{\mathrm{ini}} + \varepsilon_y^{\mathrm{ini}}} - 1\right] \times 100 \quad [\%]. \tag{3.4}$$

$\varepsilon_{x(y)}^{\mathrm{ini}}$ and $\varepsilon_{x(y)}^{\mathrm{fin}}$ are the initial rms emittance and the rms emittance after 300 lattice periods respectively. Since no external nonlinear field is applied, the observable stop bands are solely caused by space charge force.

The sawtooth-like configuration of the emittance growth peaks can be observed. This is caused by the reduction of the beam's phase-space density associated with the development of instabilities, which makes the tune depression approach unity. Then, it is clear from Eq. (2.16) that the resonant value of the bare tune becomes lower. Since the stopband gradually moves toward the lower tune, the development of instability tends to be suppressed in the higher tune

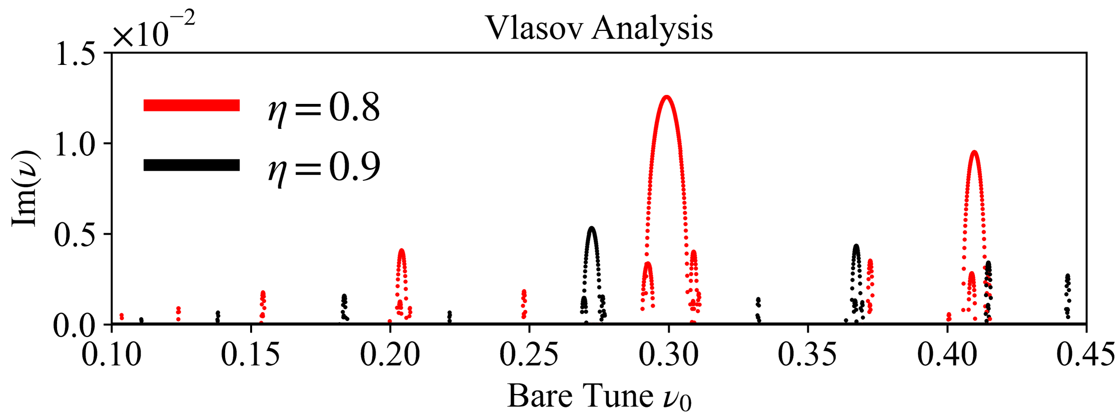

(a) TE

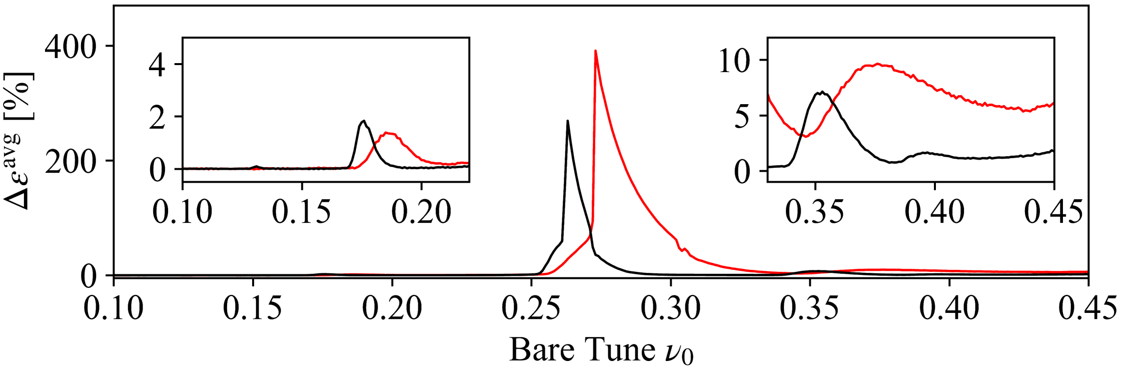

(b) WB

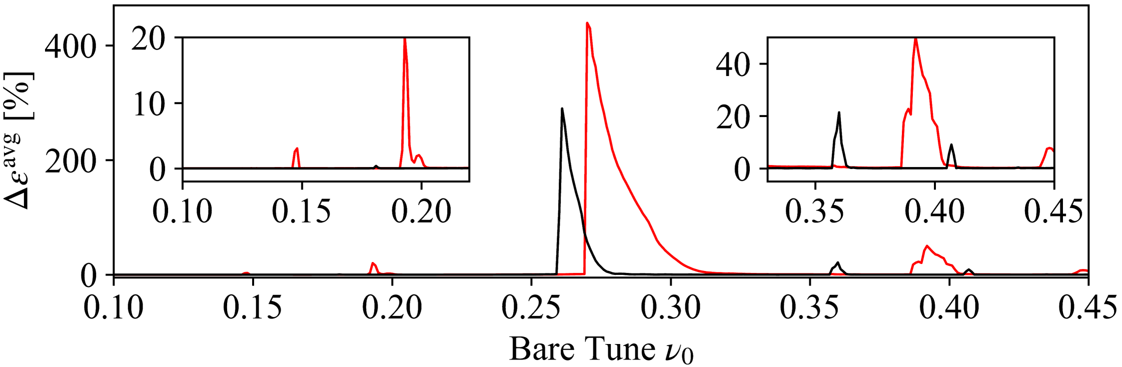

(c) PA

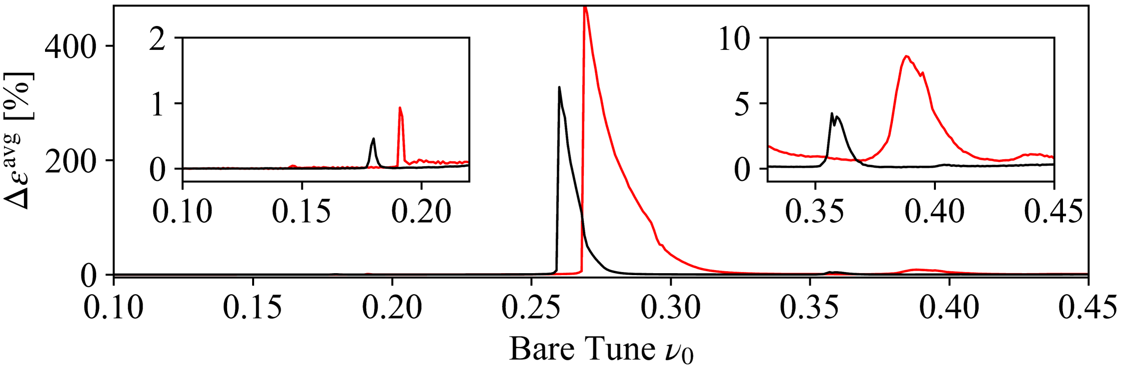

Figure 3.3: The upper panel shows the growth rate amplitude of low-order modes as a function of the bare tune. The panels (a), (b), and (c) show the stopband configurations at the exit of the 300th lattice period for three different types of distributions with η = 0.8 and 0.9: (a) Gaussian, (b) waterbag, and (c) parabolic.

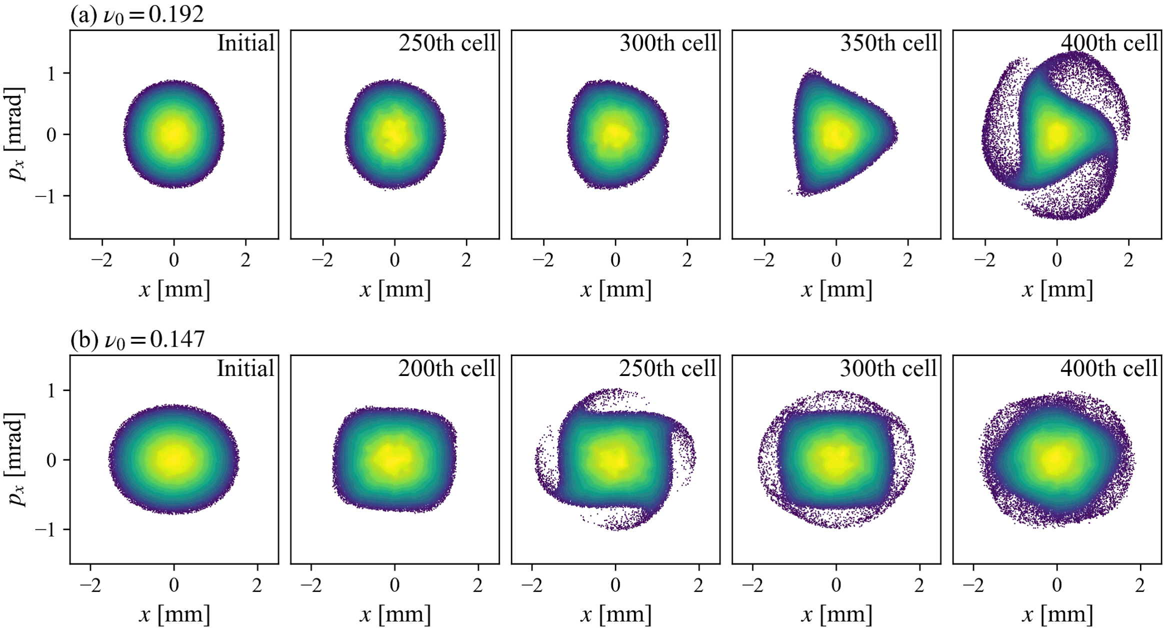

Figure 3.4: The waterbag type initial distribution is adopted. The transverse operating tunes set at (a) $\nu_0 = 0.192$ and (b) $\nu_0 = 0.147$, and the tune depressions are initially adjusted to $\eta = 0.8$ in both cases.

side of the stopband. A similar effect has been observed in experiments with a Paul ion trap [31, 32, 37–42].

There is the most severe emittance growth takes place near the bare tune of 0.25 for all three cases. The instability is likely to be caused mainly by 2nd-order resonance and is referred to as "Envelope instability" studied by many researchers [13, 27, 43–45]. The 1D Vlasov analysis also predicts that the severe instability of 2nd-order resonance occurs there.

We can find two peaks on the lower tune side than 0.25. According to the 1D Vlasov analysis and the coherent resonance condition in Eq. (3.1), the peaks of emittance growth that take place slightly above $1/6$ and $1/8$ are caused by the 3rd-order and the 4th-order resonances respectively. Figure 3.4 shows an example of the time evolution of the waterbag distribution. When the operating bare tune is set at 0.192 which is inside the 3rd-order stopband predicted by Eq. (3.1), the deformation of the beam core into a triangle-like shape is shown. Similarly, a rectangle-like deformation is observed inside the 4th-order stopband. These results indicate that the low-order collective instabilities develop in the beam core. Such instabilities cannot be described by the incoherent pictures.

The features of Gaussian stopbands are much different from the other two. First of all, they are extended toward the lower thresholds given by the single particle reasons condition in Eq. (1.20). The peculiarity is observed for the peaks near the bare tune of 0.25. The significant extra emittance growths between the left edge of the peaks and 0.25 have occurred for the Gaussian case. These results suggest that resonances with different underlying mechanisms overlap. It can be explained by considering the tail resonances that are prominent for the Gaussian distribution, and we discuss this issue in detail in the following subsections.

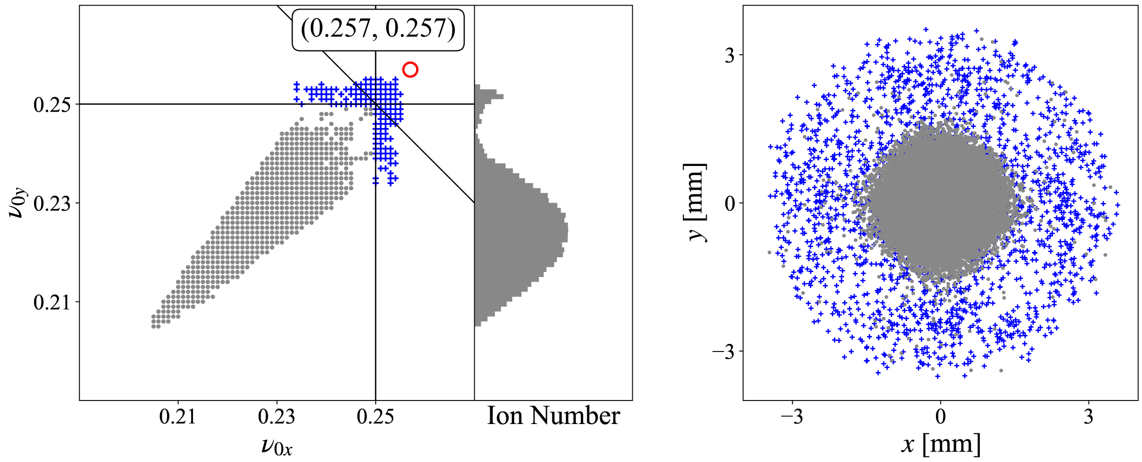

Figure 3.5: The left panel shows an incoherent tune spread of the Gaussian beam. The right panel shows particle distribution in real space at the exit of the 1000th lattice period. The operating tune is set at $\nu_0 = 0.257$. The tune depression is adjusted to $\eta = 0.9$ at injection. The macroparticles with horizontal or vertical incoherent tunes greater than 0.25 are represented by blue dots.

3.4.2 Tail and core resonances above a quarter-integer tune

The coherent resonance condition in Eq. (3.1) predicts that the resonance of mth-order always overlaps with the resonance of $2m$th-order. For example, 2nd and 4th-order resonances take place near the bare tune of $1/4$, and 3rd and 6th-order resonances take place near the bare tune of $1/6$ as well. According to 1D Vlasov theory, the higher order resonances have the higher resonant value of the bare tune since the tune shift factor C_m theoretically gets greater as the m number increases. Thus the instabilities of higher-order resonances are expected to locate higher tune side of the stopband. On the other hand, the simulation result shown in Fig. 3.3 indicates the existence of the other instability that occurs lower tune side than the instability mainly caused by the 2nd-order resonance for the Gaussian case. Considering that the lowest order of the resonance driven by the space charge is 2nd (1st mode means the oscillation of the center of mass), a different mechanism from the collective instability seems to be there. The purpose of this subsection is to examine the resonance overlapping issue. We have focused on the well-known envelope instability band above the 0.25 bare tune per lattice period which is one of the most practically important resonances for high-intensity machines because of its strong influence on beam stability.

Tail resonance

Figure 3.5 shows an incoherent tune spread of a Gaussian beam when the tune depressions are fixed to 0.9. The operating point is set at $(\nu_{0x}, \nu_{0y}) = (0.257, 0.257)$ which is inside the extra stopband adjacent to the envelope instability band. The gray and blue dots indicate the average incoherent tunes of individual macroparticles evaluated numerically using the Fourier analysis. It is shown that the several hundred macro particles moved above 4th-order resonance lines indicated by the single particle resonance condition and form a halo around the beam core in real space. This is because the self-field force that acts on the particle is weakened as the betatron oscillation amplitude is enlarged by the resonance. It is worth noting that the beam

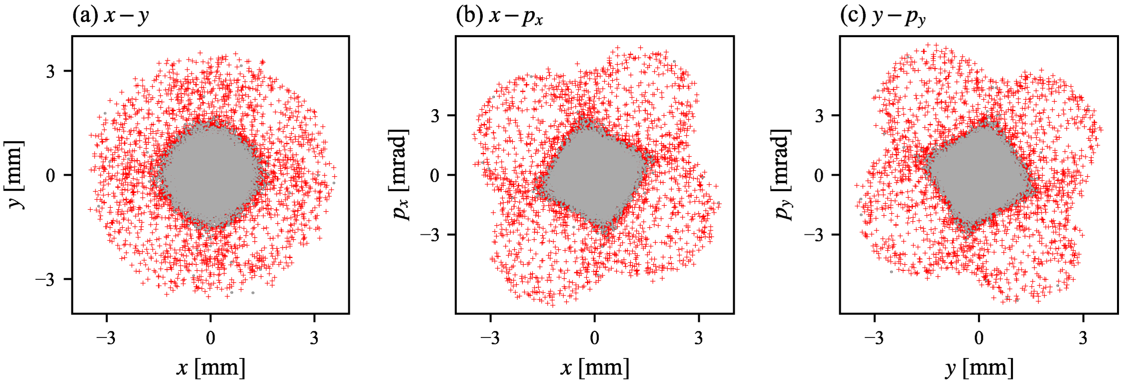

Figure 3.6: Phase space configuration at the exit of the 1000th lattice period. 10% of outermost particles identified at the injection base on the E-value in Eq. (3.10) are represented by the red dots.

core seems to remain stable despite the emittance growth of 34% during the 300 lattice period. Since there is no external driving field, the resonance instabilities of halo particles are driven by the nonlinear self-field.

The result in Fig. 3.5 implies the existence of the self-field-driven incoherent resonance in the tail region. The motion of tail particles far from the core could be rather individual than collective. Taking the spatial symmetry of the beam core into account, the tail resonance that requires particular attention can be written as

$$2\nu_x + 2\nu_y = n, \tag{3.5}$$

where the incoherent tunes should be relatively close to the bare tunes.

3.4.3 Tail separation

Despite the small number of tail particles, they have a significant contribution to the calculation of rms values and are likely to obscure the beam collective instabilities. Thus, it is informative for the elucidation of the resonance mechanism to consider the collective motion of core particles except for tail particles. The Hamiltonian then can provide the information necessary to identify the tail particles executing the betatron oscillation with large amplitude [28, 33]. Since the energy of Coulomb potential is comparably small to the external potential in circular accelerators, it should be enough to consider the contribution from the linear space-charge term only. We can then obtain the approximate Hamiltonian from Eq. (2.9) as

$$\hat{H} = \frac{\hat{J}_x}{\hat{\beta}_x} + \frac{\hat{J}_y}{\hat{\beta}_y}, \tag{3.6}$$

where $\hat{\beta}_{x(y)}$ is the modified betatron function calculated from rms beam radius r_x and r_y in Eq. (2.4) as

$$\begin{aligned} \hat{\beta}_x &= r_x^2/\varepsilon_x\,, \\ \hat{\beta}_y &= r_y^2/\varepsilon_y\,. \end{aligned} \tag{3.7}$$

The actions of certain particle that has the canonical cordinates (x, y, p_x, p_y) are evaluated from

$$\begin{aligned} 2\hat{J}_x &= \hat{\beta}_x p_x^2 + 2\hat{\alpha}_x x p_x + \hat{\gamma}_x x^2\,, \\ 2\hat{J}_y &= \hat{\beta}_y p_y^2 + 2\hat{\alpha}_y y p_y + \hat{\gamma}_y y^2\,, \end{aligned} \tag{3.8}$$

where $\hat{\alpha}_{x(y)}$ and $\hat{\gamma}_{x(y)}$ are the modified Courant-Snyder functions defined as

$$\begin{aligned} \hat{\alpha}_x(s) &= -\frac{1}{2}\frac{d\hat{\beta}_x(s)}{ds}, \quad \hat{\gamma}_x = \frac{1+\hat{\alpha}_x(s)^2}{\hat{\beta}_x(s)}, \\ \hat{\alpha}_y(s) &= -\frac{1}{2}\frac{d\hat{\beta}_y(s)}{ds}, \quad \hat{\gamma}_y = \frac{1+\hat{\alpha}_y(s)^2}{\hat{\beta}_y(s)}. \end{aligned} \tag{3.9}$$

Taking the average of Eq. (3.6) over one lattice period, we introduce the parameter

$$E \equiv \nu_{0x}\eta_x\hat{J}_x + \nu_{0y}\eta_y\hat{J}_y, \tag{3.10}$$

that corresponds to the energy of each particle. It can be used as a good measure of the amplitude of the betatron oscillation unless the beam density is not so high ($\eta_{x(y)} \approx 1$).

Let us take a look again at the simulation result shown in Fig. 3.5. Figure 3.6 shows the particle distribution in phase-space at the exit of the 1000th lattice period. 10% of the outermost particles are classified as tail particles based on the E-value at injection and are shown in red. It is confirmed that most of the halo particles come from the tail region as expected. This strongly suggests that the particles in the tail region where the Coulomb interaction with the beam core is weak tend to become unstable individually. In addition, we can see the development of four arms around the beam core in x-p_x and y-p_y plane. This is consistent with the resonance condition in Eq. (3.5) predicting that the 4th-order resonance occurs under a such situation.

In order to separate the contribution of the tail particles to the rms values, we check the E-value of individual particles and define the tail particles at injection. The rms emittance growth at the exit of Mth lattice period excluding the tail particle contribution is calculated as

$$\Delta\varepsilon^{(\kappa)}(M) \equiv \frac{\varepsilon^{(\kappa)}(M) - \varepsilon^{(\kappa)}(0)}{\varepsilon^{(0)}(0)} \times 100\,[\%]\,, \tag{3.11}$$

where ε is the sum of the horizontal and vertical rms emittance. κ indicates the percentage of the particles classified as tail particles and excluded from the rms emittance evaluation.

3.4.4 Simulation results

We carried out PIC simulations with the WARP code to explore the resonance features above the 0.25 bare tune per lattice period in detail. The tune depressions are set at 0.9. We used the Gaussian-type distribution that is well adapted to the focusing lattice. Here, the pseudo equilibrium matching procedure mentioned in Subsection 3.3.2 enables to make the emittance growth induced by an initial Coulomb potential mismatch negligible.

Figure 3.7 shows the tune dependence of emittance growth at the exit of the 100th, 200th, and 500th lattice periods. According to the maximum incoherent tune shift in Eq. (2.13), the incoherent resonance condition predicts that the resonant bare tune reaches approximately 0.3 from 0.25. As is clear from the figure, the stopband does not have such a width. This suggests

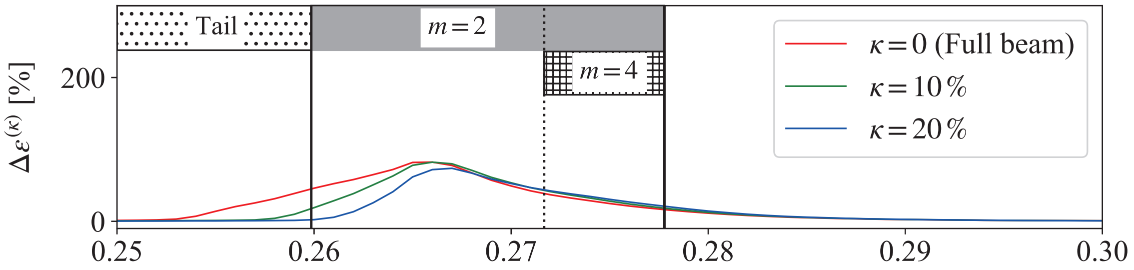

(a) 100th Cell

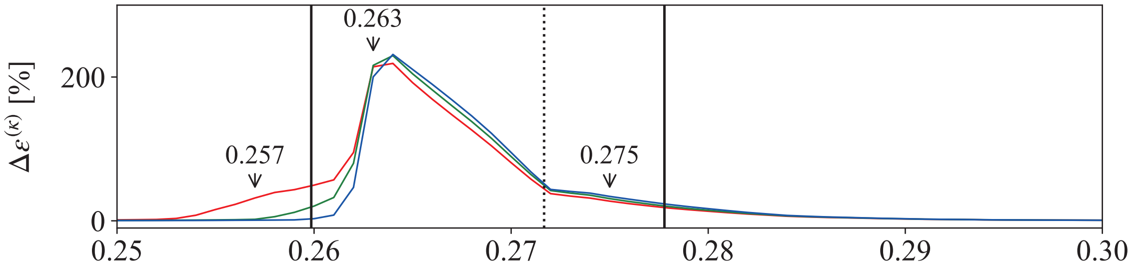

(b) 200th Cell

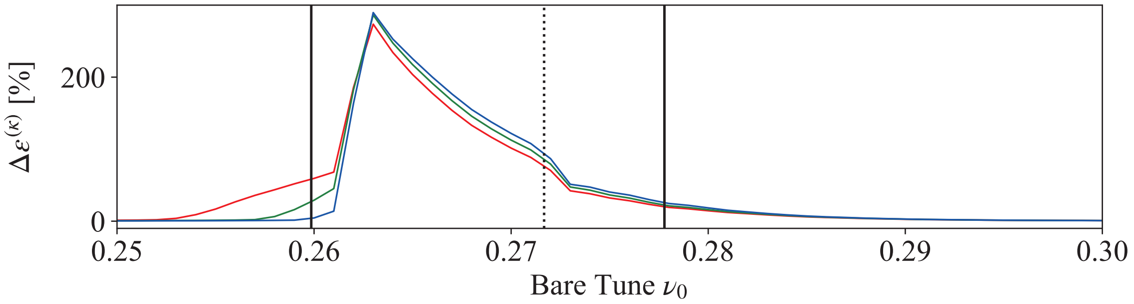

(c) 500th Cell

Figure 3.7: Emittance growths of a Gaussian beam evaluated at the exit of the (a) 100th, (b) 200th, and (c) 500th lattice period.

that the incoherent picture can not be applied to the collective motion of beam core particles as mentioned above. On the other hand, the stopbands evaluated with Eqs. (2.16) and (2.17) are found to be in good agreement with the simulation results. Then the tail resonance region is expected to locate on the lower tune side of the collective 2nd-order resonance stopband and above the single particle 4th-order resonance line ($\nu_0 = 0.25$).

The three curves in each panel are evaluated for different ensembles of particles excluding the outermost particles. We then assumed three truncation factors $\kappa_m = 0\%$, 10%, and 20%. It is confirmed that the emittance growth in the tail region is very sensitive to the truncation factor and eliminated almost completely by disregarding 20% of outermost particles. This strongly suggests that the instability is caused exclusively by the tail particles and is separable from the collective instabilities in the beam core [46]. Contrary to the tail resonance, the emittance growth in the 2nd and 4th collective resonance region seems to be almost independent of the truncation factor.

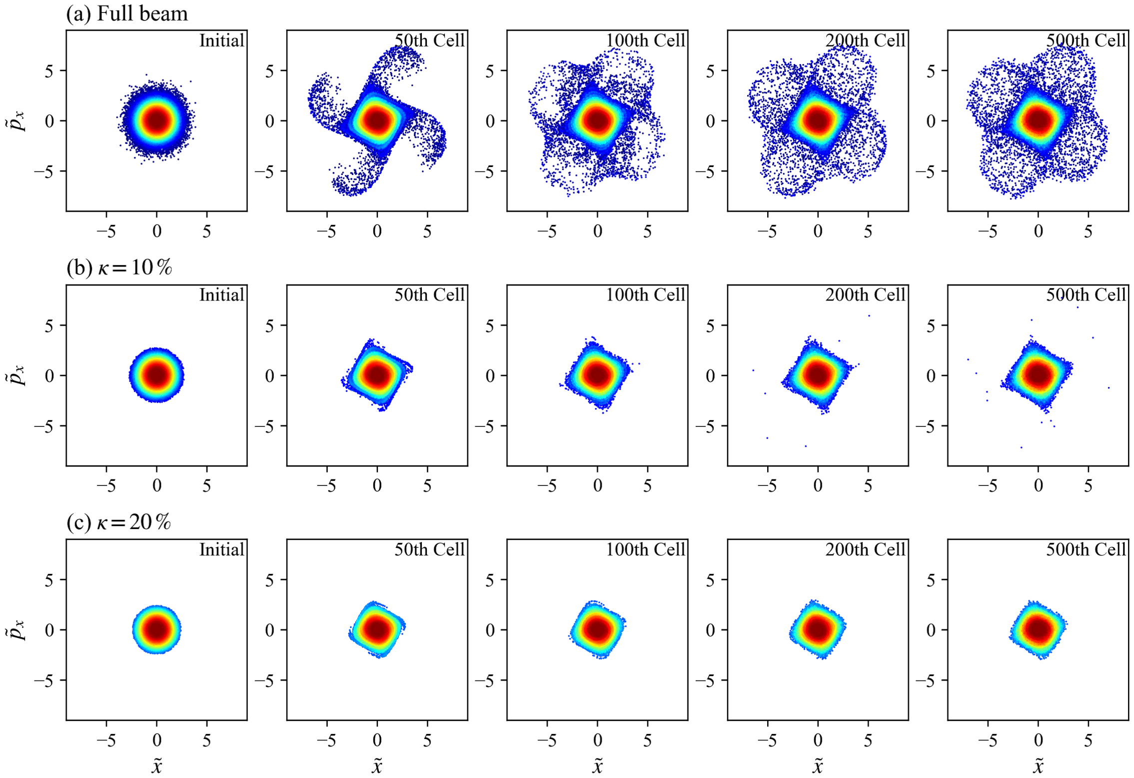

Figure 3.8: Phase space configurations at $\nu_0 = 0.257$ assuming three different truncation factors (a) $\kappa = 0\%$, (b) 10%, and (c) 20%, observed at injection, exit of 50th, 100th, 200th, and 500th cell.

3.4.5 Phase-space configuration

Figures 3.8-3.10 show the typical phase-space configurations in the tail resonance region ($\nu_0 = 0.257$), 2nd-order collective resonance band ($\nu_0 = 0.263$), and 4th-order collective resonance band ($\nu_0 = 0.275$). The abscissa ($\tilde{x}$) and ordinate ($\tilde{p}_x$) are scaled to be dimensionless by their initial rms averages. The particles are color-coded based on their initial E-values. The color varies from red to blue as the initial E-values get larger.

In the case of Fig. 3.8, we can see only the slight deformation of the beam core. On the other hand, the tail particles form a large halo around the beam core. It is confirmed in Fig. 3.8 (b) that the halo consists of 10% of outermost tail particles in the initial phase-space. Fig. 3.11 (a) also shows the emittance growth is solely caused by the tail particles.

The phase-space profile at the bare tune of 0.263 in the 2nd-order collective resonance band fairly differs from the tail resonance case. After the 4th-order resonance, the beam core is found to be deformed into the 2-arm structure, which is peculiar to 2nd-order resonance. It is worth noting that the three distributions obtained with different truncation factors are quite similar after the 200th cell. Thus, the core and tail particles become unstable at the same time as the whole of the beam.

The phase-space profiles near the upper boundary (Fig. 3.10) and below the lower boundary (Fig. 3.8) of the collective instability band are clearly different, although both resonances are of the same 4th-order. In the case of Fig. 3.10, we can see the strong deformation and four-island structure developed inside the beam core. We also find that the core particles spread in a relatively narrow area as wide as the initial beam size with almost no halo particles. In addition,

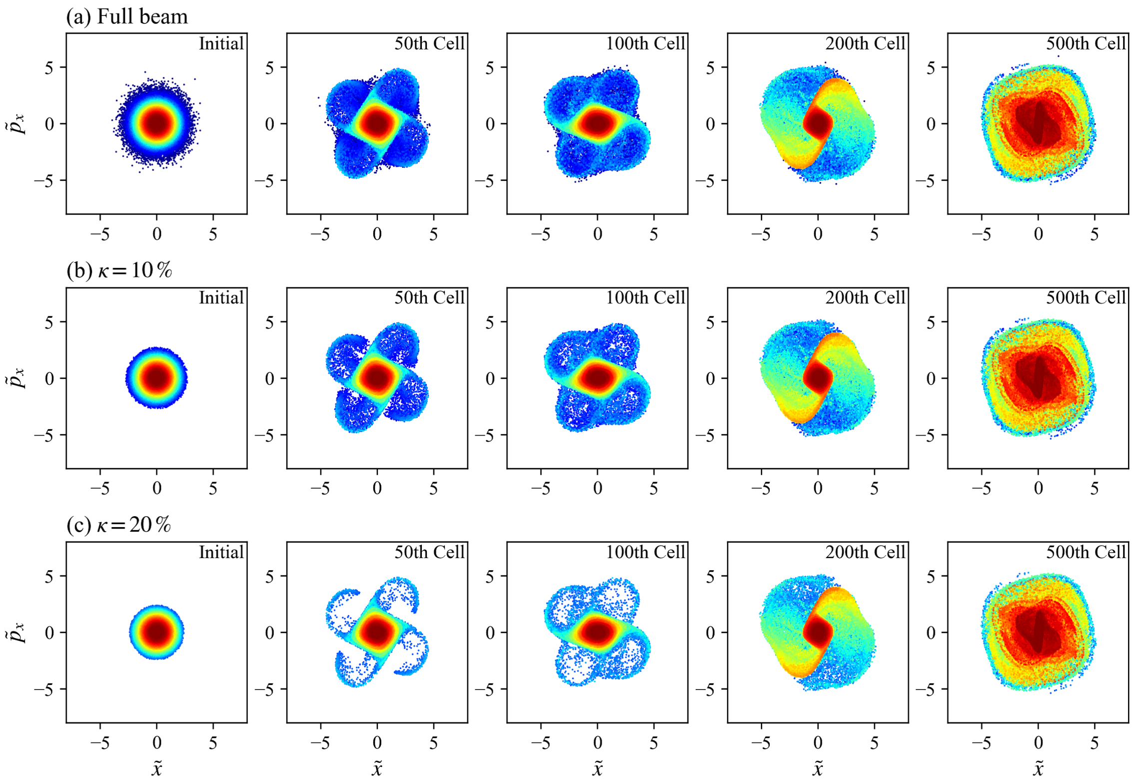

Figure 3.9: Phase space configurations at $\nu_0 = 0.263$ assuming three different truncation factors (a) $\kappa = 0\%$, (b) 10%, and (c) 20%, observed at injection, exit of 50th, 100th, 200th, and 500th cell.

it is observed in Figs. 3.10 and 3.11 that the emittance growth and the phase-space profile are hardly affected by the truncation factor similar to the case of Fig. 3.9. These results suggest that the resonance at $\nu_0 = 0.275$ develops rather collectively than individually, unlike the tail resonance at $\nu_0 = 0.257$.

3.4.6 Incoherent tune spread

In the last subsection, it is confirmed that there are two families of resonance mechanisms driven by the space charge force namely the incoherent resonance in the tail region and the coherent collective resonance. The instabilities at $\nu_0 = 0.263$ and $\nu_0 = 0.275$ are classified in the former, at $\nu_0 = 257$ is classified in the latter. These results are consistent with our discussion in Sec. 3.4.2 and the theoretical predictions based on the Vlasov analysis.

According to the incoherent resonance condition, the upper boundary of the stopband in the case of Fig. 3.7 is $\nu_0 = 0.3$; the operating point is generally not chosen in the range $0.25 \leq \nu_0 \leq 0.3$. On the other hand, we detect only negligible emittance growth outside the collective instability band despite the core deformation as shown in Fig. 3.12. This figure depicts the incoherent tune spread when the operating point is set at 0.29 beyond the upper boundary of the collective instability band. The incoherent tunes are evaluated using Fourier transform technique. The incoherent tune spread lies on the 4th-order single-particle resonance line, and the particles moved above the resonance line. It is clear that the core particles satisfy the incoherent resonance condition in Eq. (3.5), but the emittance growth at the exit of the 1000th cell is less than a few percent. Thus, there is little practical importance to caring about

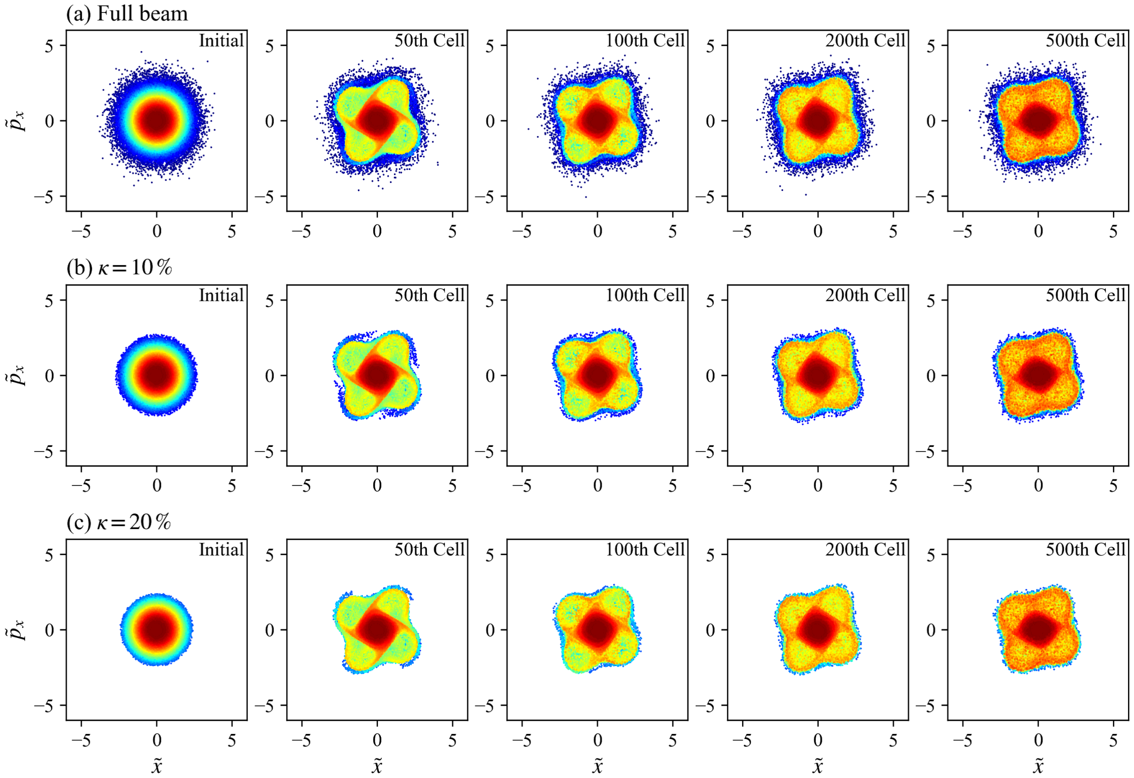

Figure 3.10: Phase space configurations at $\nu_0 = 0.275$ assuming three different truncation factors (a) $\kappa = 0\%$, (b) 10%, and (c) 20%, observed at injection, exit of 50th, 100th, 200th, and 500th cell.

such distortion of the incoherent tune spread.

Figure 3.13 shows examples of the incoherent tune spreads in the 2nd-order and 4th-order collective resonance bands ($\nu_0 = 0.263$ and 0.275) for comparison. In this case, we used the orbit data of individual particles from the 300th cell to the 1300th cell after the collective instabilities roughly settled; these incoherent tune spreads are expected to remain almost unchanged after the 300th cell. We find that a lot of particles located initially much below the resonance lines $\nu_{0x(0y)} = 1/4$ moved above them. In particular, it turns out from Fig. 3.13 (a) that only a few particles remain below the resonance lines. In the case of Fig. 3.13 (b), we also notice that the tune region where the particles are affected by the resonance instability is much wider than in the case of Fig. 3.12.

Figure 3.14 displays another example of nonlinear collective instability at $\nu_{0x(0y)} = 0.192$ with a well-matched waterbag beam. In this example, the tune depression adjusted at 0.8. As is evident from Fig. 3.4 (a), the operating point is set in the 3rd-order collective instability band. Then, the orbits of an individual particle between the 500th and 1500th are Fourier analyzed to evaluate their incoherent tunes. The right panel indicates that the resonance instability affects the particles having a much lower incoherent tune than the single particle resonance condition $\nu_{0x(0y)} = 1/6$, which is very similar to the 4th-order case in Fig. 3.13 (b).

These results suggest that the reason why the particles cross the resonance line and are accumulated near or above $\nu_{0x(0y)} = 1/4$ is not necessarily responsible for the incoherent effect. Recalling the tune spread configurations after redistribution due to the collective instabilities shown in Figs. 3.13 and 3.14, the resonance effect appears rather well below the resonance line

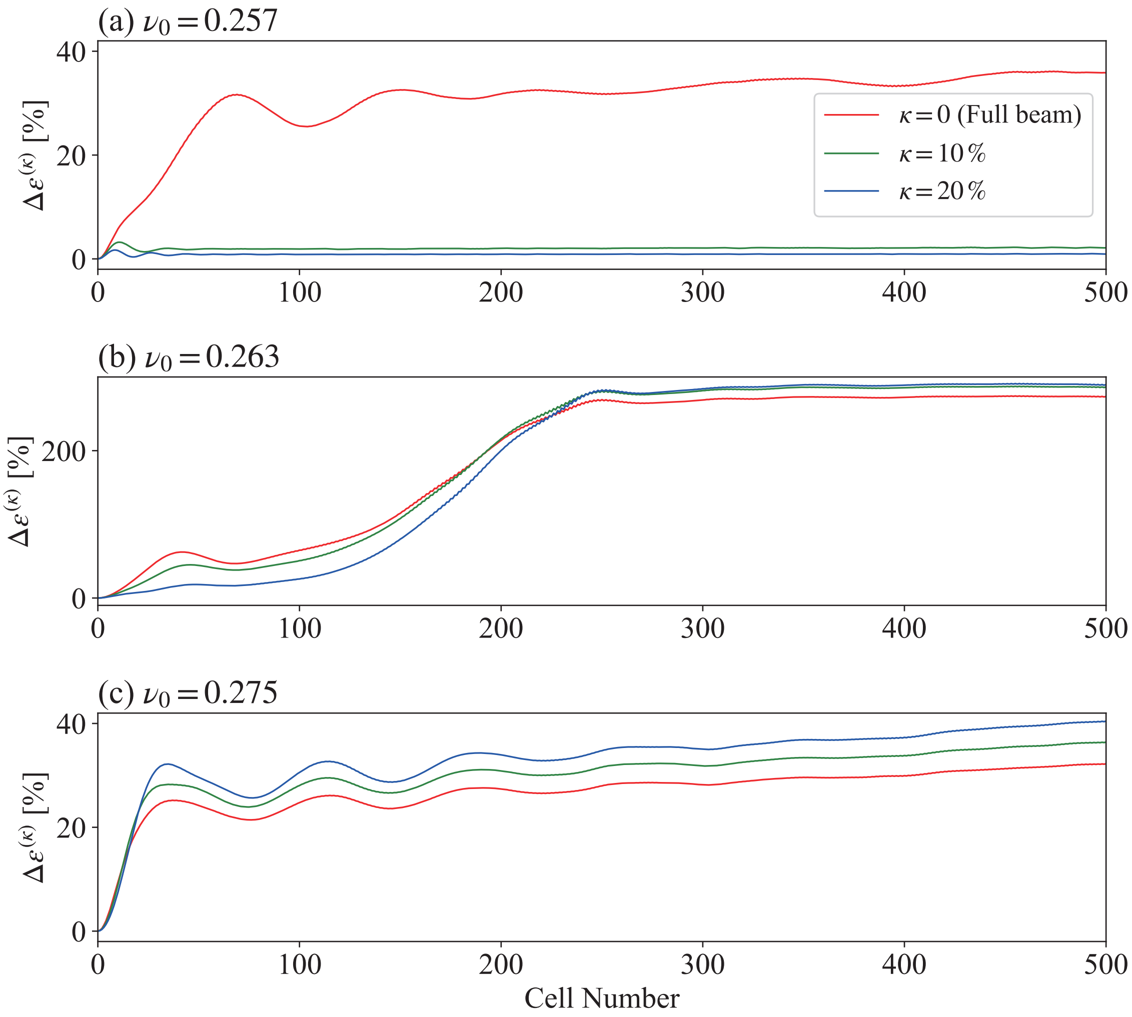

Figure 3.11: Time evolutions of the rms emittance-growth rates at the operating bare tunes of (a) $\nu_0 = 0.257$, (b) 0.263, and (c) 0.275.

than on the resonance line. Based on the incoherent picture, it is difficult to interpret the results that the resonance instability affects the particles not on the resonance line but well below it.

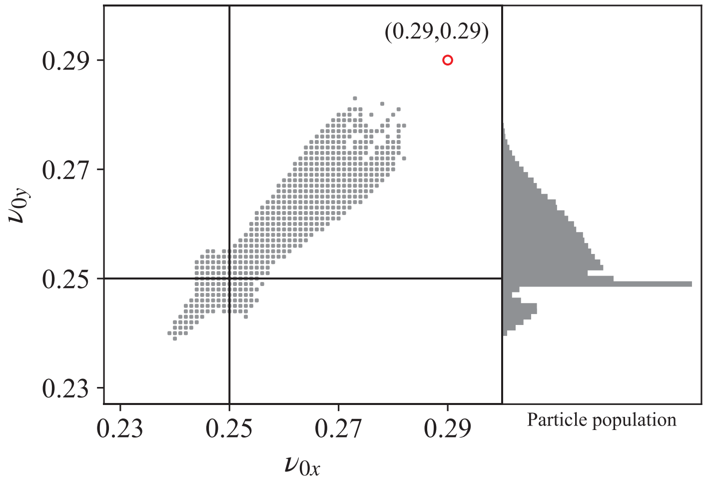

Figure 3.12: Incoherent tune spread of a Gaussian beam at the operating tune of $\nu_0 = 0.29$. The initial tune depression is adjusted at $\eta = 0.9$.

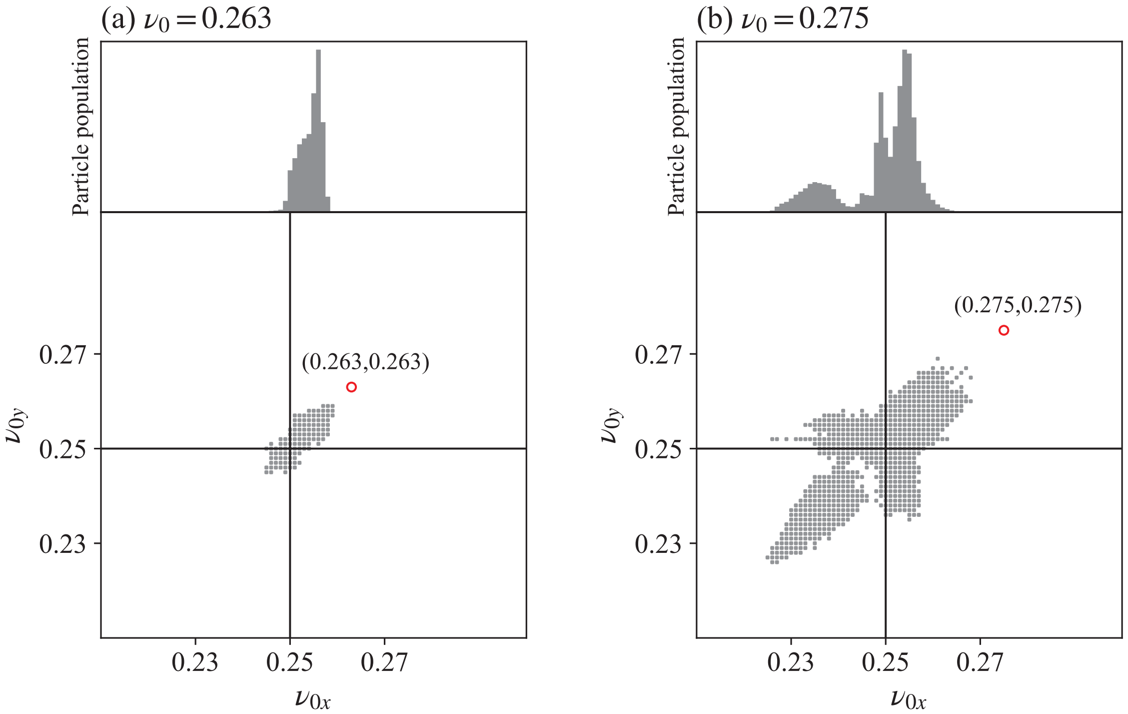

Figure 3.13: Incoherent tune spread of a Gaussian beam at the operating tune of (a) $\nu_0 = 0.263$ and (b) 0.275. The initial tune depression is adjusted at $\eta = 0.9$, similarly to the cases of Figs. 3.9 and 3.10.

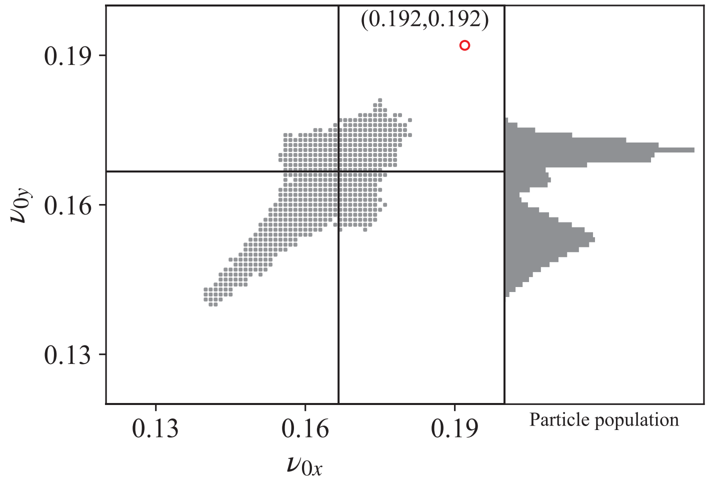

Figure 3.14: Incoherent tune spread of the waterbag beam after the development of the coherent 3rd-order resonance is settled. All simulation conditions are the same as employed in Fig. 3.4 (a).

3.5 Resonance instabilities in an ideal AG lattice

We now explore the resonance instabilities on the ν_{0x}-ν_{0y} plane. The horizontal and vertical motions are no longer symmetric, and the beam parameters such as bare tunes, emittances, and tune depressions are not necessarily equal in the horizontal and vertical directions. In this section, we employ the W$_{\text{ARP}}$ code again and conducted systematic numerical simulations of charged particle beam propagating through a sinusoidal focusing force same as in the previous section for simplicity.

3.5.1 Stop band distribution in tune space

In this section, we try to investigate whether the hypothesis of 2D-coherent resonance condition in Eq. (3.1) can predict the approximate stopband distributions on the ν_{0x}-ν_{0y} plane. In order to reveal the precise positions of stopbands, a series of self-consistent numerical simulations is performed over a wide tune range.

Stop bands with fixed tune depression

Assuming horizontal and vertical tune depressions are equal and fixed over the whole tune space, we can simplify the coherent resonance conjecture as

$$k\nu_{0x} + \ell\nu_{0y} = \frac{n}{2} \cdot \frac{1}{1-(1-\eta)C_m} . \tag{3.12}$$

As is obvious from this equation, the resonance conditions are expected to be straight lines on ν_{0x}-ν_{0y} plane. Figure 3.15 shows the result summarizing the simulations with about five thousand (71×71) of different combinations of operating tunes ν_{0x} and ν_{0y}. The tune depression is fixed at 0.9 for all operating points. The visible instability bands are found to be straight as consistent with the prediction in Eq. (3.12).

The most conspicuous two stopbands near $\nu_{0x(0y)} = 0.25$ are the envelope instabilities, and their serious emittance growths should be attributed mainly by 2nd-order collective resonances with $(k, \ell, n) = (2, 0, 1)$, $(0, 2, 1)$. The 2nd-order mode is expected to appear accompanied by the 4th-order or higher modes, but they are much weaker than the 2nd-mode instability as discussed in the previous section. The serious emittance growth that appears along the resonance line with $(k, \ell, n) = (1, 1, 1)$ should also be exclusively due to the 2nd-order collective resonance. However, another 2nd-order instability with $(k, \ell, n) = (1, -1, 0)$ that is expected to appear on the diagonal of Fig. 3.15 is almost invisible. The reason for the disappearance of the 2nd-order different resonance is that the horizontal and vertical emittances are equal along the diagonal line $\nu_{0x} = \nu_{0y}$. The symmetric different resonance can not develop in such an isotropic beam. This is also confirmed experimentally by using the S-POD [32].

The eight noticeable instabilities except for 2nd-order modes can be explained by considering lowest-order nonlinear ($m = 3$) modes with $(k, \ell, n) = (3, 0, 1)$, $(0, 3, 1)$, $(3, 0, 2)$, $(0, 3, 2)$, $(2, -1, 0)$, $(-1, 2, 0)$, $(2, -1, 1)$, and $(-1, 2, 1)$. The possible other 3rd-order resonances with $(k, \ell, n) = (2, 1, 1)$, $(1, 2, 1)$, $(2, 1, 2)$, and $(1, 2, 2)$ are hardly observable in Fig. 3.15, but we can detect a few percent of emittance growth attributed by them. The effects of overlapping 6th-order or higher-order resonances should be negligible compared with the ones of 3rd-order resonances.

The tune diagram in Fig. 3.16 is obtained with a waterbag beam. In order to encourage the development of collective instabilities and observe resonance instabilities in 100 lattice periods, the particle distribution is initially weakly distorted by applying 3rd-order nonlinear potential proportional to $x^3 - 3xy^2$ in this case. Similarly to the result in Fig. 3.15, almost all observable stopbands can be identified as 2nd-order or 3rd-order resonances. We found that the stopband widths are narrower than the Gaussian case. This is due to the tail resonance region as discussed in Sec. 3.4. It is thus confirmed that there is no intrinsic difference in the resonance features of Gaussian and waterbag beams.

It is important to note that all of the observed stopbands can be explained as 2nd-order or 3rd-order resonances. If the right-hand side of the coherent resonance condition in Eq. (3.15) is not half integers but integers, we have to introduce 4th-order or 6th-order resonances to interpret the simulation results in Fig. 3.15. Then, the troublesome question may be raised why many missing 4th-order and 6th-order resonances exist. In addition, it is also unnatural that the stopbands of 5th-order resonances are completely invisible even though 6th-order resonances can be detectable.

In Fig. 3.15, we can see that the stopbands shift induced by space-charge force. For reference, we have plotted indices of the stopband shift for two resonance conditions; namely the coherent resonance condition in Eq. (3.1) and the incoherent resonance condition in Eq. (2.12). We introduce the equation $\Gamma_{k\ell}(\Delta_x, \Delta_y)$ defined as

$$\Gamma_{k\ell}(\Delta_x, \Delta_y) \equiv k(\nu_{0x} - \Delta_x) + \ell(\nu_{0y} - \Delta_y) = \frac{n}{2}\,. \tag{3.13}$$

$\Gamma_{k\ell}(0, 0)$ then indicates the single-particle resonance condition except for the $1/2$ factor on the right-hand side and is plotted with a solid line. The dashed lines correspond to the former and given with $\Gamma_{k\ell}(\Delta\overline{\nu}_x, \Delta\overline{\nu}_y)$. Thus, the line indicates the resonant tunes predicted by the coherent resonances condition assuming $C_m = 1$. The dash-dotted lines also correspond to the latter and are given with $\Gamma_{k\ell}(\max(\Delta\nu_x), \max(\Delta\nu_y))$ where $\max(\Delta\nu_{x(y)})$ is maximum incoherent

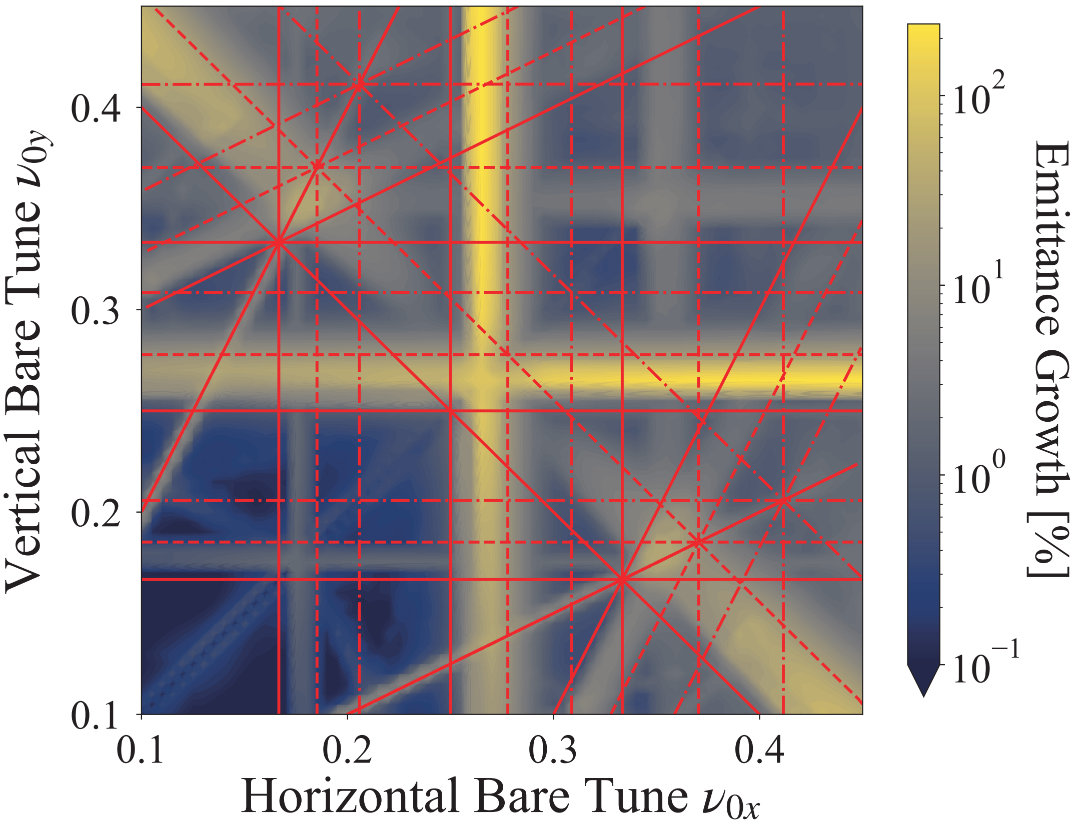

Figure 3.15: Tune diagram obtained from 2D WARP simulations with Gaussian beam. The rate of rms emittance growth evaluated at the exit of the 100th cell is color-coded. The tune depression is initially adjusted at $\eta_{x(y)} = 0.9$ over the whole tune space. The solid, dashed, and dash-dotted lines in the diagram are obtained from Eq. (3.13) with $\Delta_{x(y)} = 0$, $(1 - \eta_{x(y)})\nu_{0x(0y)}$, and $(1 - \eta_{x(y)}^2)\nu_{0x(0y)}$ respectively.

tune shift in the Gaussian distribution evaluated from Eq. (2.13). Here the line indicates the upper boundary of the stopband unlike in the former case. Based on the incoherent picture, we should avoid putting the operating point inside the region between the dash-dotted line and the solid line. It is, however, found that the actual stopband width is much narrower than the prediction. The conventional incoherent manner thus tends to be overestimating the stopband width considerably. Moreover, the stopband widths seem to depend on the resonance orders; in other words, the stopband widths are not determined by the size of the tune spread. This implies the instabilities in the beam core can not be described by the incoherent manner. We also see that the observable stopbands are almost within the region between the dashed lines and solid lines. Thus, the resonant tunes may be predicted well by the coherent resonance condition with the tune shift factor smaller than one.

Stop bands with fixed beam intensity

In a practical accelerator, the beam current and emittances are not varied arbitrarily but are determined by injection configurations such as the performance of ion sources and pre-accelerators. Thus, we next assume the case where the beam current and initial emittances remain constants regardless of the operating tunes. Figure 3.17 shows the emittance growth at the exit of the 100th lattice period in this practical situation. For simplicity, the horizontal and vertical initial

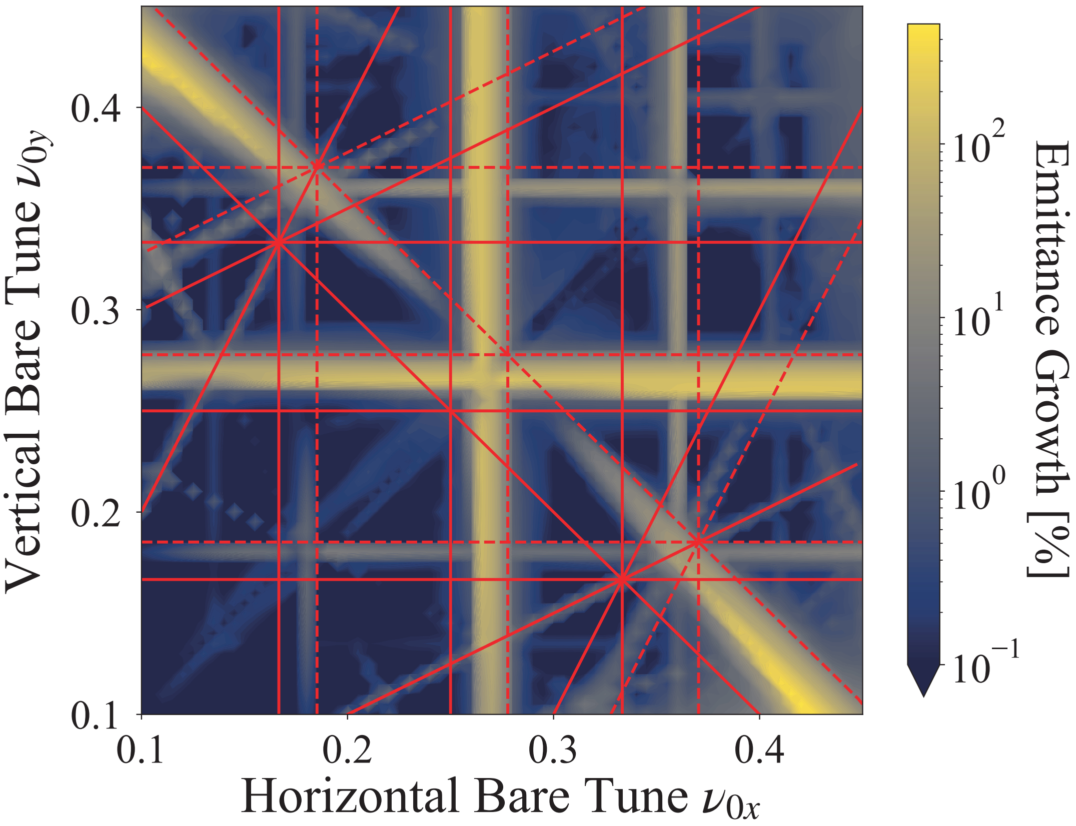

Figure 3.16: Tune diagram obtained from 2D WARP simulations with weakly distorted waterbag beam. Other conditions and the definitions of the red lines are the same as those assumed for the case of Fig. 3.15.

emittances are set equal. The beam current is adjusted so that the initial tune depression ($\equiv \eta_{1/6}$) at the operating tunes of $(\nu_{0x}, \nu_{0y}) = (1/6, 1/6)$ is equal to 0.9. In this case, the resonance lines defined by Eq. (3.1) are no longer straight since the initial tune depression depends on the operating tunes. The major 2nd and 3rd-order stopbands shown in Fig. 3.17 are also observable in Fig. 3.15. In addition to them, we notice the weak instabilities of 4th-order resonances with $(k, \ell, n) = (4, 0, 3)$ and $(0, 4, 3)$.

The resonance line curves induced by the shift of tune depression are enhanced by increasing the initial beam current. Figure 3.18 shows the tune diagram assuming three different initial beam currents corresponding to $\eta_{1/6} = 0.9$, 0.8, and 0.7. Unlike the case of $\eta_{1/6} = 0.9$, we can observe significant bending of the stopband and the resonance line for the other two cases. We here focus on the 2nd-order resonance stopband above $\nu_{0x} = 1/4$ for example. The dotted lines for each panel denote the resonant tune predicted by the coherent resonance condition with the tune shift factors $C_2 = 0.75$ (red) and $C_2 = 0.5$ (black). These numbers are derived from rms envelope Eq. (2.4) and correspond to so-called quadrupole mode and breathing mode respectively [7,23]. However, we can not observe additional instability of 2nd-order resonance overlapping the stopband whose tune shift factor is predicted to be slightly below 0.75. In the case of Fig. 3.18, we also can not detect the second peak comparable to the peak of over 400% emittance growth. The breathing mode instability thus appears to hardly develop in a quadrupole channel. Therefore, it should be sufficient to assign a single value to C_2 in practical applications.

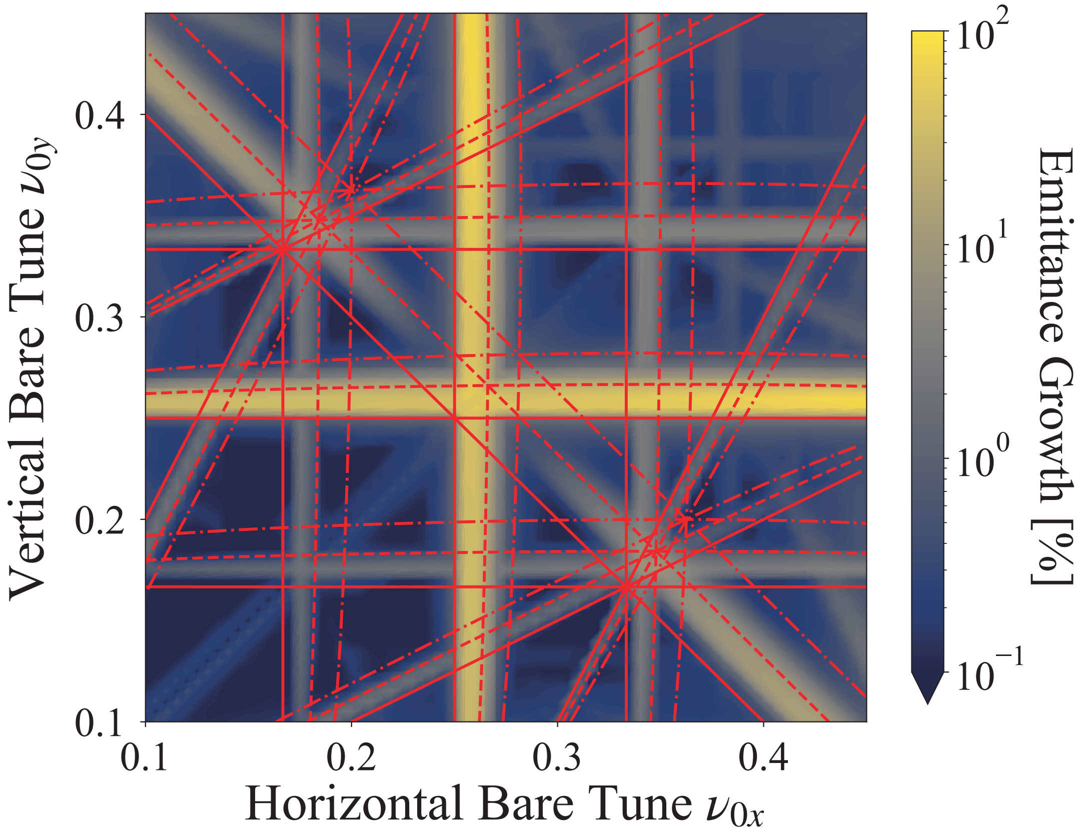

Figure 3.17: Tune diagram obtained from 2D WARP simulations with Gaussian beam. The line density and initial emittances are fixed at the value that gives $\eta_{x(y)} = 0.9$ with the operating tunes $(\nu_{0x}, \nu_{0y}) = (1/6, 1/6)$. Other conditions and the definitions of the red lines are the same as those assumed for the case of Fig. 3.15.

Stop bands of the initially equipartitioned beam

The equipartitioning case, in which the beam effective temperatures in three degrees of freedom are set equal, is also physically interesting to us. When the beam is initially equipartitioned, the following equation is satisfied at injection [13]

$$\frac{\varepsilon_x}{\varepsilon_y} = \frac{\eta_y \nu_{0y}}{\eta_x \nu_{0x}} . \tag{3.14}$$

Figure 3.19 summarizes the simulation results with the initial beam parameters determined by Eq. (3.14). The initial beam current and the initial emittance that is the greater of the horizontal and vertical directions are set at the same value as assumed in Fig. 3.17. We can see that the resonance lines bend in the opposite direction to the case of Fig. 3.17. The tendency is enhanced by assuming a higher beam current as shown in Fig. 3.20. It is found that the coherent resonance condition in Eq. (3.1) successfully reproduces the feature of stopband distribution again.

Disappearance of difference resonances

It is worth noting that the two 3rd-order difference resonance bands with $(k, \ell, n) = (2, -1, 0)$ and $(-1, 2, 0)$ can not be detected in Fig. 3.19, even though other major stopbands are observable as well as previous cases. Figure 3.21 shows that the difference resonances remain

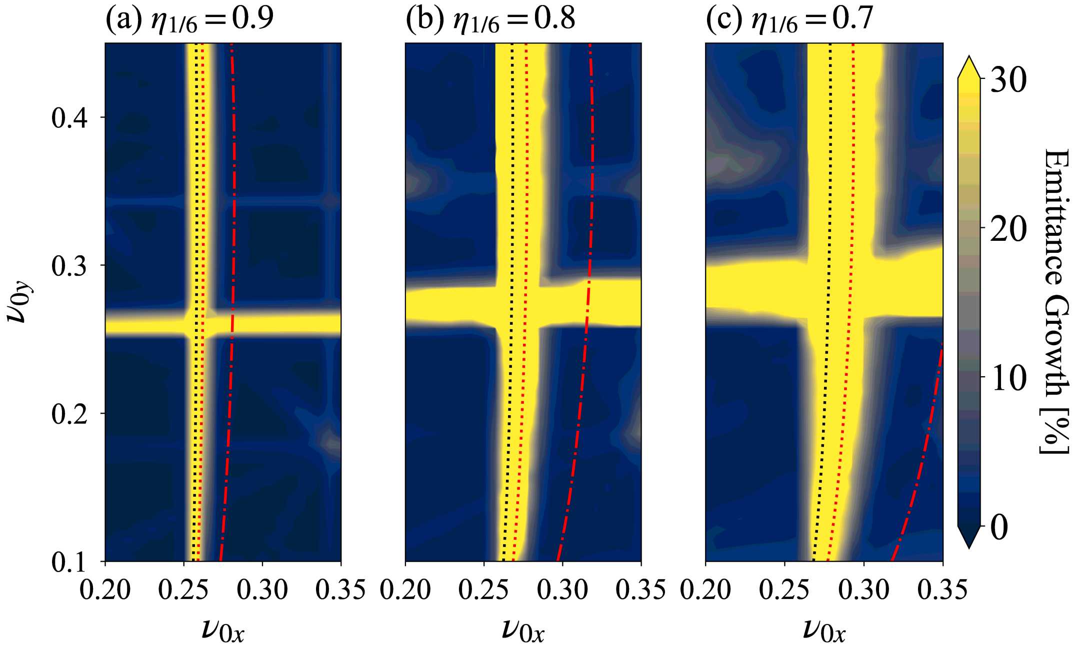

Figure 3.18: Beam intensity dependence of the envelope-instability stopband obtained from 2D WARP simulations with Gaussian. The initial beam parameters are determined in the same way as in the case of Fig. 3.17. The tune depressions are adjusted to (a) $\eta_{x(y)} = 0.9$, (b) 0.8, and (c) 0.7 with the operating tunes $(\nu_{0x}, \nu_{0y}) = (1/6, 1/6)$. The dotted lines are the theoretical prediction from Eq. (3.1) for the 2nd-order resonance assuming the tune shift factors $C_2 = 0.75$ (red) and $C_2 = 0.5$ (black).

unobservable if we apply an external nonlinear potential proportional to $x^3 - 3xy^2$ to enhance them. Here we introduce a quantity $I_{k\ell}$ defined as

$$I_{k\ell} \equiv \frac{\varepsilon_x}{k} + \frac{\varepsilon_y}{\ell} \,. \tag{3.15}$$

Figure 3.21 (b) shows the contour plot of $I_{k\ell}$. We recognize from this figure that the contour of $I_{k\ell} = 0$ almost corresponds to the 3rd-order difference resonance line with $(k, \ell, n) = (-1, 2, 0)$. We also confirmed that $I_{k\ell} = 0$ is satisfied along the resonance line with $(k, \ell, n) = (2, -1, 0)$. Moreover, it can be seen from Figs. 3.15, 3.17, and 3.19 that the case of 2nd-order difference resonance with $(k, \ell, n) = (1, -1, 0)$ also follows this rule. The space-charge driven difference resonance that occurs under the condition $\nu_{0x} = \nu_{0y}$ is referred to as the “Montague resonance” [47, 48]. Ion trap experiments also have shown that the Montague resonance is hardly activated when the horizontal and vertical emittances are approximately equal [32]. Another example is shown in Fig. 3.22 in which the initial emittance ratio $\varepsilon_x/\varepsilon_y$ is fixed at 1/2. The simulation results with and without external nonlinear driving field proportional to $3x^2y - y^3$ are shown in the right and left panels respectively. Then, $I_{k\ell} = 0$ is fulfilled along the resonance lines with $(k, \ell, n) = (2, -1, 0)$ and $(2, -1, 1)$, and we can see that the corresponding stop bands disappear in both cases. Thus, it is obvious that the quantity $I_{k\ell}$ is seriously correlated to the disappearance of difference resonances. Since $I_{k\ell}$ is free from intensity-dependent parameters, the present finding is expected to be able to apply regardless of the beam current.

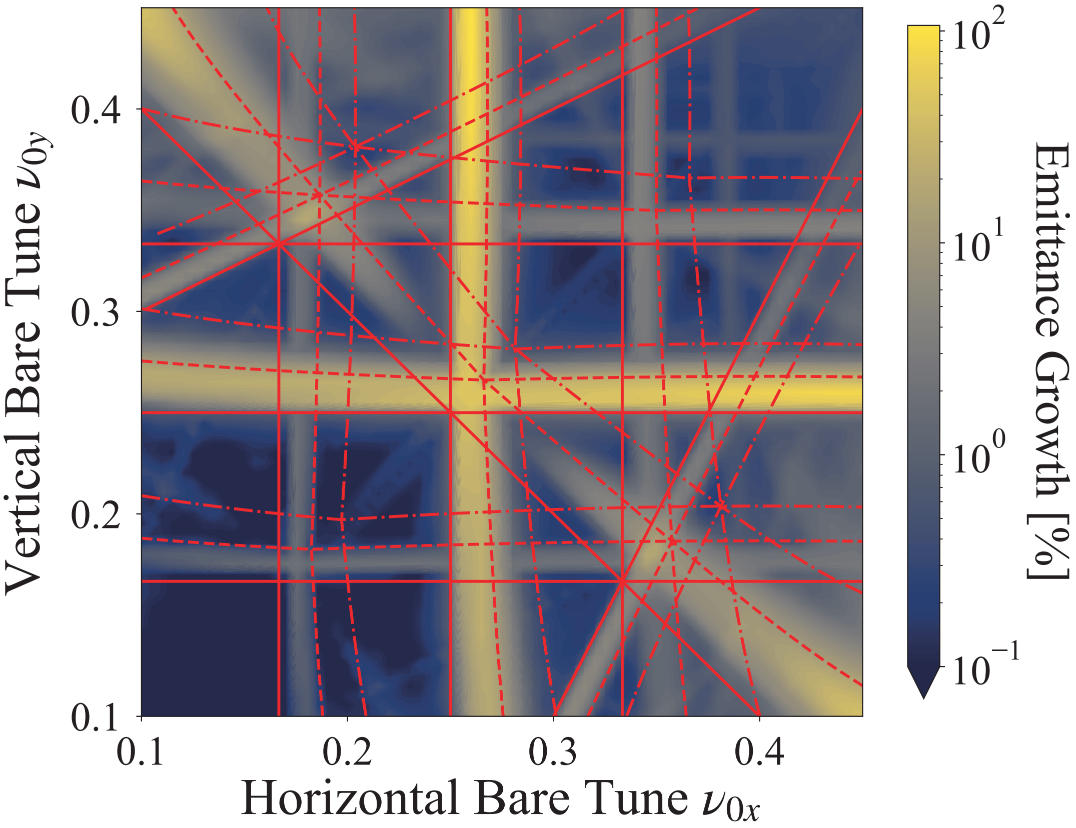

Figure 3.19: Tune diagram obtained from 2D WARP simulations with Gaussian beam. The initial emittances are chosen so as to meet the equipartitioning condition in Eq. (3.14). The line density is fixed at the value that gives $\eta_{x(y)} = 0.9$ with the operating tunes $(\nu_{0x}, \nu_{0y}) = (1/6, 1/6)$. Other conditions and the definitions of the red lines are the same as those assumed for the case of Fig. 3.15.

3.5.2 Evaluation of low order tune shift factors

The Okamoto and Yokaya theory suggests that the tune shift factor does not depend on whether the resonance is driven by the external field or self-field, as long as the external non-linearity can be treated as a perturbation. We assumed the theoretical prediction for a 1D beam is also valid in the 2D case. Then, the extension of the 1D coherent resonance condition with mth-order nonlinear external driving field in Eq. (2.18) to a 2D beam can be written as

$$k(\nu_{0x} - C_m \Delta\bar{\nu}_x) + \ell(\nu_{0y} - C_m \Delta\bar{\nu}_y) = |n \pm \kappa_m|, \tag{3.16}$$

where κ_m is the frequency per one lattice period. In computer simulations, we can take an arbitrary number of κ_m, unlike in a real circular accelerator where the periodicity of the external driving field is limited by its structure. We here introduce an external driving field in addition to the sinusoidal linear focusing force, in order to identify the resonance condition numerically and evaluate low-order tune shift factors. This has two advantages over relying on the self-field. First, we can avoid the overlapping of resonance instabilities of different orders by choosing a proper number of κ_m and the operating point. As mentioned in the last section, the self-field-driven mth-order resonance occurs accompanied by 2mth-order resonances. Since the tune shift factor depends on the resonance order, the overlapping may degrade the evaluation accuracy of

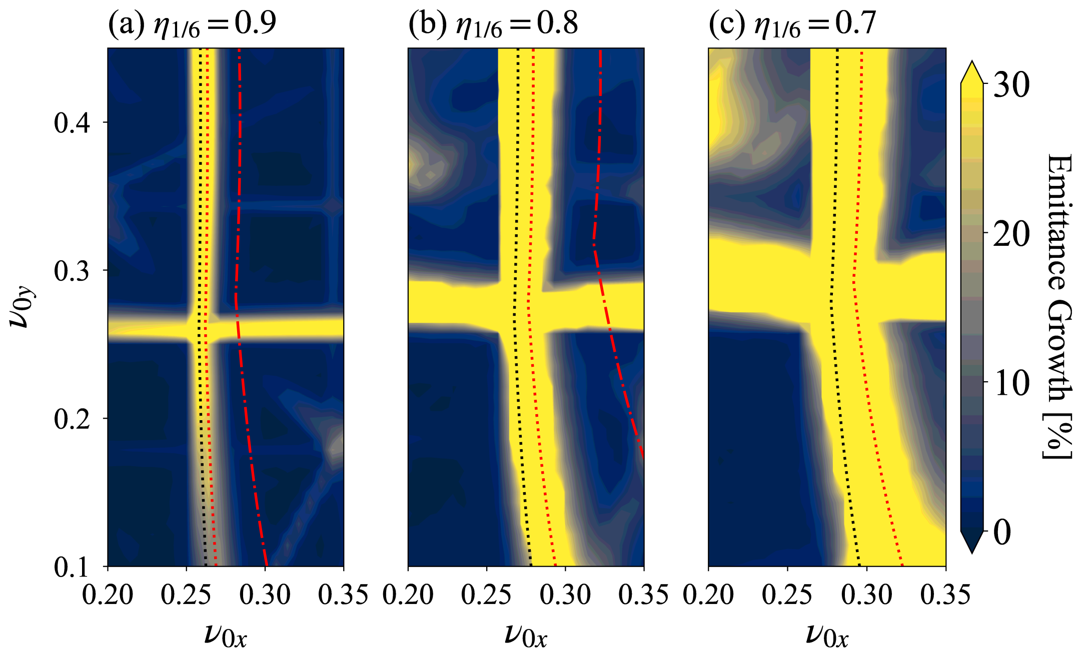

Figure 3.20: Beam intensity dependence of the envelope-instability stopband obtained from 2D WARP simulations with Gaussian. The initial beam parameters are determined in the same way as in the case of Fig. 3.19. The tune depressions are adjusted to (a) $\eta_{x(y)} = 0.9$, (b) 0.8, and (c) 0.7 with the operating tunes $(\nu_{0x}, \nu_{0y}) = (1/6, 1/6)$. The definitions of the red and black lines are the same as those assumed for the case of Fig. 3.18.

the tune shift factor. Second, the resonance strength is controllable independently of the beam intensity. In particular, self-field-driven 4th-order resonances may be too small to locate their stopbands.

We expect the tune shift factors to be independent of the distribution function. In order to verify that the difference in the particle distribution does not cause a significant change in the evaluated value of tune shift factors, we employ the parabolic and waterbag beams in addition to the Gaussian beam in this section.

3.5.3 Non-coupling resonance

Let us first look at the non-coupling resonance cases where the horizontal and vertical motions are symmetric. The horizontal and vertical tune depression are set equal; namely $\eta_x = \eta_y (\equiv \eta)$. We keep the operating point at $(\nu_{0x}, \nu_{0y}) = (0.15, 0.15)$ where the significant emittance growth does not occur for the range of $0.8 < \eta < 0.95$ unless the external driving force is not applied. Then the resonance condition in Eq. (3.16) can be simplified as

$$m(\nu_0 - C_m \Delta\bar{\nu}) = |n \pm \kappa_m|, \tag{3.17}$$

where $\Delta\bar{\nu} = (1 - \eta)\nu_0$ represents the rms tune shift in the horizontal and vertical direction. A nonlinear perturbation can drive several resonances at the same time, but it may be sufficient for our purpose to focus on the most severe resonance with $n = 0$ at

$$m\nu_0 = \frac{\kappa_m}{1 - (1 - \eta)C_m}. \tag{3.18}$$

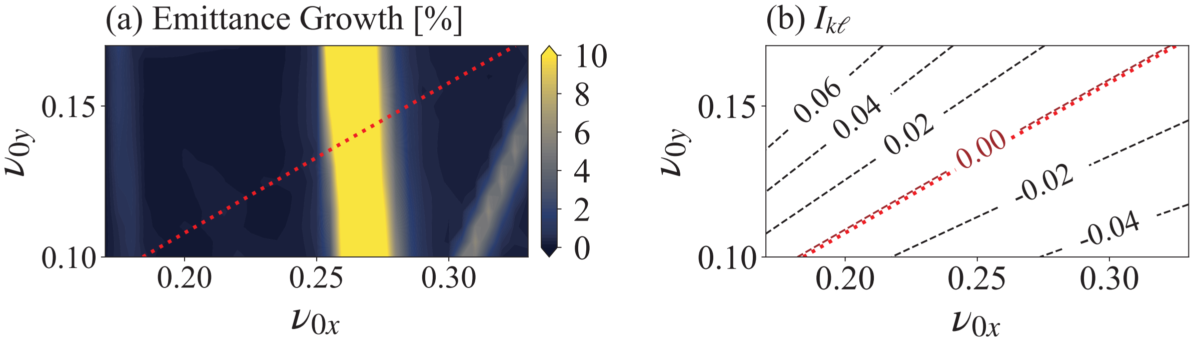

Figure 3.21: (a) 2D WARP simulation results obtained with Gaussian beam. The conditions are the same as those assumed for the case of Fig. 3.17 except that a 3rd-order nonlinear field proportional to $x^3 - 3xy^2$ is added. (b) Contour plot of $I_{k\ell}$ defined by Eq. (3.16). The number in panel (b) indicates the value of $I_{k\ell}$ in a unit of mm·mrad. The red dotted line is the theoretical prediction from Eq. (3.1) for the 3rd-order resonance assuming the tune shift factor of $C_3 = 0.875$.

This suggests that we can locate the mth-order resonance band by scanning the perturbation frequency κ_m.

We now try to estimate the low-order tune shift factors C_m by applying an external perturbation field. However, the precise estimation is not so easy due to several reasons. We show an example of the emittance behavior driven by the 2nd-order perturbation in Fig. 3.23. The emittance growths at the exit of the 200th lattice period are plotted. The sawtooth-like configurations of the emittance growth curves are due to the stop band shifts caused by the beam density reduction as discussed in Sec. 3.4. This makes it difficult to evaluate the initial stopband location. Considering that the resonance instability makes the tune depression approach unity, the C_m is inevitably estimated to be less than the correct value. Moreover, we see that the stopbands of the Gaussian beam in Fig. 3.23 (a) are clearly different from the others and are expanded toward upper thresholds $\kappa_2 = 0.3(= 2\nu_0)$ given by the single particle resonance condition. We even observe a second peak in the $\eta = 0.9$ case. It is apparent from Fig. 3.24 that the peculiarity of the Gaussian beam originates from the tail particles. The emittance growth curves are deformed to the dashed lines by disregarding only 5% of outermost particles that are identified with E-value in Eq. (3.10) in the emittance calculation. We can see that the second peak is almost completely eliminated by only 5% of removal in the $\eta = 0.9$ case. The emittance growth on the higher κ_2 side is also significantly lowered in the $\eta = 0.8$ case. In both cases, the highest peaks are hardly affected by removing halo particles. These results are quite similar to the case in Sec. 3.4 and suggest the existence of the tail resonance region.

It is important for a better estimate of the C_m to suppress the effect from stopband shift and the tail resonance. We here define the resonant κ_m of mth-order coherent resonance as the point that reaches one percent of emittance growth at first. The one-percent level is expected to have only a negligible effect on the stopband shift. We also expect that no significant halo develops in such a short time. On the other hand, the tail particle of the Gaussian beam may cause percent level emittance growth before the collective resonance develops. We thus truncate one percent of the outermost particle defined with E-value in Eq. (3.10) at injection, in order to mitigate the tail resonance effect.

Figure 3.25 shows the emittance growth evaluated with the WARP code on κ_2-η plane. The

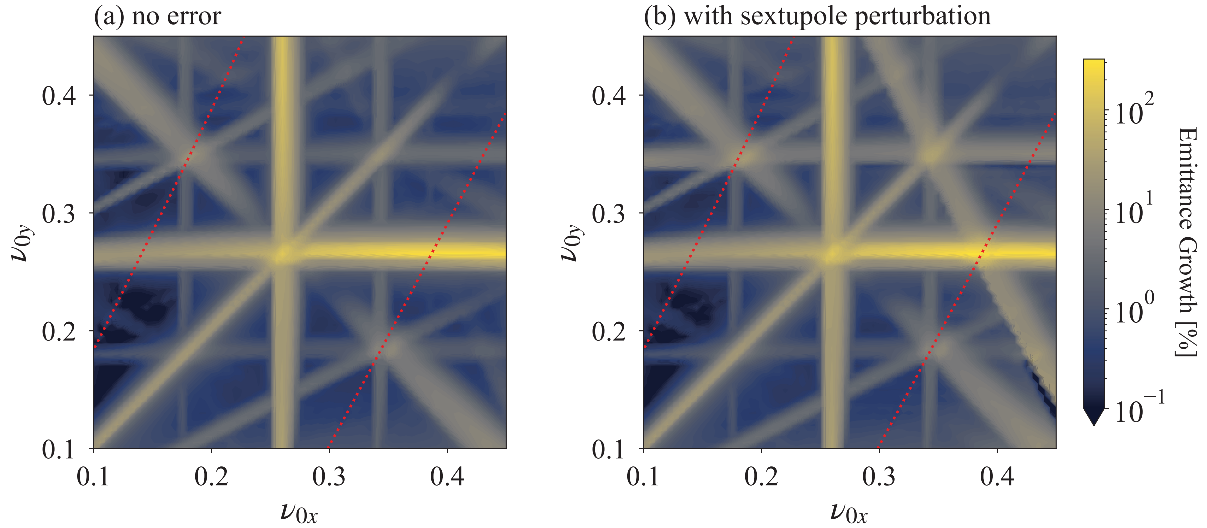

Figure 3.22: Tune diagram obtained from 2D WARP simulations with Gaussian beam. The initial emittance ratio is fixed at $\varepsilon_x/\varepsilon_y = 1/2$ over the whole tune space. The line density is set at the same value as assumed in Fig. 3.17. The red dotted line is the theoretical prediction from Eq. (3.1) for the 3rd-order coupling resonances with $(k, \ell, n) = (2, -1, 0)$ and $(2, -1, 1)$ assuming the tune shift factor of $C_3 = 0.875$. The external field is completely linear in the case of the panel (a). A 3rd-order nonlinear field proportional to $x^3 - 3xy^2$ is added in the case of the panel (b).

center of the 2nd-order stopband lies clearly higher κ_2 region than the solid line with $C_2 = 1$ and is well fitted by the Eq. (3.18) with $C_2 \approx 0.7$ as shown by the dotted line for all three cases. This suggests that the numerical observation can not be explained without the C_2 smaller than unity. The tune shift factor of the 2nd mode evaluated with these results is $C_2 = 0.78 \pm 0.05$ for the Gaussian beam, $C_2 = 0.71 \pm 0.04$ for the waterbag beam, and $C_2 = 0.73 \pm 0.05$ for the parabolic beam.

The dash-dotted line in Fig. 3.25 (a) indicates the boundary of the stopband based on the incoherent picture, on which the following equation is satisfied

$$m\nu_0 = \frac{\kappa_m}{\eta^2} \, . \tag{3.19}$$

This can be derived from Eq. (2.13). As is obvious from this panel, the incoherent picture tends to overestimate the width of the stopband.

The results of similar WARP simulations are shown in Figs. 3.26 and 3.27, where 3rd-order and 4th-order nonlinear fields are added respectively. The positions of stop bands are well fitted by Eq. (3.18). Then, it is confirmed that the proper tune shift factors become significantly smaller than unity for all cases. As in the case of Fig. 3.25, we can not detect indications of incoherent resonance in Figs. 3.26 and 3.27.

The fitting results of 2nd, 3rd, and 4th non-coupling coherent resonances are summarized in Table 3.3. Since the single-peaked band profiles can be seen in all cases, we only need a single value of the tune shift factor to be assigned for each mode of a specific order from a practical point of view. The tune shift factor tends to be greater as the mode number gets higher for waterbag and parabolic beams as predicted by the theoretical studies [8, 20]. In

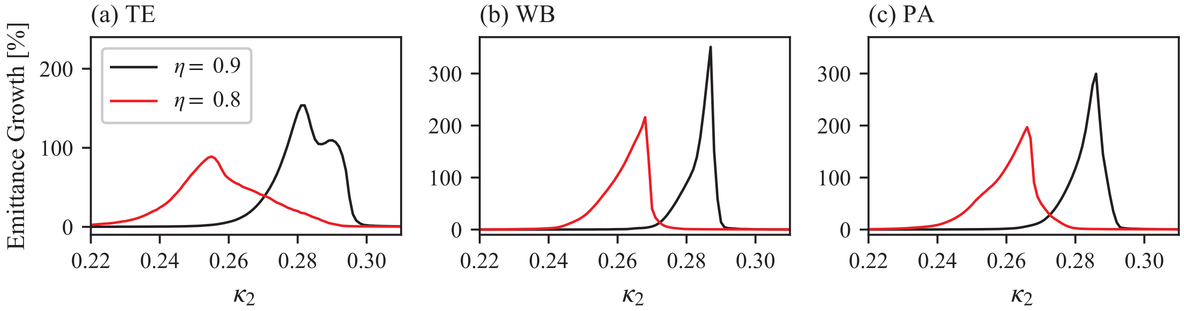

Figure 3.23: κ_2 dependence of the emittance growth evaluated at the exit of 200th cell. The operating point is set at $(\nu_{0x}, \nu_{0y}) = (0.15, 0.15)$. The tune depressions are initially adjusted at $\eta_{x(y)} = 0.8$ (red) and 0.9 (black). The external 2nd-order perturbation is applied to excite the 2nd mode. Three different types of initial distributions are considered: (a) Gaussian, (b) waterbag, and (c) parabolic.

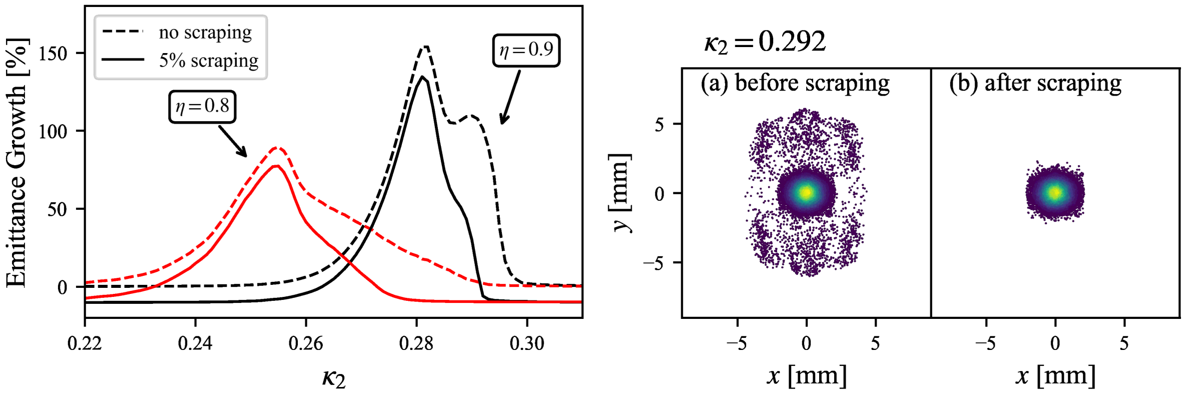

Figure 3.24: κ_2 dependence of the emittance growth evaluated at the exit of 200th cell. The dashed lines are the same as those in Fig. 3.23 (a). The solid lines indicate the stopband configurations after 5% of halo particle scraping based on the E-value defined by Eq. (3.10).

particular, the estimated tune shift factors for the waterbag beam are in good agreement with the theoretical value derived from Sachere's 1D Vlasov analysis assuming the uniform distribution ($C_2 = 0.75$, $C_3 = 0.88$, and $C_4 = 0.92$). On the other hand, the evaluated tune shift factors of the Gaussian beam get smaller as the m number increases. The main cause of this m dependence of C_m opposite to the others must be the incoherent resonance in the remaining tail region. The tail resonance expands the stopband toward the single-particle resonance line, making the evaluated tune shift factor smaller. The truncation of more tail particles may lead to more mitigation of this effect. However, too much scraping is not preferable due to the enhancement of a mismatch since the initial particle distribution generator equipped with the WARP code is designed assuming a full Gaussian distribution function.

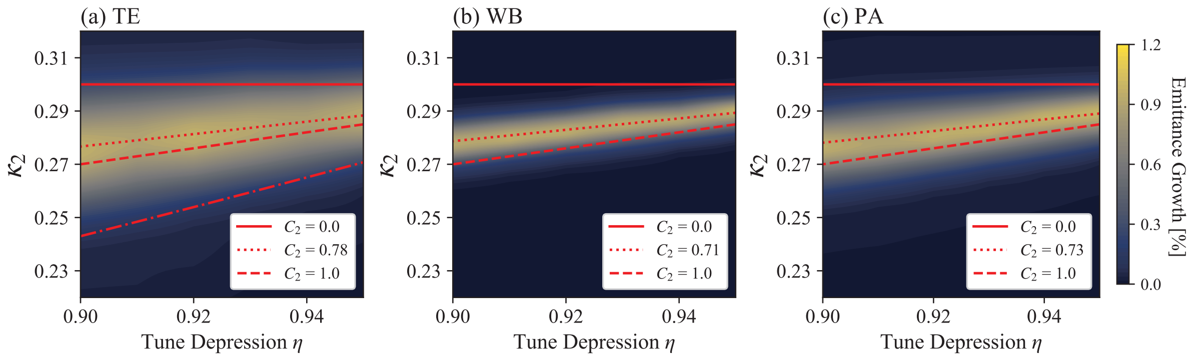

Figure 3.25: Emittance-growth chart obtained from 2D WARP simulations with the 2nd-order perturbation on. Three different types of initial particle distributions are considered: (a) Gaussian, (b) waterbag, and (c) parabolic. The operating point is set at $(\nu_{0x}, \nu_{0y}) = (0.15, 0.15)$. The solid and dashed lines correspond to the theoretical prediction from Eq. (3.1) with $C_2 = 0$ and 1. The dotted line is the location of the stopband peak fitted by Eq. (3.1) with (a) $C_2 = 0.78$, (b) 0.71, and (c) 0.73. The dash-dotted line in panel (a) is corresponding to the limit of the resonant region predicted based on the incoherent picture with Eq. (2.13).

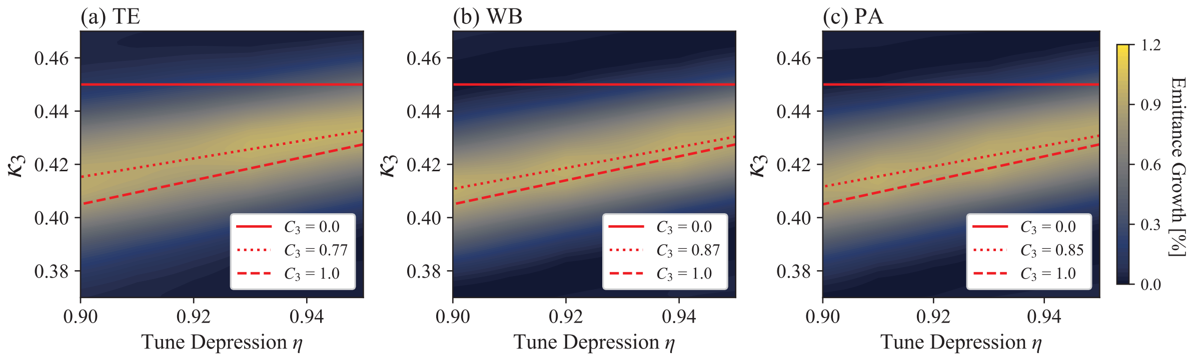

Figure 3.26: Emittance-growth chart obtained from 2D WARP simulations with the 3rd-order perturbation on. Except for the order of the perturbation, the other conditions are the same as employed in the case of Fig. 3.25.

3.5.4 Coupling resonance

According to the coherent resonance condition in Eq. (3.16), the external field that is proportional to $x^k y^\ell$ exites sum or difference resonances under the condition,

$$k\nu_{0x} + \ell\nu_{0y} = \frac{\kappa_m}{1 - (1 - \eta)C_m}, \tag{3.20}$$

where the horizontal and vertical tune depressions are set equal for simplicity. If $\nu_{0x} = \nu_{0y}$ and both of k and ℓ are positive numbers, the resonance condition in Eq. (3.20) is identical to Eq. (3.18). The fact that the simulation results of the last subsection show single-peaked band profiles in all cases supports our assumption that the tune shift factor depends only on the resonance order.

The C_m estimation is conducted by locating the stopband on η-κ_m plane as well as the last subsection, however, the case of coupling resonance is comparably troublesome. First of all,

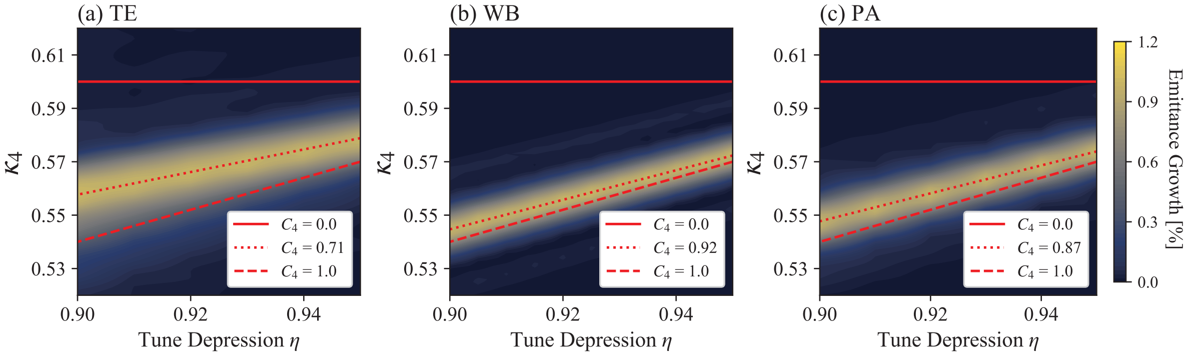

Figure 3.27: Emittance-growth chart obtained from 2D W$_{\text{ARP}}$ simulations with the 4th-order perturbation on. Except for the order of the perturbation, the other conditions are the same as employed in the case of Fig. 3.25.

Table 3.3: Tune shift factors estimated from non-coupling resonance bands excited by nonlinear fields

	C_2	C_3	C_4
TE	0.78 ± 0.05	0.77 ± 0.06	0.71 ± 0.06
WB	0.71 ± 0.04	0.87 ± 0.03	0.92 ± 0.01
PA	0.73 ± 0.05	0.85 ± 0.04	0.87 ± 0.02

the emittance growth is very sensitive to the initial emittances, and even the disappearance of the different resonance occurs under certain conditions as discussed in the last subsection. In addition, the difference resonance causes the emittance exchange between the horizontal and vertical degree of freedom and makes the stopband position ambiguous. In this subsection, we thus focus on sum-resonance to avoid such unwanted effects.

The operating point is set at $(\nu_{0x}, \nu_{0y}) = (0.142, 0.211)$, after careful test simulations. There are several reasons we decide to choose this operating point. First, this is within a region free from self-field-driven resonances of the orders lower than 4th. It is necessary to avoid self-field-driven resonances so that we observe the emittance growth that comes solely from the external field-driven resonance. We also have to take care of the other external-field resonances accompanied by the sum resonance of interest. For example, the 4th-order nonlinear field proportional to $x^3y - xy^3$ can drive the sum and difference resonances with $(k, \ell) = (3, 1)$, $(3, -1)$, $(1, 3)$, and $(-1, 3)$ at the same time, and the overlapping of the resonances with different conditions can be a serious error in the estimation of the tune shift factors.

The emittance growth due to the 2nd-order coupling resonance with $(k, \ell) = (1, 1)$ is color-coded in Fig. 3.28 on η-κ_2 plane, when the 2nd-order skew perturbation proportional to xy is switched on. Since ν_{0x}, ν_{0y}, k, and ℓ are known, we can evaluate the C_2 by fitting Eq. (3.20) to the position of the stopband. The evaluated tune shift factor is $C_2 = 0.71 \pm 0.05$ for the Gaussian beam, $C_2 = 0.72 \pm 0.05$ for the waterbag beam, and $C_2 = 0.71 \pm 0.05$ for the parabolic beam. Thus, we found that the estimated values of C_2 are almost identical for the three distribution functions.

The 3rd-order nonlinear field proportional to $3x^2y - y^3$ was switched on to drive the coupling resonance with $(k, \ell) = (2, 1)$ in Fig. 3.29. Because the 3rd-order resonant instability is much

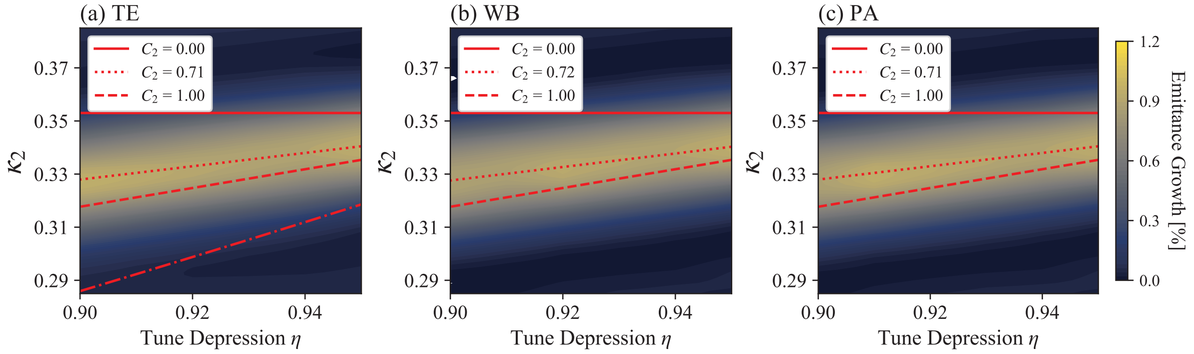

Figure 3.28: Emittance-growth chart of the sum resonance with $(k, \ell) = (1, 1)$ driven by the 2nd-order perturbation proportional to xy obtained from 2D WARP simulations. Three different types of initial particle distributions are considered: (a) Gaussian, (b) waterbag, and (c) parabolic. The operating point is set at $(\nu_{0x}, \nu_{0y}) = (0.142, 0.211)$. The solid and dashed lines correspond to the theoretical prediction from Eq. (3.1) with $C_2 = 0$ and 1. The dotted line is the location of the stopband peak fitted by Eq. (3.1) with (a) $C_2 = 0.71$, (b) 0.72, and (c) 0.71. The dash-dotted line in panel (a) is corresponding to the limit of the resonant region predicted based on the incoherent picture with Eq. (2.13).

weaker than the second's, the amplitude of the 3rd-order perturbation is set large compared with the case in Fig. 3.28 (b_3/b_2 in Eq. (1.12) is 1/4 when r_0 is set at 5 mm). The fitting Eq. 3.20 to these results leads to $C_3 = 0.72 \pm 0.08$ for the Gaussian beam, $C_3 = 0.82 \pm 0.03$ for the waterbag beam, and $C_3 = 0.80 \pm 0.05$ for the parabolic beam.

The 4th-order resonant instability is even much weaker than the other two cases. In order to observe the 4th-order stopband clearly, we have to further raise the amplitude of the perturbation ($\propto x^3y - xy^3$). On the other hand, the comparably strong nonlinearity may lead to the development of the tail resonance. The fitting procedure based on the Eq. (3.20) with $k = 1$ and $\ell = 3$ results in $C_4 = 0.63 \pm 0.03$ for the Gaussian beam, $C_4 = 0.84 \pm 0.01$ for the waterbag beam, and $C_4 = 0.79 \pm 0.01$. Then, we found the evaluated C_4 for the Gaussian beam is significantly smaller than the others. The much wider stopband shown in Fig. 3.30 (a) implies that the tail resonance has a non-negligible effect on the emittance growth. A similar tendency has been seen also in the case of Fig. 3.29 (a). Thus, it is difficult to make a reasonable estimate for the Gaussian beam since the effect of the tail resonance reduces the evaluated C_m from its real value, even though one percent of the outermost particle is truncated at injection.

Table 3.4: Tune shift factors estimated from sum resonance bands excited by nonlinear fields

	C_2	C_3	C_4
TE	0.71 ± 0.05	0.72 ± 0.08	0.63 ± 0.03
WB	0.72 ± 0.05	0.82 ± 0.03	0.84 ± 0.01
PA	0.71 ± 0.05	0.80 ± 0.05	0.79 ± 0.01

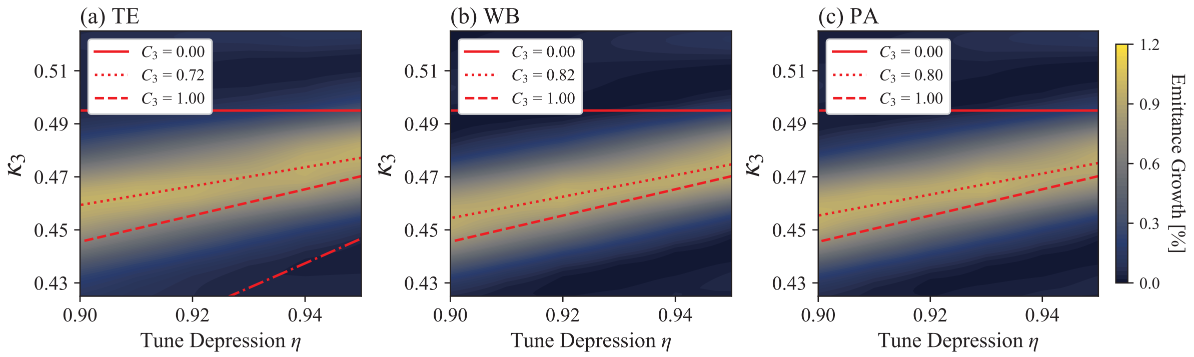

Figure 3.29: Emittance-growth chart of the sum resonance with $(k, \ell) = (2, 1)$ driven by the 3rd-order perturbation proportional to $3x^2y - y^3$ obtained from 2D WARP simulations. Except for the order of the perturbation, the other conditions are the same as employed in the case of Fig. 3.28.

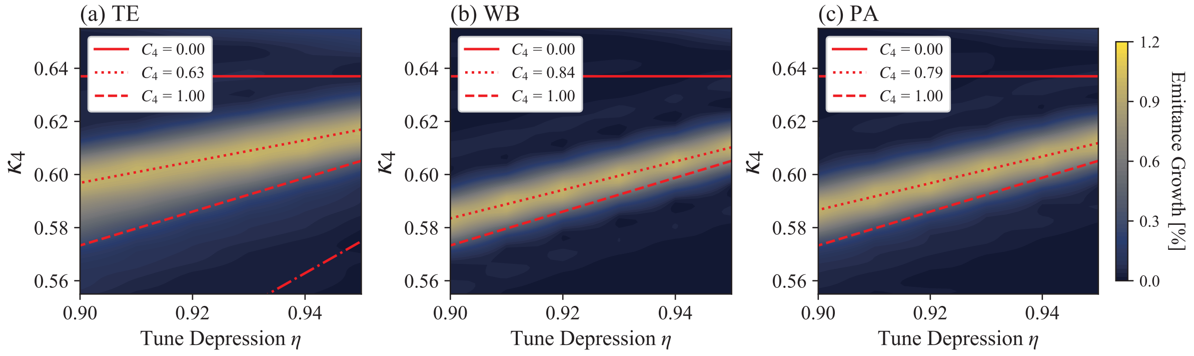

Figure 3.30: Emittance-growth chart of the sum resonance with $(k, \ell) = (3, 1)$ driven by the 4th-order perturbation proportional to $x^3y - xy^3$ obtained from 2D WARP simulations. Except for the order of the perturbation, the other conditions are the same as employed in the case of Fig. 3.28.

3.6 Construction of a stability tune diagram

We here consider the determination of the operating point (ν_{0x}, ν_{0y}) based on the coherent resonance condition in Eq. (3.1), whose validity has already been confirmed in previous sections. In order to provide a simple and useful guideline to choose the operating betatron tunes, we constructed a stability tune diagram that shows the resonance-free regions on ν_{0x}-ν_{0y} plane. In the stability tune diagram, we pay attention to the following three types of resonant instabilities of practical importance.

1 Self-field-driven coherent resonances: The space change force can be a source of various nonlinear resonances without external nonlinearity as shown in Figs. 3.15, 3.17, and 3.19. It is clear that we have to pay attention to these instabilities.

2 Tail resonances: The tail particles' motions are unstable rather individually than collectively under certain conditions that roughly correspond to the narrow region surrounded by coherent resonance stopbands and the single particle resonance lines on ν_{0x}-ν_{0y} plane. Considering that the beams more or less have a tail around the core, in reality, the tail

resonance region must be an essential component for our stability tune diagram.

3 External-field-drive resonances: In almost all of the circular accelerators, the sextupole magnets are equipped for chromaticity correction and generate much stronger nonlinear forces than the error field originating from misalignments. Since the resonances driven by this intended nonlinearity can be comparably severe, furthermore attention should be paid to these instabilities.

Then the effect of the error field-driven resonances is automatically covered by taking the coherent resonances into account.

Here, a question arises as to what orders of resonances should be noted. It is clear that we should pay attention to rather lower-order resonances than higher orders' since the higher-order modes are weak and tend to be suppressed by the Landau damping mechanism except for the resonances driven by a strong external nonlinear field. According to the ion trap experiments, the non-coupling coherent resonances of up to 3rd-order are always detectable [32]. Similarly, 2nd and 3rd-order resonance can be clearly seen in numerical simulations of Figs. 3.15, 3.17, and 3.19, and thus we should always take care of the coherent resonances of up to 3rd-order. On the other hand, whether we have to care of the next order ($m = 4$) resonance or not may depend on several configurations such as the beam density, accumulation time, and acceptable emittance of the accelerator. If an allowable emittance growth is strictly limited, or if the beam accumulated for a very long time, we need to take care of the 4th-order resonances.

It is very difficult to theoretically evaluate a bandwidth of coherent resonances. They expected to depend on not only the beam intensity and operating points but also density profiles as shown in Subsection 3.5.1. Thus, we have to rely on time-consuming numerical simulations to obtain precise bandwidth. On the other hand, our purpose is to provide a simple and useful guideline as a starting point for the determination of the operating point, and thus we here rely on a simple criterion given by

$$\Delta w_m = 2(1 - C_m)\frac{1 - \bar{\eta}}{\bar{\eta}}\bar{\nu}_0 f_{k\ell}\ . \tag{3.21}$$

This is a generalization of Eq. (2.17) derived from the 1D Vlasov theory. $\bar{\nu}_0 \equiv (\nu_{0x} + \nu_{0y})/2$ and $\bar{\eta} \equiv (\eta_x + \eta_y)/2$ denote the averaged values in the horizontal and vertical directions. The factor $f_{k\ell}$ is defined as

$$f_{k\ell} = \frac{|\ell\varepsilon_x + k\varepsilon_y|}{|\ell|\varepsilon_x + |k|\varepsilon_y}\ . \tag{3.22}$$

This is introduced to reflect the disappearance of difference resonances as discussed in Sec. 3.5. The difference resonance disappears when the condition $I_{k\ell} = 0$ is fulfilled, and then $f_{k\ell}$ also becomes zero. Thus, the stopbands with $I_{k\ell} = 0$ will be drawn with no bandwidth in our stability tune diagram.

3.6.1 Application of a stability tune diagram to the RCS at J-PARC

As an example, we assume the current configurations of the rapid cycling synchrotron (RCS) at Japan Proton Accelerator Research Complex (J-PARC) [49]. The basic parameters of RCS are shown in Table 3.5 [50]. The super-period $N_{\rm sp}$ denotes the number of groups of cells. The

Table 3.5: Fundamental parameters of the RCS at J-PARC [49,51].

Circumference	348.333 [m]
Number of cells	27
Super-period ($N_{\rm sp}$)	3
Operating point (ν_{0x}, ν_{0y})	$(6.45, 6.42)$
Injection energy	400 [MeV]
Extraction energy energy	3 [GeV]
Transverse rms emittance (at injection)	50 [mm·mrad]
Bunch length	92 [m]
Number of bunches	2
Particle per pulse	8.3×10^{13}

RCS has a triangle-like shape and consists of three large structures that include 9 cells. If we expand the betatron function into Fourier series around the ring, $N_{\rm sp}$ harmonics then appear. Thus the right-hand side of Eq. (3.1) have to be replaced by $N_{\rm sp}n/2$, and the coherent resonance condition is given by

$$k(\nu_{0x} - C_m \Delta\bar{\nu}_x) + \ell(\nu_{0y} - C_m \Delta\bar{\nu}_y) = \frac{nN_{\rm sp}}{2}, \tag{3.23}$$

where the ν_{0x} and ν_{0y} represent the bare tunes per one revolution of the RCS. According to the parameters shown in Table 3.5, the rms tune depression is evaluated to be 0.98 at injection.

Figure 3.31 shows the stability tune diagram assuming the RCS. The stopband with $(k, \ell, n) = (1, -1, 0)$ has no width since $\varepsilon_x \approx \varepsilon_y$ in the RCS. We here take the coherent tune shift factors as $C_2 = 0.7$, $C_3 = 0.8$, and $C_4 = 0.9$ based on the numerical evaluation in the last section. If we adopt the theoretical values of $C_2 = 0.75$, $C_3 = 0.88$, and $C_4 = 0.92$ proposed by Sachere [8], the stopband features in the figures are hardly affected. The bands shown in black correspond to the resonant instabilities driven by the quadrupole field and 3rd-order nonlinear field originating from the sextupole magnets equipped with the RCS. We can construct such stability tune diagrams only with the basic parameters shown in the table and the lattice design including the alignment of the nonlinear magnets, which are known in any machine.

The operating point was chosen around the $(\nu_{0x}, \nu_{0y}) = (6.68, 6.27)$ (green dot) at the design stage and had been already changed due to the resonant instabilities. After a careful tune survey, the current operating point has been chosen at around $(\nu_{0x}, \nu_{0y}) = (6.45, 6.42)$ (red dot). Figure 3.31 shows that the red dot is located at the resonance-free region contrary to the green dot. Thus, it is confirmed that the prediction in Fig. 3.31 is consistent with the result of experimental optimization of the operating point in the RCS.

Next, we add the 4th-order stopbands to the stability diagram as shown in Fig. 3.32. Then the current operating point was found to be overlapped with the 4th-order stopbands corresponding to $(k, \ell, n) = (4, 0, 51)$, $(0, 4, 51)$, $(3, 1, 51)$, $(1, 3, 51)$, and $(2, 2, 51)$. Thus, the RCS performance might be improved by choosing the operating point around at $(\nu_{0x}, \nu_{0y}) = (6.29, 6.32)$ and $(6.71, 6.68)$ denoted with blue dots. Then the $(\nu_{0x}, \nu_{0y}) = (6.29, 6.32)$ is should be preferable than $(6.32, 6.29)$ since the instability of external field driven resonance corresponding to $(k, \ell, n) = (2, 1, 36)$ expected to be more severe than self-field-driven one corresponding to $(k, \ell, n) = (1, 2, 36)$.

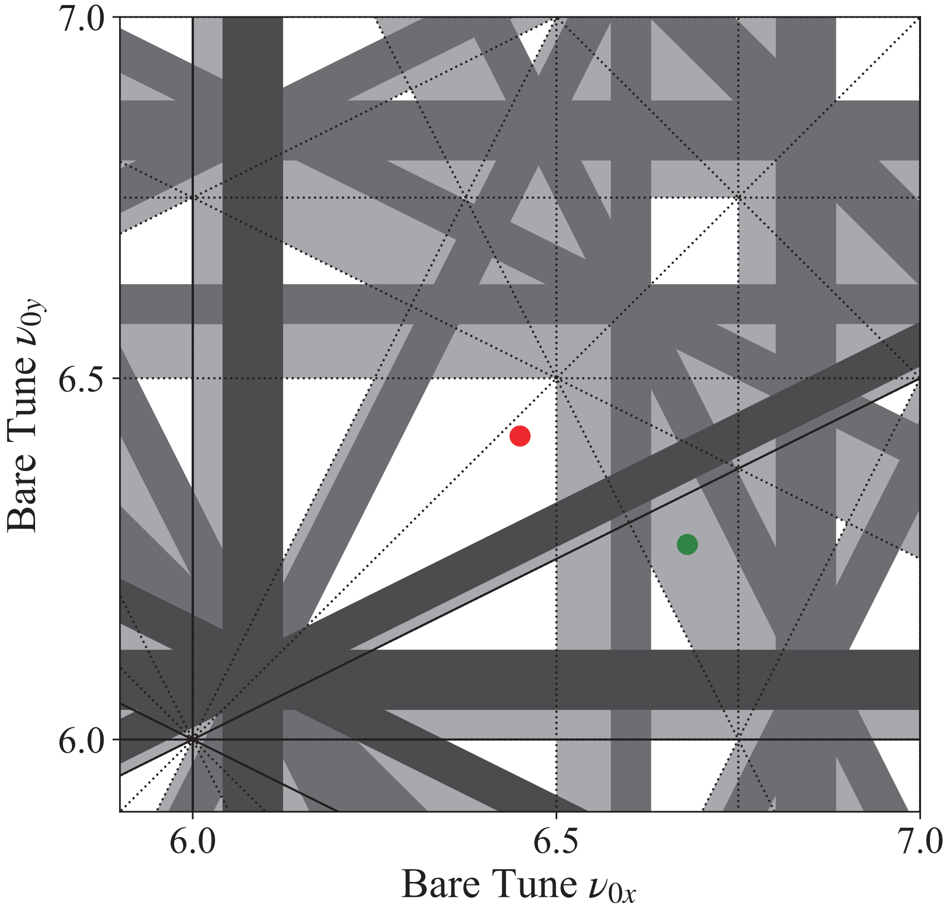

Figure 3.31: Stability tune diagram obtained from Eqs. (3.21) and (3.23). The fundamental parameters of the RCS at J-PARC given in Table 3.5 are assumed. The stopbands of self-field-driven, external-field-driven, and tail resonances are drawn in the diagram. The possible resonant instabilities of up to 3rd-order are considered. The tune shifts factors determined in Sec. 3.5: $C_2 = 0.7$ and $C_2 = 0.8$ is used here. The tune depression is fixed at $\eta_{x(y)} = 0.98$ that is approximately corresponding to the configuration of the RCS. The red dot represents the typical operating point $(\nu_{0x}, \nu_{0y}) = (6.45, 6.42)$ of the RCS [51].

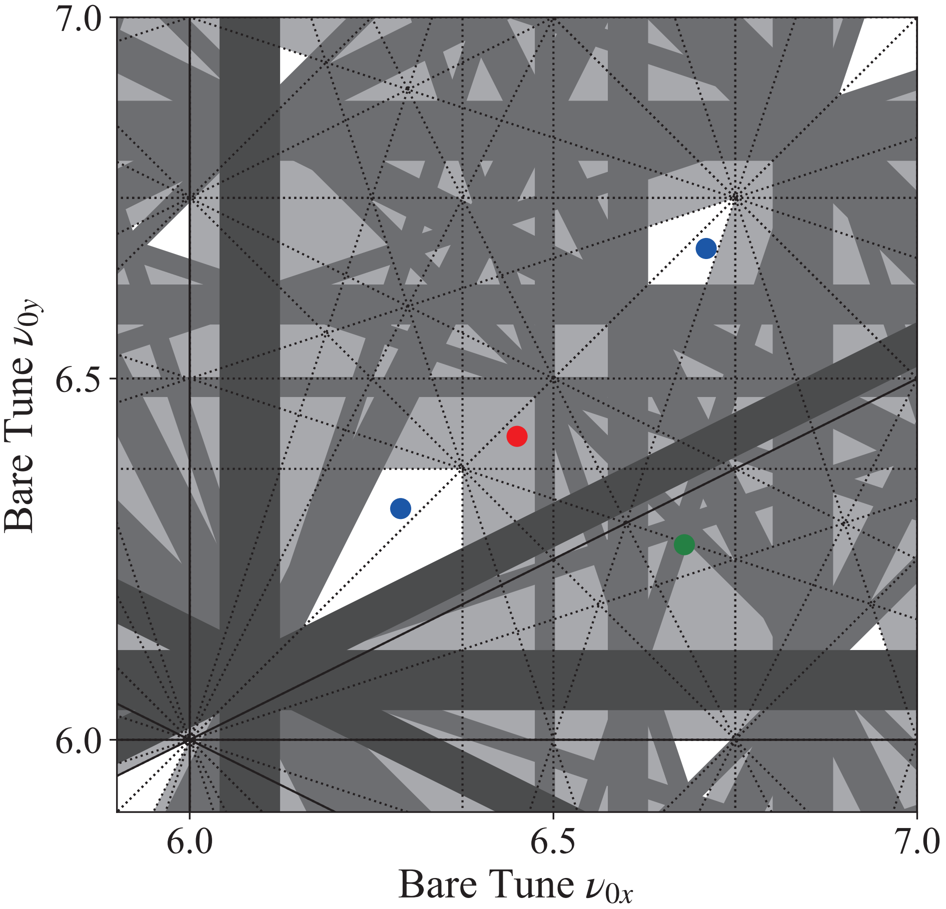

Figure 3.32: Stability tune diagram obtained from Eqs. (3.21) and (3.23). The possible resonant instabilities of up to 4th-order are considered. The tune shifts factors determined in Sec. 3.5: $C_2 = 0.7$, $C_3 = 0.8$, and $C_4 = 0.9$ are used here. The other conditions are the same as employed in the case of Fig. 3.31.

3.7 Summary

We have conducted systematic self-consistent simulations to study the 2D betatron resonances induced by space-change force in high-intensity circular accelerators. The simulation results suggest that two different types of instability mechanisms exist; namely the incoherent resonances in the beam tail region and collective coherent resonances in the beam core. It is confirmed that the proposed 2D coherent resonance condition well explains the basic features of the collective coherent resonances despite its remarkable simplicity. The factor 1/2 on the right-hand side of Eq. (3.1) implies that many instability bands of low-order resonances can be disregarded in previous studies at high beam density. In addition, no clear signature of the occurrence of incoherent resonances in the dense beam core has been observed contrary to the conventional incoherent concepts.

It is also confirmed that the tune shift factors of low-order resonances are always smaller than unity as predicted by the 1D Vlasov analysis. Moreover, the tune shift factor is found to depend almost exclusively on the resonance order m. This suggests that we can predict the locations of important stopbands with the several tune shift factors of each order over the whole tune space unless the beam density does not exceed the achievable range in circular accelerators.

We have proposed a stability tune diagram based on the coherent resonance concept. The simple rule shown in Sec. 3.6 allows us to quickly spot the resonance-free region that is preferable to set operating points, without the experimentally unobservable parameters or considerable efforts. The predictions of our diagram have been confirmed to be consistent with the operating configuration of the RCS in J-PARC, which guarantees the reliability of the diagram. It seems possible to provide a valuable guideline for any circular accelerators as long as the basic lattice information including the distribution of nonlinear magnets is given.

Chapter 4

Resonance in linear accelerators

4.1 Introduction

In ion linear accelerators (linac), the beam stability can be seriously deteriorated by space-charge-driven resonances. Even if the external field is completely linear, the nonlinear space charge potential can be a source of various resonances [12, 20, 22, 52, 53]. Unlike in the case of circular accelerators, the bunch length in linac is comparable to the transverse beam size. Since the synchrotron and betatron tunes are also comparable, the cooperation between the longitudinal and transverse degrees of freedom is expected to be more pronounced. Thus we should pay attention to not only betatron resonances but also synchrobetatron coupling resonances. In addition, any ion linac does not have a strictly periodic structure due to the increase in the beam's kinetic energy. The betatron and synchrotron phase advances are not necessarily constants but rather shift gradually. Then the operating point may cross low-order resonance stopbands. The resonance crossing may lead to emittance growth and beam loss.

In order to study the resonance features in the linac systematically, we developed a simulation model and performed self-consistent multi-particle simulations using the "IMPACT" code [55, 56]. Assuming the most typical drift-tube linac structure (DTL), we explore the low-order resonant instability over a wide parameter range. In this chapter, we first derive the Hamiltonian for charged particle beam propagating through a DTL. After presenting our simulation model in detail, Sec. 4.6 is devoted to showing the simulation results with similar design parameters of J-PARC DTL. It is then confirmed that serious emittance exchanges occur when the operating point crosses the synchrobetatron difference resonance band. We also demonstrate that the difference resonances can be significantly suppressed by choosing a certain ratio of the initial transverse and longitudinal emittances. The equipartitioned linac design is found to automatically achieve the proper emittance ratio and broaden the usable operating area in the tune space.

4.2 Hamiltonian formalism for drift-tube linacs

In this section, we follow the work of H. Okamoto *et al.* and derive the Hamiltonian of an ion beam propagating through an Alvarez-type linac [57]. We assume the axisymmetric TM mode ($B_z = 0$) generated by an accelerating structure of period $L = \beta_s \lambda$ where β_s and λ are Lorentz factor of synchronous particle and RF wavelength. Maxwell's equation in cylindrical coordinates can be written as

$$\begin{cases} \dfrac{1}{r}\dfrac{\partial(rE_r)}{\partial r}+\dfrac{\partial E_z}{\partial z}=0\ , \\ \dfrac{\partial E_r}{\partial z}-\dfrac{\partial E_z}{\partial r}=-\dfrac{\partial B_\theta}{\partial t}\ , \\ -\dfrac{\partial(B_\theta)}{\partial z}=\dfrac{1}{c^2}\dfrac{\partial E_r}{\partial t}\ , \\ \dfrac{1}{r}\dfrac{\partial(rB_\theta)}{\partial r}=\dfrac{1}{c^2}\dfrac{\partial E_z}{\partial t}\ , \end{cases} \tag{4.1}$$

where t denotes time. E_w and B_w denote the electric and magnetic field components in the w direction respectively. E_θ and B_r are zero. Combining the above equations yields

$$\frac{1}{r}\frac{\partial}{\partial r}\left(r\frac{\partial E_z}{\partial r}\right)+\frac{\partial^2 E_z}{\partial z^2}=\frac{1}{c^2}\frac{\partial^2 E_z}{\partial t^2}\ . \tag{4.2}$$

We here focus only on the RF components that have the angular frequency of ω. Assuming that E_z can be written as $E_z = R(r)Z(z)\cos\omega t$, $R(r)$ and $Z(z)$ satisfy that

$$\begin{cases} \dfrac{1}{rR}\dfrac{d}{dr}\left(r\dfrac{dR}{dr}\right)+\dfrac{\omega^2}{c^2}=\left(\dfrac{2n\pi}{L}\right)^2\ , \\ \dfrac{1}{Z}\dfrac{d^2Z}{dz^2}=-\left(\dfrac{2n\pi}{L}\right)^2\ , \end{cases} \tag{4.3}$$

where n is necessarily an integer because $Z(z)$ must be periodic function, and $Z(z)$ is given by the linear combination of $\cos(2n\pi z/L)$ and $\sin(2n\pi z/L)$. The differential equation for $R(r)$ is found to be identical to modified Bessel's equation, and $R(r)$ can be given by modified Bessel functions. Thus we can obtain the Electromagnetic fields

$$\begin{cases} E_z=\displaystyle\sum_{n=0}^{\infty}a_nI_0(k_nr)\cos\frac{2n\pi z}{L}\cos\omega t\ , \\ E_r=\displaystyle\sum_{n=0}^{\infty}\frac{2n\pi a_n}{k_nL}I_1(k_nr)\sin\frac{2n\pi z}{L}\cos\omega t\ , \\ B_\theta=-\displaystyle\sum_{n=0}^{\infty}\frac{\omega a_n}{k_nc^2}I_1(k_nr)\cos\frac{2n\pi z}{L}\sin\omega t\ , \end{cases} \tag{4.4}$$

where I_n denotes the modified bessel function of order n. a_n is the nth Fourie coefficients determined by the boundary conditions, and $k_n^2 = (2\pi/\lambda)^2[(n\lambda/L)^2 - 1]$.

In order to determine a_n approximately, we here assume a boundary condition that E_z is uniform at the aperture radius within every accelerating gap of width g as shown in Fig. 4.1; namely $E_z(r = r_0, z, t = 0) = E_0L/g$ where E_0 is a constant. Then, we obtain

$$a_0=\frac{E_0}{I_0(k_0r_0)}\ ,\quad a_n=\frac{2E_0}{I_0(k_nr_0)}\cdot\frac{\sin(n\pi g/L)}{n\pi g/L}\quad \text{for}\quad n=1,2,3,\ldots.\ , \tag{4.5}$$

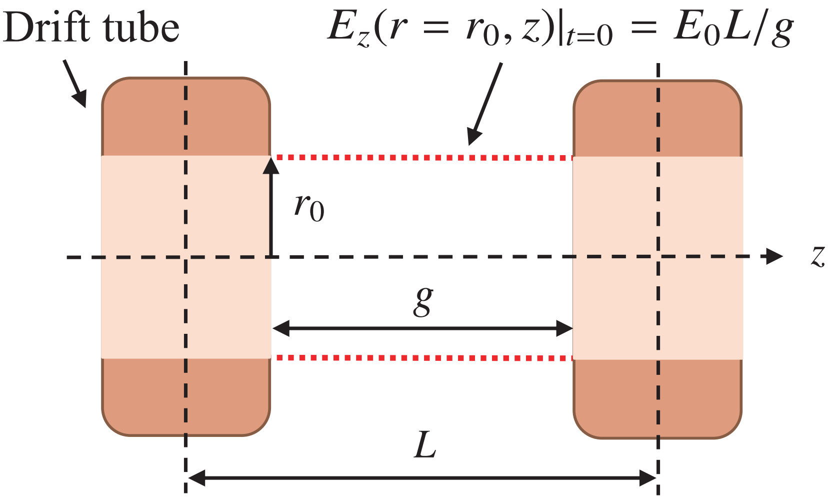

Figure 4.1: Schematic view of the accelerating gap. Neumann boundary condition is imposed on the red dotted line.

The traveling waves of $n \neq 1$ have different phase velocities to the synchronous particle, and their contributions are disappeared by averaging over one structure period [58, 59]. Only the traveling wave of $n = 1$ contributes to the beam acceleration, and we here ignore the other field components for simplicity except that our calculations in later sections take all of the field components into account. Then, the vector potential $\boldsymbol{A}^{(\mathrm{rf})} = (A_r^{(\mathrm{rf})}, A_\theta^{(\mathrm{rf})}, A_z^{(\mathrm{rf})})$ that derives the electromagnetic field in Eq. (4.4) is given by

$$\begin{cases} A_z^{(\mathrm{rf})} = \dfrac{E_0T}{\omega} I_0(k_1r) \sin\left(\dfrac{2\pi z}{L} - \omega t\right), \\ A_r^{(\mathrm{rf})} = -\dfrac{2\pi E_0T}{\omega k_1 L} I_1(k_1r) \cos\left(\dfrac{2\pi z}{L} - \omega t\right), \end{cases} \tag{4.6}$$

where T is referred to as the "transit time factor" characterizing the accelerating field distribution and given by

$$T = \frac{1}{I_0(k_1r_0)} \cdot \frac{\sin(\pi g/L)}{\pi g/L} \,. \tag{4.7}$$

The time dependence of the total energy of the synchronous particle W_s is approximately written as

$$\frac{dW_\mathrm{s}}{dz} \approx qE_0T\cos\psi_\mathrm{s} \,, \tag{4.8}$$

where ψ_s is the synchronous phase defined by

$$\psi_\mathrm{s} = \omega \int^z \frac{dz}{\beta_\mathrm{s}c} - \frac{2\pi z}{L} \,. \tag{4.9}$$

In this study, we assume that the ψ_s is a constant through a whole linac for simplicity.

From Eq. (1.5), the Hamiltonian in cylindrical coordinates can be written as

$$H_{\mathrm{DTL}}(r,\theta,t,p_r,p_\theta,p_t;z) = -\sqrt{p^2 - \left(p_r - qA_r^{(\mathrm{rf})}\right)^2 - \frac{p_\theta^2}{r^2}} - q\left(A_z^{(\mathrm{rf})} + A_z^{(\mathrm{mag})}\right) - \frac{q\beta_\mathrm{s}}{c}\phi_\mathrm{sc} \; , \tag{4.10}$$

where $p = \sqrt{(p_t + q\phi_\mathrm{sc})^2/c^2 - mc^2}$ is the kinetic momentum. After the Taylor expansion of the square root, substituting Eq. (4.6) into the Hamiltonian yields

$$\begin{aligned} H_{\mathrm{DTL}} \approx & -p + \frac{1}{2p_\mathrm{s}}\left[p_r + \frac{2\pi qE_0T}{\omega k_1 L}I_1(k_1 r)\cos\left(\frac{2\pi z}{L} - \omega t\right)\right]^2 + \frac{p_\theta^2}{2p_\mathrm{s}r^2} \\ & - \frac{qE_0T}{\omega}I_0(k_1 r)\sin\left(\frac{2\pi z}{L} - \omega t\right) + \frac{qG(z)r^2\cos 2\theta}{2} - \frac{q\beta_\mathrm{s}}{c}\phi_\mathrm{sc} \; , \end{aligned} \tag{4.11}$$

where the kinetic momentum for the synchronous particle is given by $p_\mathrm{s} = \sqrt{(W_\mathrm{s}/c)^2 - mc^2}$. We have assumed that the transverse momenta are much lesser than p and neglect the higher order terms. $G(z)$ represents the quadrupole gradient along the beam line. We now consider the canonical transformation from (t, W) to the relative time and energy $(\Delta t, -\Delta W)$ with a generating function

$$F_1(t, -\Delta W; z) = -(\Delta W + W_\mathrm{s})\left(t - \int^z \frac{dz}{\beta_\mathrm{s} c}\right) . \tag{4.12}$$

The new Hamiltonian is

$$\begin{aligned} H_{\mathrm{DTL}} \approx & \frac{(\Delta W)^2}{2p_\mathrm{s}(\beta_\mathrm{s}\gamma_\mathrm{s}c)^2} + \frac{1}{2p_\mathrm{s}}\left[p_r + \frac{2\pi qE_0T}{\omega k_1 L}I_1(k_1 r)\cos\left(\omega\Delta t + \psi_\mathrm{s}\right)\right]^2 + \frac{p_\theta^2}{2p_\mathrm{s}r^2} \\ & + \frac{qE_0T}{\omega}[I_0(k_1 r)\sin\left(\omega\Delta t + \psi_\mathrm{s}\right) - \omega\Delta t\cos\psi_\mathrm{s}] + \frac{qG(z)r^2\cos 2\theta}{2} + \frac{q}{\beta_\mathrm{s}\gamma_\mathrm{s}^2 c}\phi_\mathrm{sc} \; . \end{aligned} \tag{4.13}$$

Assuming that the particle amplitude in the bunch is sufficiently small; namely, $k_1 r \ll 1$ and $w\Delta t/2\pi \ll 1$, we can approximately write

$$\begin{aligned} \sin\left(\omega\Delta t + \psi_\mathrm{s}\right) &\approx \omega\Delta t\cos\psi_\mathrm{s} + \sin\psi_\mathrm{s}[1 - (\omega\Delta t)^2/2] \; , \\ \cos\left(\omega\Delta t + \psi_\mathrm{s}\right) &\approx \cos\psi_\mathrm{s} - \omega\Delta t\sin\psi_\mathrm{s} \; , \\ I_0(k_1 r) &\approx 1 + (k_1 r)^2/4 \; , \\ I_1(k_1 r) &\approx k_1 r/2 \; . \end{aligned} \tag{4.14}$$

Note that the 3rd-order nonlinear term proportional to $\Delta t r^2$ is inevitably present in the product of $I_0(k_1 r)$ and $\sin\left(\omega\Delta t + \psi_\mathrm{s}\right)$. This nonlinear term can be a source of 3rd-order different resonance, and this aspect will be discussed later in this chapter. Substituting Eq. (4.14) into the Hamiltonian in Eq. (4.13) and keeping low-order terms, we obtain the linearized Hamiltonian

$$\begin{aligned} H_{\mathrm{DTL}} \approx & \frac{(\Delta W)^2}{2p_\mathrm{s}(\beta_\mathrm{s}\gamma_\mathrm{s}c)^2} + \frac{1}{2p_\mathrm{s}}\left(p_r + \frac{\pi qE_0T}{\omega L}r\cos\psi_\mathrm{s}\right)^2 + \frac{p_\theta^2}{2p_\mathrm{s}r^2} \\ & - \frac{qE_0T\omega\sin\psi_\mathrm{s}}{2}(\Delta t)^2 + \frac{qE_0T\sin\psi_\mathrm{s}}{4\omega}(k_1 r)^2 + \frac{qG(z)r^2\cos 2\theta}{2} + \frac{q}{\beta_\mathrm{s}\gamma_\mathrm{s}^2 c}\phi_\mathrm{sc} \; . \end{aligned} \tag{4.15}$$

Now we would like to perform a canonical transformation to remove the cross term proportional to rp_r in the 2nd term on the right-hand side. This transformation is achieved with the generating function

$$F_2(r,\hat{p}_r;z) = r\hat{p}_r - \frac{\pi q E_0 T}{2\omega L} r^2 \cos\psi_\mathrm{s}\ , \tag{4.16}$$

The new Hamiltonian is given by

$$\begin{aligned} H_\mathrm{DTL} \approx & \frac{(\Delta W)^2}{2p_\mathrm{s}(\beta_\mathrm{s}\gamma_\mathrm{s}c)^2} + \frac{1}{2p_\mathrm{s}}\left[\hat{p}_r^2 + \left(\frac{p_\theta}{r}\right)^2\right] + \frac{p_\mathrm{s}}{2}\left(\frac{\gamma_\mathrm{s}\sigma_\parallel}{2\pi}\right)^2(\omega\Delta t)^2 \\ & - \frac{p_\mathrm{s}\sigma_\parallel^2}{4}\left[1 - \left(\frac{\gamma_\mathrm{s}\sigma_\parallel}{2\pi}\cot\psi_\mathrm{s}\right)^2\right]\left(\frac{r}{L}\right)^2 + \frac{qG(z)r^2\cos 2\theta}{2} + \frac{q}{\beta_\mathrm{s}\gamma_\mathrm{s}^2 c}\phi_\mathrm{sc}\ , \end{aligned} \tag{4.17}$$

where $\sigma_\parallel^2 = -2\pi q\lambda E_0 T \sin\psi_\mathrm{s}/mc^2\beta_\mathrm{s}\gamma_\mathrm{s}^3$ represents the synchrotron phase advance. The 2nd term on the right-hand side suggests that the longitudinal focusing is inevitably accompanied by the defocusing force in the transverse direction. This effect is referred as to "RF-defocusing" and may enlarge the amplitude of the betatron oscillation when the synchrotron tune is high.

4.2.1 Root-mean-squared envelope equations for bunched beams

The rms envelope equations for bunched beams including acceleration can be given by [7, 60]:

$$\begin{cases} \dfrac{d^2X}{dz^2} + \left(\dfrac{1}{p_\mathrm{s}}\dfrac{dp_\mathrm{s}}{dz}\right)\dfrac{dX}{dz} + K_x(z)X - \dfrac{\Gamma u_\mathrm{s}\pi\lambda_3}{l^2}M_{311}(X,Y,u_\mathrm{s}T)X - \left(\dfrac{\delta}{p_\mathrm{s}}\right)^2\dfrac{\epsilon_x^2}{X^3} = 0, \\ \dfrac{d^2Y}{dz^2} + \left(\dfrac{1}{p_\mathrm{s}}\dfrac{dp_\mathrm{s}}{dz}\right)\dfrac{dY}{dz} + K_y(z)Y - \dfrac{\Gamma u_\mathrm{s}\pi\lambda_3}{l^2}M_{131}(X,Y,u_\mathrm{s}T)Y - \left(\dfrac{\delta}{p_\mathrm{s}}\right)^2\dfrac{\epsilon_y^2}{Y^3} = 0, \\ \dfrac{d^2T}{dz^2} + 3\left(\dfrac{1}{p_\mathrm{s}}\dfrac{dp_\mathrm{s}}{dz}\right)\dfrac{dT}{dz} + K_t(z)T - \dfrac{\Gamma u_\mathrm{s}\pi\lambda_3}{l^2}M_{113}(X,Y,u_\mathrm{s}T)T - \left(\dfrac{\delta}{p_\mathrm{s}u_\mathrm{s}^2}\right)^2\dfrac{\epsilon_\parallel^2}{T^3} = 0, \end{cases} \tag{4.18}$$

with

$$u_\mathrm{s} = \gamma_\mathrm{s}\beta_\mathrm{s}\ , \delta = mc\ , \Gamma = \frac{qI}{2\pi\epsilon_0 p_\mathrm{s}\beta_\mathrm{s}^2 c^2\gamma_\mathrm{s}^2}\ , \tag{4.19}$$

where Γ represents the generalized perviance, and I is the peak beam current. $\lambda_3 \approx 1/5\sqrt{5}$ is a factor depending weakly on the beam's density profile in the real space. The elliptic integral $M_{i,j,k}$ is given by

$$M_{i,j,k}(x,y,\tau) = \frac{3}{2}\int_0^\infty \frac{ds}{(x^2+s)^{i/2}(y^2+s)^{j/2}(\tau^2+s)^{k/2}}\ ,$$

X and Y are horizontal and verrtical rms beam size scaled with $l = c/\omega$ to be dimensionless. T is the longitudinal rms phase given by $T = \omega\sqrt{\langle\Delta t^2\rangle}$. K_x, K_y, and K_t represent linear focusing forces produced by the accelerating field and quadrupole magnets. ϵ_x, ϵ_y, and $\epsilon_\parallel$ are normalized

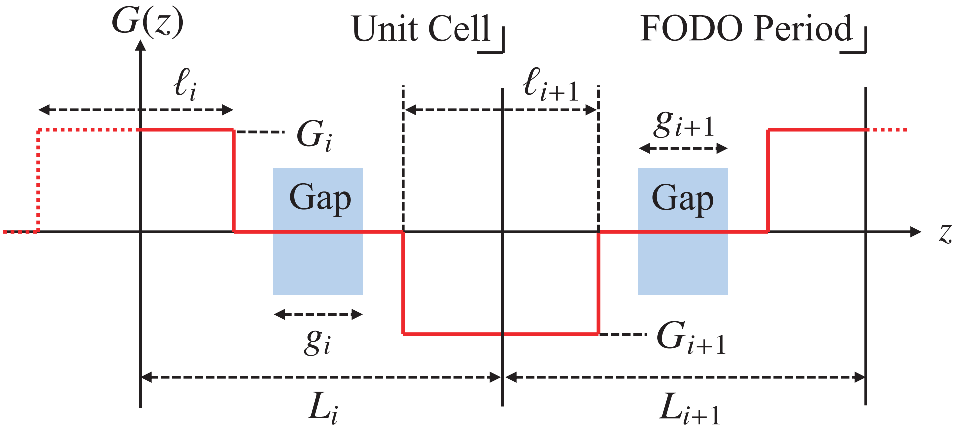

Figure 4.2: Schematic plot of a unit focusing cell.

rms emittances defined with unnormalized rms emittances as

$$\begin{aligned} \epsilon_x &= \varepsilon_x \beta_s \gamma_s \ , \\ \epsilon_y &= \varepsilon_y \beta_s \gamma_s \ , \\ \epsilon_\parallel &= \varepsilon_z \beta_s \gamma_s^3 \ . \end{aligned} \tag{4.20}$$

The rms phase advances in i and $(i+1)$th unti cells can be obtained by

$$\begin{aligned} \mu_{x,i}\eta_{x,i} &= \int_{z_i}^{z_{i+2}} \frac{\epsilon_x}{\beta_s\gamma_s l^2 X^2}\,dz, \\ \mu_{y,i}\eta_{y,i} &= \int_{z_i}^{z_{i+2}} \frac{\epsilon_y}{\beta_s\gamma_s l^2 Y^2}\,dz, \\ \sigma_i\eta_{\parallel,i} &= \int_{z_i}^{z_{i+2}} \frac{\epsilon_\parallel}{\beta_s^3\gamma_s^3 l^2 T^2}\,dz, \end{aligned} \tag{4.21}$$

where $\eta_{x,i}$, $\eta_{y,i}$, and $\eta_{\parallel,i}$ are rms tune depressions in i and $(i+1)$th unit cells. $\mu_{x,i}$, $\mu_{y,i}$, and σ_i denote the transverse and longitudinal zero current phase advances per one FODO period consist of i and $(i+1)$th unit cells. In our simulation model, the horizontal and vertical motions are assumed to be symmetric. Then the horizontal and vertical phase advances are approximately equal; namely $\mu_{x,i} \approx \mu_{y,i} (\equiv \mu_i)$ and $\eta_{x,i} \approx \eta_{y,i} (\equiv \eta_{\perp,i})$, when the equipartitioning condition is given by [13, 61]

$$\frac{\epsilon_\perp \mu_i \eta_{\perp,i}}{\epsilon_\parallel \sigma_i \eta_{\parallel,i}} = 1. \tag{4.22}$$

4.3 Simulation model

We assume an Alvarez-type DTL structure where the electromagnetic fields from quadrupole magnets and accelerating gaps exist along the design orbit. The transverse focusing is provided by the quadrupole magnetic field in the drift tubes. In the longitudinal direction, the beam is focused by the accelerating fields between the drift tubes. A schematic plot of this channel is shown in Fig. 4.2. The subscript i represents the serial number assigned to each unit structure and increases from 1. There are many design parameters to determine the electromagnetic field configuration such as the effective quadrupole length ℓ_i, quadrupole field gradient G_i, and gap width g_i. Thus we introduce a simulation model to give these design parameters [62].

4.3.1 Accelerating gap

Strictly speaking, the DTL structure is not periodic contrary to the assumption in Sec. 4.2. However, the variation in the unit length is so slow that the lengths of adjacent two units cells can be assumed to be approximately equal ($L_i \approx L_{i+1}$) until the accelerating gradient $E_0 T \cos\psi_\mathrm{s}$ is within a realistic range of the order of several megavolts per meter. Thus the electromagnetic field exists in ith accelerating gap can be well approximated by Eqs. (4.4) and (4.5) where L and g are replaced by L_i and g_i.

In this chapter, we keep the E_0 and T constants through a whole linac. The accelerating gradient becomes also constant. Then the gap width g_i should be chosen so that the a_1 in Eq. (4.5) is kept constant, and that can be numerically accomplished with ease. Thus the g_i becomes not constant but gradually gets longer as i increases in our simulations.

The summation in Eq. (4.4) has to be interrupted at the proper n number in numerical simulations. After some test simulations, we set the upper limit of $n(\equiv n_\mathrm{max})$ at 20. Fig. 4.3 shows examples of E_z for different n_max numbers. $Ez(r = r_0)$ converges to a square shape in the limit of $n \to \infty$ due to the boundary condition. The profiles of $E_z(r = r_0)$ appear to be quite different from each other. On the other hand, we can hardly see any difference between the three profiles of $E_z(r = 0)$ shown in Fig. 4.3 (b). It is also confirmed that there is no significant difference among the simulation results as long as we set n_max greater than 10.

4.3.2 Quadrupole magnet

The stepwise z-dependence of $G(z)$ leads to a worse convergence of simulation results since a sufficiently fine time step is required to reflect the rapid change in transverse focusing force. In addition, the real quadrupole magnets more or less have fringe fields, and the quadrupole gradients are expected to get stronger smoothly as one moves from the outside to the inside along the design orbit. Thus, we take the fringe field effect into account to guarantee the accuracy of the simulation with a relatively small number of time steps. Then the quadrupole gradient of ith magnet is given by

$$G(z) = G_i[F(z - z_i - \ell_i/2) - F(z - z_i + \ell_i/2)], \tag{4.23}$$

where $F(z)$ is a function defined by

$$F(z) = \frac{1}{2}\left[1 - \frac{z}{8}\left(\frac{1}{r_1} + \frac{1}{r_2}\right)\left(\frac{v_1^2 v_2^2 (v_1^2 + v_1 v_2 + v_2^2 + 4 + 8/v_1 v_2)}{v_1 + v_2}\right)\right], \quad v_i = \sqrt{1 + \left(\frac{z}{r_i}\right)^2}, \tag{4.24}$$

where z_i represents the center position of the ith quadrupole magnet [63]. r_1 and r_2 are outer and inner radius of the quadrupole magnet. In later simulations, r_1 and r_2 are set to 12 mm, which approximately reproduces the fringe fields of the quadrupole magnets installed in the J-PARC DTL.

Figure 4.4 shows an example of $G(z)$ for one FODO period. Then the FODO lattice consists

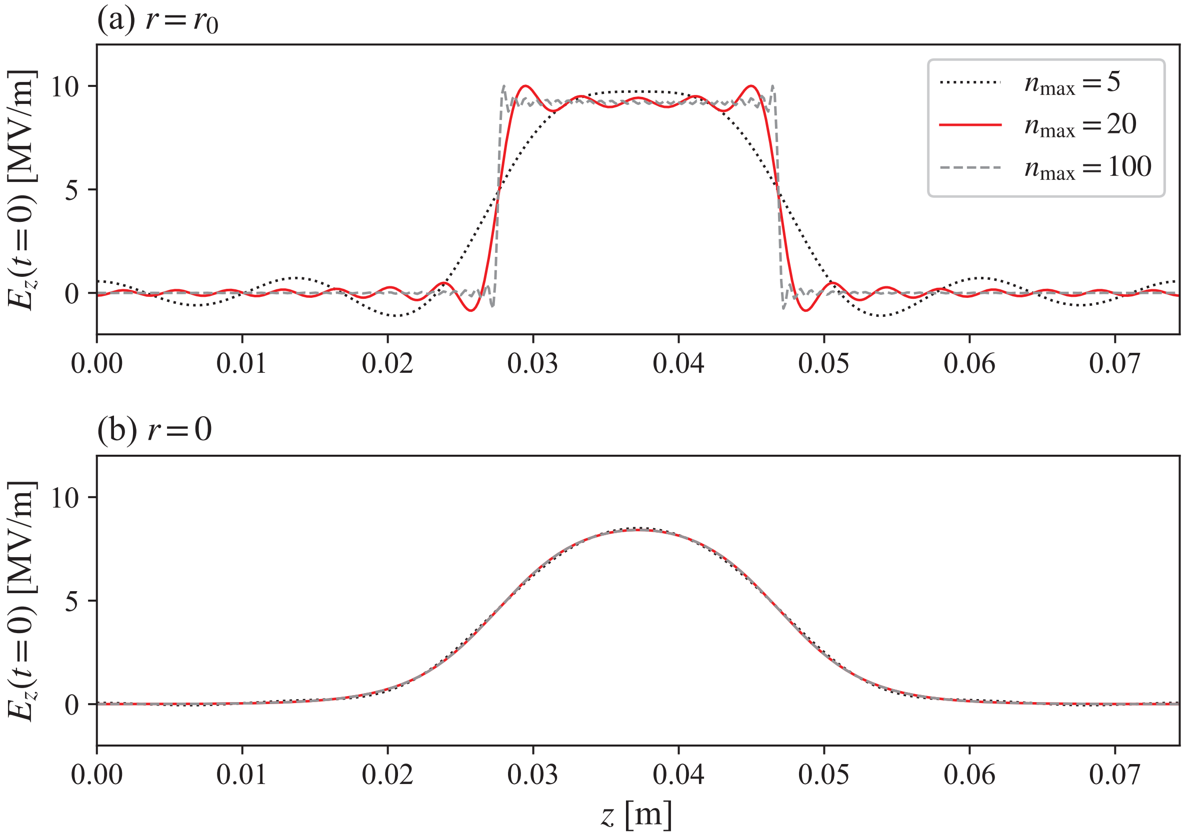

Figure 4.3: Amplitude of the accelerating field on (a) $r = r_0$ and (b) $r = 0$ axis.

of half-focusing, defocusing, and half-focusing quadrupole magnets. We have assumed that a H^- beam accelerated from the kinetic energy of 3 MeV to 3.24 MeV through two unit cells. It is found that the fringe fields effect reaches nearly the center of the accelerating gaps, and $G(z)$ varies quite smoothly. In real machines, the effective length ℓ_i changes discontinuity or is kept constant for the sake of better productivity. However, we assume that ℓ_i gets longer continuously and is proportional to the β_{s} for simplicity; namely $\ell_i = \ell_0 \beta_{\mathrm{s}}(z_i)$ where ℓ_0 is a constant, and $\beta_{\mathrm{s}}(z_i)$ denotes the β_{s} at the center of each quadrupole magnet. Here the parameter G_i remains to be determined, and there are infinite sets of G_i. In this study, we consider the following two practical design guidelines based on the phase advances to determine the set of G_i.

Constant tune ratio (design-A)

Each of the G_i is determined so that the ratio of transverse and longitudinal rms phase advances is kept constant; namely

$$\frac{\mu_i \eta_{\perp,i}}{\sigma_i \eta_{\parallel,i}} = \text{Const.} \tag{4.25}$$

Then the equipartitioning condition is expected to be maintained independently of i if the initial emittances and phase advances are adjusted so that Eq. (4.22) is satisfied. This is referred as "equipartitioning setting" and adopted in J-PARC DTL [61, 64–66]. The previous numerical study has shown that the emittance exchange between longitudinal and transverse degrees of freedom caused by coupling resonances can be significantly suppressed by adopting this set-

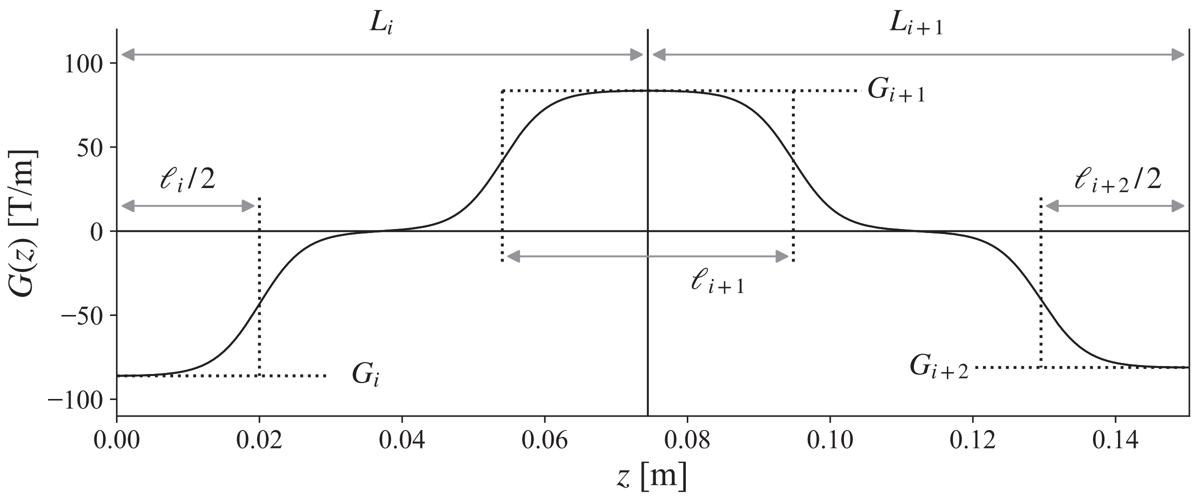

Figure 4.4: z-dependence of the quadrupole gradient for one FODO period.

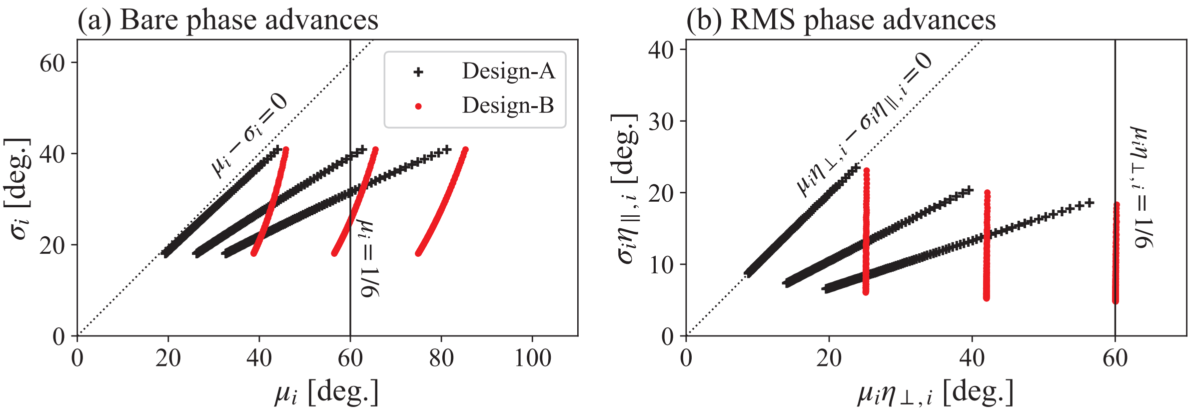

(a) Bare phase advances

(b) RMS phase advances

Figure 4.5: Evolutions of (a) bare phase advances and (b) rms phase advances in design-A and design-B. Three different combinations of starting points have been assumed for each case.

ting [67].

Constant transverse tune (design-B)

In the second design, G_i is set to keep the transverse rms phase advance constant; namely,

$$\mu_i\eta_{\perp,i} = \text{Const.} \tag{4.26}$$

when the transverse beam size is expected to be approximately unchanged. Thus, this setting may enable us to accelerate beams with a larger emittance than design-A in which the beam size is gradually enlarged as the beam's kinetic energy increases.

Comaprison of design-A and design-B

Figure 4.5 shows the shifts of the operating points through 100 FODO units (200 unit cells) for three different combinations of the initial operating point (μ_1, σ_1). Here the acceleration of H^- beam from the kinetic energy 3 to 72 MeV is assumed with the accelerating gradient of 1.6

(a) Design-A

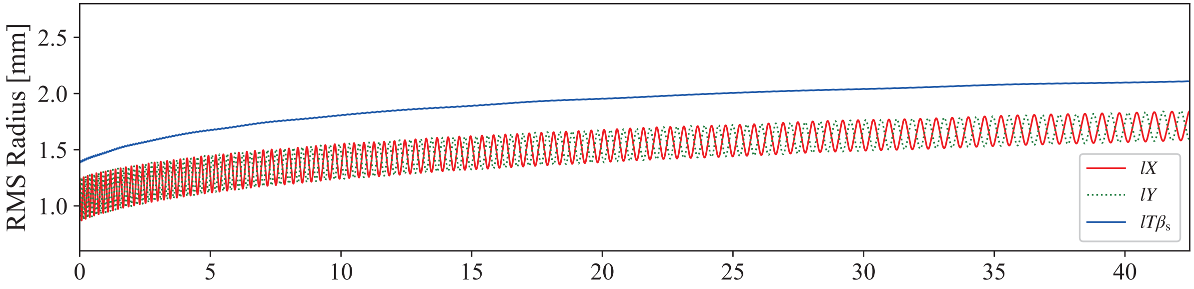

(b) Design-B

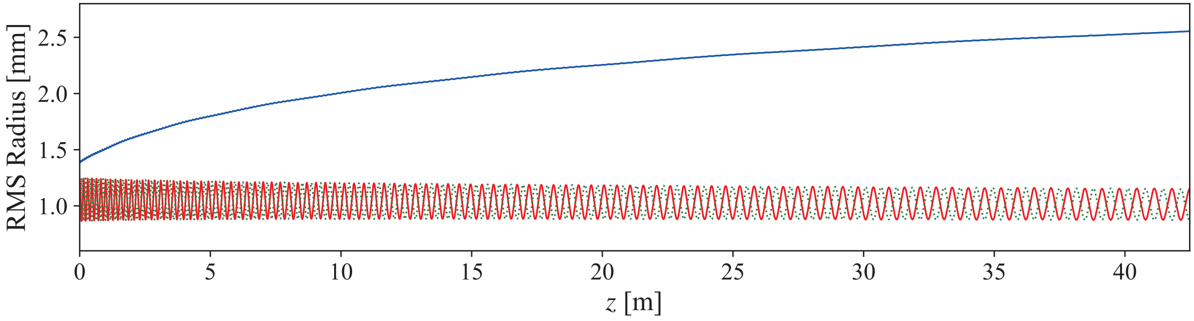

Figure 4.6: Matched rms envelopes in (a) design-A, and (b) design-B. Initial operating point is set at $(\mu_1, \sigma_1) = (39.8°, 32.4°)$ in both Designs.

MeV/m. The transverse and longitudinal emittances are set at 0.22 and 0.295 π mm·mrad, and the peak current is set at 50 mA. These are the same as the design parameters of the J-PARC DTL. As indicated by Eq. (4.17) the longitudinal focusing force decreases proportionally to $1/\beta_s\gamma_s^3$, and the operating longitudinal phase advances shift to lower direction as i increases for all cases. The operating points shift straightly in Fig. 4.5 (b) as expected from the conditions in Eqs. (4.25) and (4.26). The left panel (a) shows the slight curves in the shifts of bare phase advances due to the changes in the tune depressions.

We next take a look at the rms beam radius shown in Fig. 4.6, where the initial operating point set at $(\mu_1, \sigma_1) = (39.8°, 32.4°)$. The other parameters are the same as the case of Fig. 4.5. The upper panel (a) shows that the transverse and longitudinal beam sizes gradually get larger since the transverse focusing force decreases as well as the longitudinal direction. In the case of Fig. 4.5 (b), we can see that the transverse beam sizes remain almost at the same level through the 100 FODO units, while the longitudinal beam size rapidly gets larger. It is confirmed that the difference in transverse and longitudinal tune depressions are also developed as $(\eta_{\perp,i}, \eta_{\parallel,i})$ changes from $(0.55, 0.50)$ to $(0.66, 0.28)$ in 200 units. Thus, the space charge effect seems to contribute to the rapid growth of the longitudinal beam size in the case of design-B; in other words, the compression in the transverse direction likely leads to dissipation in the longitudinal direction.

Table 4.1: Main simulation parameters.

Ion species	H$^-$
Accelerating gradient	1.6 [MV/m]
Transit time factor	0.2
Initial kinetic energy	3 [MeV]
Output kinetic energy	72 [MeV]
Number of FODO cells (unit cells)	100 (200)
Transversal normalized emittance at injection	0.220 [π mm·mrad]
Longitudinal normalized emittance at injection	0.295 [π mm·mrad]
Peak beam current	50 [mA]
RF frequency	324 [MHz]
Effective length of the 1st quadrupole magnet (ℓ_1)	40 [mm]

4.4 Self-consistent numerical simulation

4.4.1 Basic parameters

The basic parameters of our simulations are summarized in Table 4.1. We reference the design parameters of J-PARC DTL as an example [49, 65]. The original design had a structure length of 26.7 m with 146 accelerating gaps, whereas we here assume a structure length of 43 m with 200 accelerating gaps, and the output kinetic energy increases from 50 to 72 MeV. The other configurations are quite similar to the original design except that a continuous DTL structure ignoring the connection between the DTLs is assumed for simplicity. As mentioned above, the equipartitioning setting is adopted in J-PARC DTL, and the equipartitioning condition in Eq. (4.22) is satisfied at the initial operating point of J-PARC DTL $(\mu_1, \sigma_1) = (39.8°, 32.4°)$ when the beam parameters shown in Table 4.1 are chosen.

4.4.2 Initial distributions

Considering that the beams in linac have much higher density in phase space, it is more important than the 2D cases in the previous chapter to construct initial particle distribution well adapted to the lattice. Here, we again employ the pseudo-equilibrium distributions proposed by Steven *et al.* [35]. We have generalized their procedure for the 3D case with the simulation study of bunched beams in mind (see appendix D).

Typical pseudo equilibrium waterbag (WB) and thermal equilibrium (TE) distributions are shown in Fig. 4.7. We here assume a H$^-$ beam with the betatron and synchrotron phase advances of 39.8° and 32.4° at injection, and the main beam parameters are given by Table 4.1. Then, the transverse and longitudinal tune depressions become 0.54 and 0.51 in both cases. We can see that the phase space configurations are deformed into a rectangle-like shape due to the nonlinear nature of the Coulomb potential.

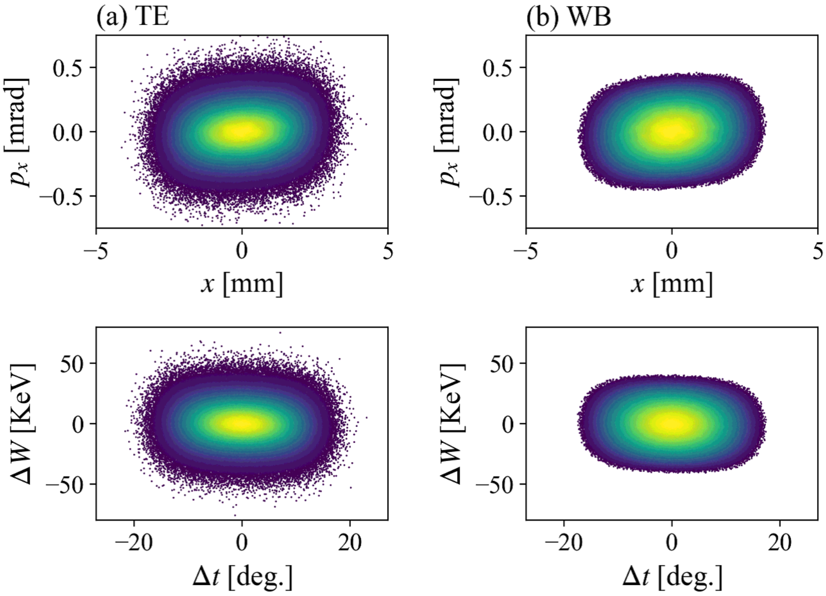

Figure 4.7: Initial particle distributions of (a) Gaussian and (b) waterbag beams in the horizontal and longitudinal phase spaces.

4.5 3D coherent resonance condition

Before proceeding to numerical simulation, we introduce the coherent resonance condition generalized to include the synchrotron resonance given by

$$\begin{aligned} n_x\mu_{x,i}[1 - C_m(1 - \eta_{x,i})] &+ n_y\mu_{y,i}[1 - C_m(1 - \eta_{y,i})] \\ &+ n_\parallel\sigma_{\parallel,i}[1 - C_m(1 - \eta_{\parallel,i})] = \pi n, \end{aligned} \tag{4.27}$$

where n_x, n_y, and $n_\parallel$ are integers. The resonance order is defined by $m = |n_x| + |n_y| + |n_\parallel|$. $\mu_{x(y)}$ and $\sigma_\parallel$ are the bare phase advances calculated considering the RF-defocusing. Except for that the factor of 2π is muliplied, the definition of $\mu_{x(y)}$ and $\sigma_\parallel$ are basically same as $\nu_{0x(0y)}$. This resonance condition is the straightforward generalization of the 2D coherent resonance condition in Eq. (3.1). It was concluded in previous works that the 3D coherent resonance condition in Eq. (4.27) well reproduces the feature of numerical and experimental results, in spite of its remarkably simple form [67]. It was also confirmed that the stopbands positions can be well fitted with the same tune shift factors determined numerically in Chapter 3; namely $C_2 = 0.7$, $C_3 = 0.8$, and $C_4 = 0.9$. Assuming the symmetry of the horizontal and vertical motions, we can simplify the Eq. (4.27) as

$$n_\perp\mu_i[1 - C_m(1 - \eta_{i\perp})] + n_\parallel\sigma_i[1 - C_m(1 - \eta_{i\parallel})] = \pi n, \tag{4.28}$$

where $n_\perp$ is an integer.

The generalization of the stability tune has been discussed by Okamoto *et al.* [68], and we here introduce it for later convenience. The bandwidth is given by

$$\Delta w_{m,i} = 2(1 - C_m)\frac{1 - \bar{\eta}_i}{\bar{\eta}_i}\bar{\nu}_i f'_{n_\perp,n_\parallel}\,, \tag{4.29}$$

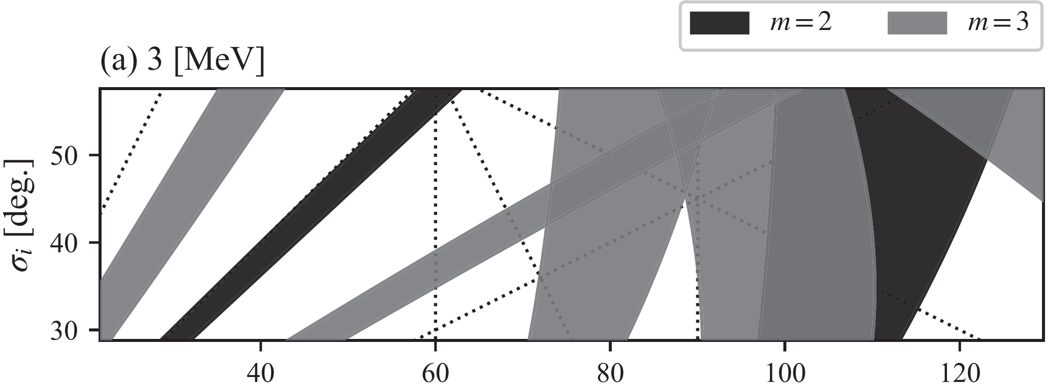

(a) 3 [MeV]

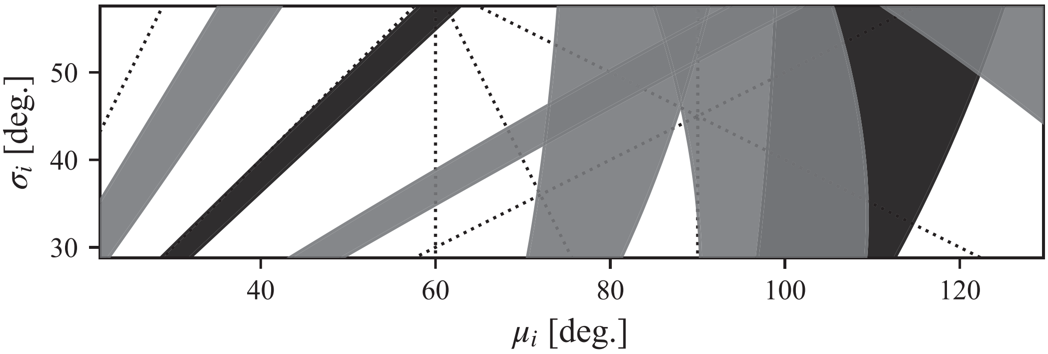

(b) 72 [MeV]

Figure 4.8: Stability tune diagram constructed based on Eqs. (4.28) and (4.29). The initial kinetic energy of (a) 3 MeV and (b) 72 MeV is assumed. The coherent resonance bands of up to 3rd-order are drawn.

where $\bar{\eta}_i \equiv (\eta_{x,i} + \eta_{\parallel,i})/2$, $\bar{\nu}_i \equiv (\mu_{x,i} + \sigma_{\parallel,i})/2$, and $f_{n_\perp,n_\parallel}$ is a factor defined by

$$f'_{n_\perp,n_\parallel} = \frac{|n_\parallel \epsilon_\perp + n_\perp \epsilon_\parallel|}{|n_\parallel|\epsilon_\perp + |n_\perp|\epsilon_\parallel} \, . \tag{4.30}$$

It has been confirmed that the generalized stability tune diagram can explain the experimental observation in a linear Paul trap fairly well. As shown in Fig. 4.8, we construct a stability tune diagram in μ_i-σ_i plane assuming the main beam parameters given in Table 4.1 for example. The coherent stopbands of up to the 3rd order are drawn in the figure. In this case, the tail resonance effect is expected to be ignorable since the operating point shifts within a sufficiently shorter time than the development of the tail resonances. In addition, the coherent collective effects should be much more important than the incoherent effects because of the relatively strong space-charge force. The upper panel (a) shows the stability tune diagram at injection, and the other corresponds to the output. We can hardly detect a significant difference between the two panels. In general, the tune depression tends to approach unity as the beam's kinetic energy increases. However, the effect seems to be counteracted by the phase space compression caused by the reduction in emittances accompanied by the increase in the beam's kinetic energy.

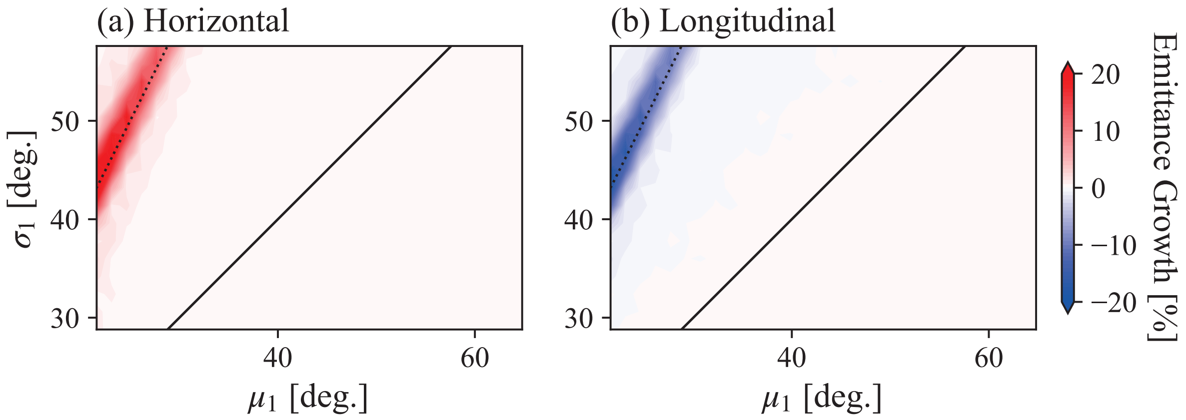

Figure 4.9: Simulation results obtained with the zero-current waterbag beam in design-A. The growth rates of the (a) horizontal and (b) longitudinal normalized emittances evaluated at the exit of the DTL are color-coded in μ_1-σ_1 plane. Except for the peak current, the main simulation parameters are given in Table 4.1.

4.6 Simulation results

4.6.1 Zero beam current

We first focus on the external field-driven resonances. As mentioned in Sec. 4.2, the accelerating field has nonlinear components and can be a source of synchrobetatron coupling resonances. In order to eliminate the space charge effect, the peak current is set at 0 mA. Figure 4.9 shows the simulation result assuming the beam parameters given in Table 4.1 except for the peak current. The abscissa and ordinate represent the horizontal and vertical initial bare phase advances. The quadrupole gradients are determined based on design-A, and the operating points shift straightly to the $(\mu_i, \sigma_i) = (0°, 0°)$ in this case since the tune depressions are always equal to 1. The rate of emittance growth evaluated at 21×29 different combinations of initial phase advances at the exit of 100th FODO units are color-coded. Note that the operating phase advances are much lowered during the 100 FODO unit from the initial phase advances.

The dotted line represents the single-particle resonance condition at injection given by $2\mu_1 - \sigma_1 = 0$. This resonance is driven by the 3rd-order nonlinear term proportional to $\Delta t r^2$ that is present in the Hamiltonian in Eq. (4.13). As expected from the Hamiltonian in Eq. (4.13), clear emittance exchange between transverse and longitudinal degrees of freedom can be seen along the dotted line.

4.6.2 Constant tune ratio

The simulation results in Figs. 4.10 and 4.11 are obtained using the matched waterbag and Gaussian beams. The simulation parameters are listed in Table 4.1, and the quadrupole gradients are determined based on design-A. The abscissa and ordinate represent the horizontal and vertical initial bare phase advances as well as Fig. 4.9. The dotted and solid lines show the 3rd-order and 2nd-order single-practical resonance conditions at injection given by $2\mu_1 - \sigma_1 = 0$ and $\mu_1 - \sigma_1 = 0$ respectively. The rates of emittance growth after 100 FODO units at 21×72 different combinations of initial phase advances are color-coded.

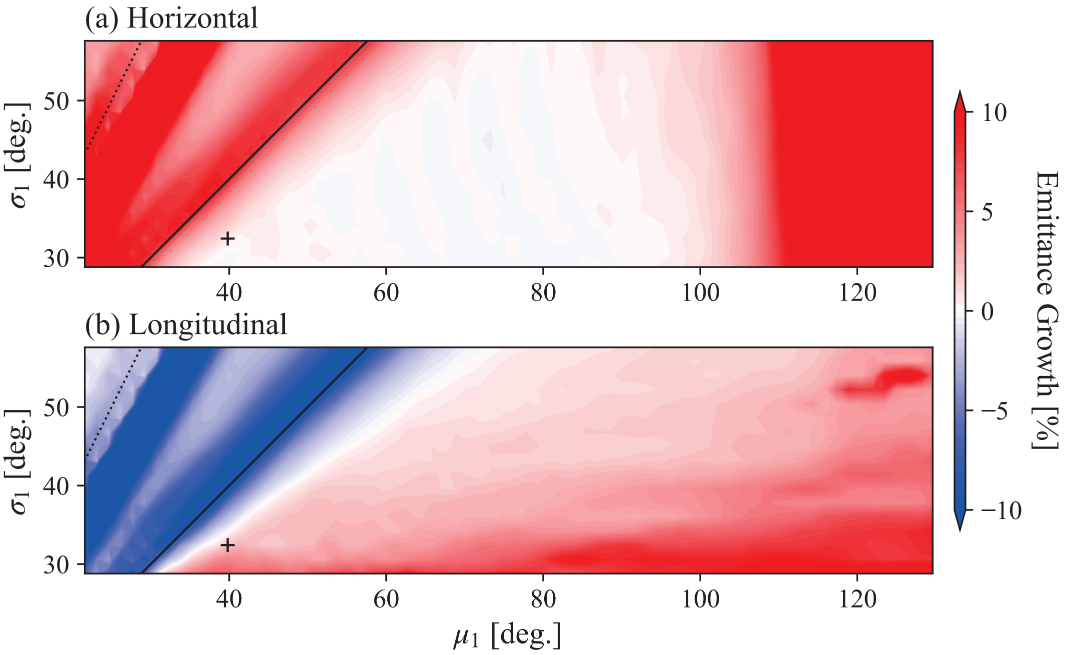

Figure 4.10: Simulation results obtained with the waterbag beam in design-A. The growth rates of the (a) horizontal and (b) longitudinal normalized emittances evaluated at the exit of the DTL are color-coded in μ_1-σ_1 plane. Main simulation parameters are given in Table 4.1.

It is confirmed that there is no significant difference in both cases except for the emittance growth of the lower σ_1 region in the Gaussian case. Given that the particle distribution of the Gaussian beam is much broader than that of the waterbag beam, this can be attributed to the nonlinearity of the accelerating field. The + marker represents the initial phase advances of the J-PARC DTL $(\mu_1, \sigma_1) = (39.8°, 32.4°)$. Since we can detect only a few percent of emittance growth in both of the directions around it, the current operating configuration of J-PARC DTL may be appropriate. The emittance growth in the $\mu_1 > 90°$ region is the well-known envelope instability. In addition to this, we can see that the emittance exchange between the transverse and longitudinal directions occurs along the each of lines. The stopband along the solid line should be caused by the self-field-driven 2nd-order resonance with $(n_\perp, n_\parallel, n) = (1, 1, 0)$. The stopband with $(n_\perp, n_\parallel, n) = (2, 1, 0)$ along the dotted line should be mainly driven by the external nonlinear field since the self-field-driven 3rd order stopband with $(n_\perp, n_\parallel, n) = (1, 2, 0)$ can not be detectable.

Figures 4.12 and 4.13 show the comparison of the stability tune diagram and the simulation results. The hatch represents the coherent resonance bands with $(n_\perp, n_\parallel, n) = (2, 1, 0)$, $(1, 1, 0)$, and $(2, 0, 1)$, where only the observable instabilities in Figs. 4.10 and 4.11 are drawn. The stopbands with $(n_\perp, n_\parallel, n) = (2, 0, 1)$ are only drawn in upper panels since it is kind of a non-coupling resonance and develops within the transverse direction. The markers show the shifts of operating points through 100 FODO units for 37 different combinations of initial phase advances and are color-coded based on the local emittance growth. The stability tune diagram suggests that the coherent resonance band moves to a higher μ_i side induced by the space-charge force, and this is consistent with the numerical observation for the three stopbands. In addition, it is shown that the emittance growth occurs when the operating points across the stop bands given by the coherent resonance conjectures in Eqs. (4.28) and (4.29).

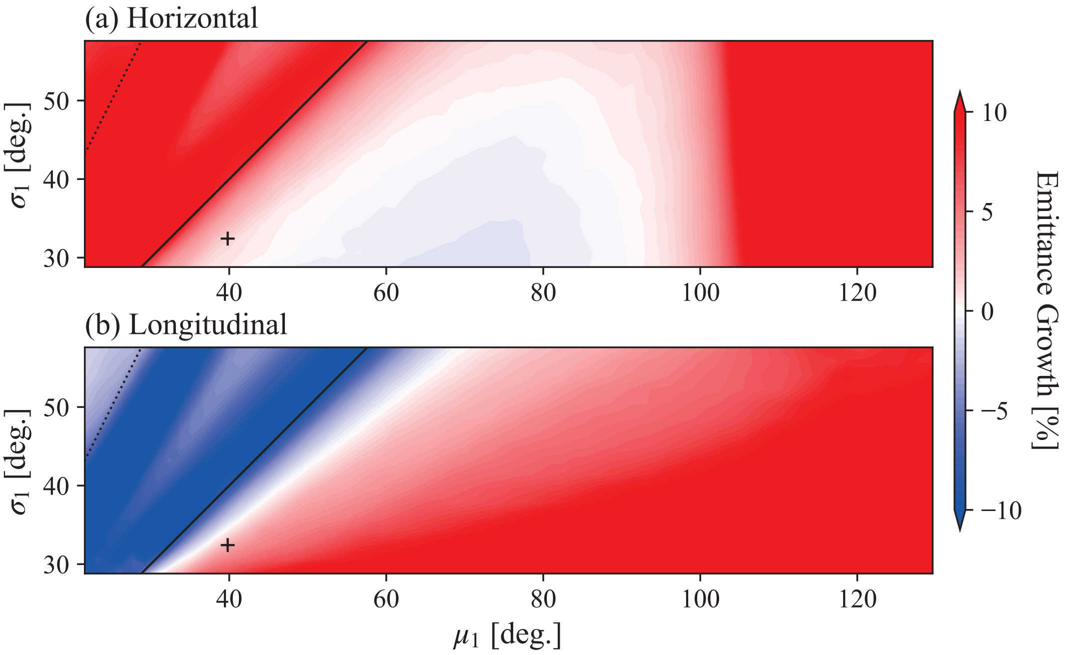

Figure 4.11: Simulation results obtained with the Gaussian beam. Except for the initial distribution, all simulation conditions are the same as employed in Fig. 4.10.

4.6.3 Equipartitioning setting

The tune diagram in Fig. 4.14 is obtained with the equipartitioning setting, where the initial longitudinal emittances are chosen so that the condition in Eq. (4.22) is satisfied at injection for each operating points. Other numerical conditions are the same as in Fig. 4.10, and the initial distribution is the waterbag-type. The difference resonance instabilities with $(n_\perp, n_\parallel, n) = (2, -1, 0)$ and $(1, -1, 0)$ are significantly suppressed. Thus, the equipartitioning setting has the practical advantage that the usable operating region on the tune space is considerably widened by suppressing the difference resonance instabilities.

Figures 4.15 shows the stability tune diagram and the evolutions of emittance growths obtained from simulations with 37 different combinations of initial phase advances. The definition of the hatches and dotted lines are the same as in Fig. 4.12. Since the $f'_{1,-1}$ and $f'_{2,-1}$ are nearly equal to 0 within the two corresponding difference resonance bands, their bandwidths are quite narrow. It is worth mentioning that the emittance exchanges on the two difference resonances are made inactive. We here introduce the emittance-based parameter defined as

$$I'_{n_\perp,n_\parallel} \equiv \frac{\epsilon_\perp}{n_\perp} + \frac{\epsilon_\parallel}{n_\parallel}. \tag{4.31}$$

This is the straightforward generalization of Eq. (3.16). It is confirmed that $I'_{n_\perp,n_\parallel} = 0$ is satisfied for the two difference resonances. Thus, the finding mentioned in Chapter 3 for continuous beams is found to be still valid in the case of bunched beams, which supports the argument in Ref. [67].

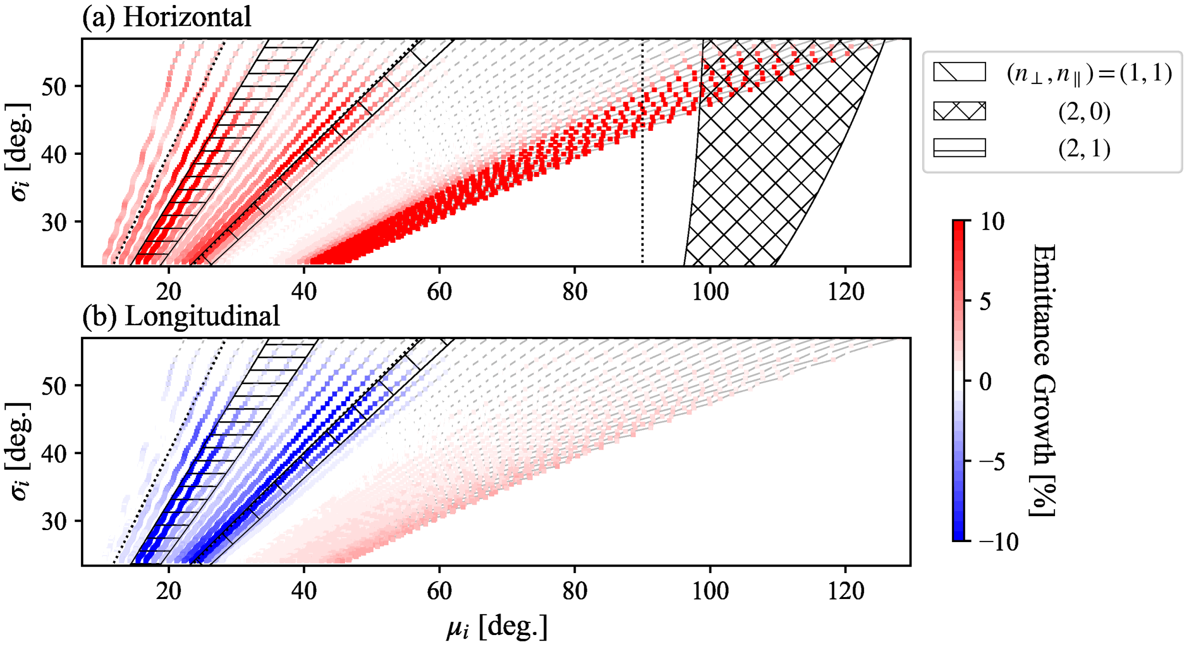

Figure 4.12: Stability tune diagram obtained from Eqs. (4.28) and (4.29). The square dots show the evolutions of bare phase advances and are color-coded based on the local growth rates of the (a) horizontal and (b) longitudinal normalized emittances obtained with the waterbag beam in design-A.

4.6.4 Constant transverse tune

Figure 4.16 shows the IMPACT data obtained under the design-B. The initial beam parameters are similar to the case in Fig. 4.10. The excitation of difference resonances is clearly observed in the higher σ_1 region than the dotted line given by $\mu_1 - \sigma_i = 0$. In addition to this, we can detect the slight emittance growth caused by the 3rd-order coherent resonance with $(n_\perp, n_\parallel, n) = (3, 0, 1)$. Since the operating points shift downward in μ_i-σ_i plane and stay within the stopband relatively long time, the effect of the non-coupling betatron resonance is expected to be higher than in the case of Fig. 4.10. It is worth noting that we can find a resonance-free region with sufficient width still in this case. Furthermore, given the larger acceptable emittance can be provided than the equipartitioning setting, the design-B should also be one of the viable settings for the DTL.

Next, let us compare the simulation results with the stability tune diagram. Considering that the operating points shift downward almost straightly as shown in this figure, it may be difficult to avoid the instability of difference resonance with $(n_\perp, n_\parallel, n) = (1, 1, 0)$ when the initial operating point is chosen within a region defined by $\sigma_1 > \mu_i$.

We can see the 3rd-order betatron resonance locate just on the position theoretically predicted from Eq. (4.28). On the other hand, the 3rd-order stopband is much weaker and narrower than others. This may be due to the low distortion of the initial particle distribution. We employ the digit-reserved numbers to minimize the distortion of the initial particle distribution and reduce the statistical noise. The asymmetry of the particle distribution in real space originating from the initial distortion should be the seed of the self-field-driven parametric instabilities, especially for odd modes. Given that realistic beams are more distorted, the effect of 3rd-order betatron resonance should be underestimated in our case. Thus the result in Fig. 4.15 alone may

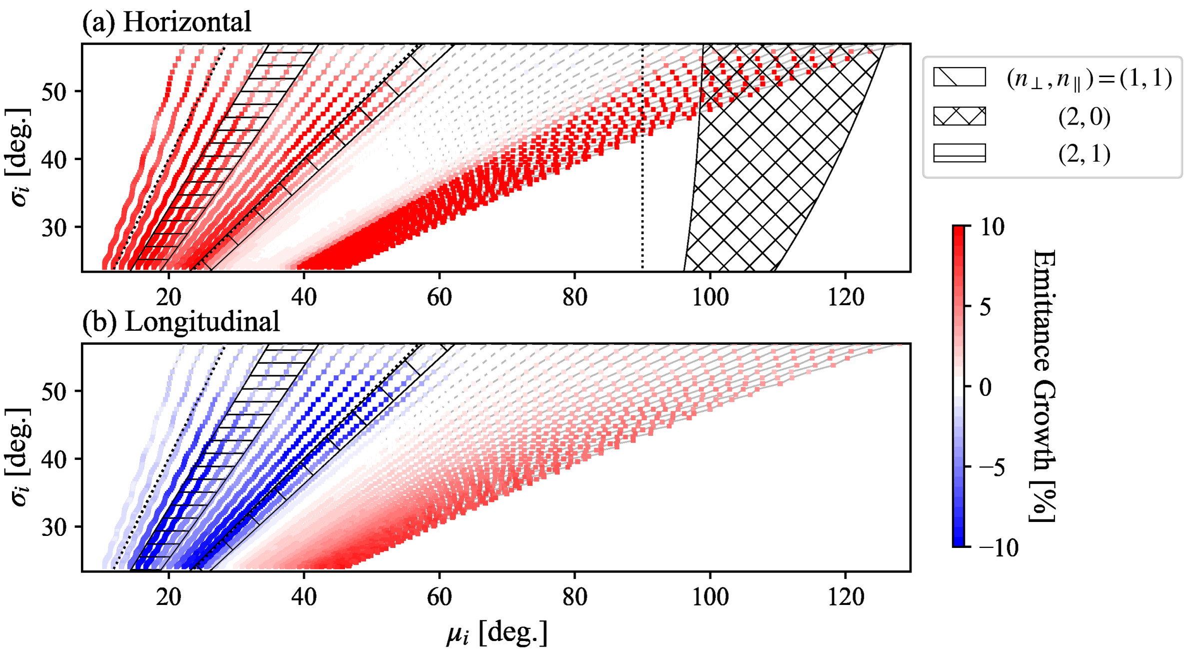

Figure 4.13: Stability tune diagram and simulation results obtained with the Gaussian beam. Except for the initial distribution, all conditions are the same as employed in Fig. 4.12.

be insufficient to measure the danger of the 3rd-order instability. A similar discussion can be found in Ref. [69].

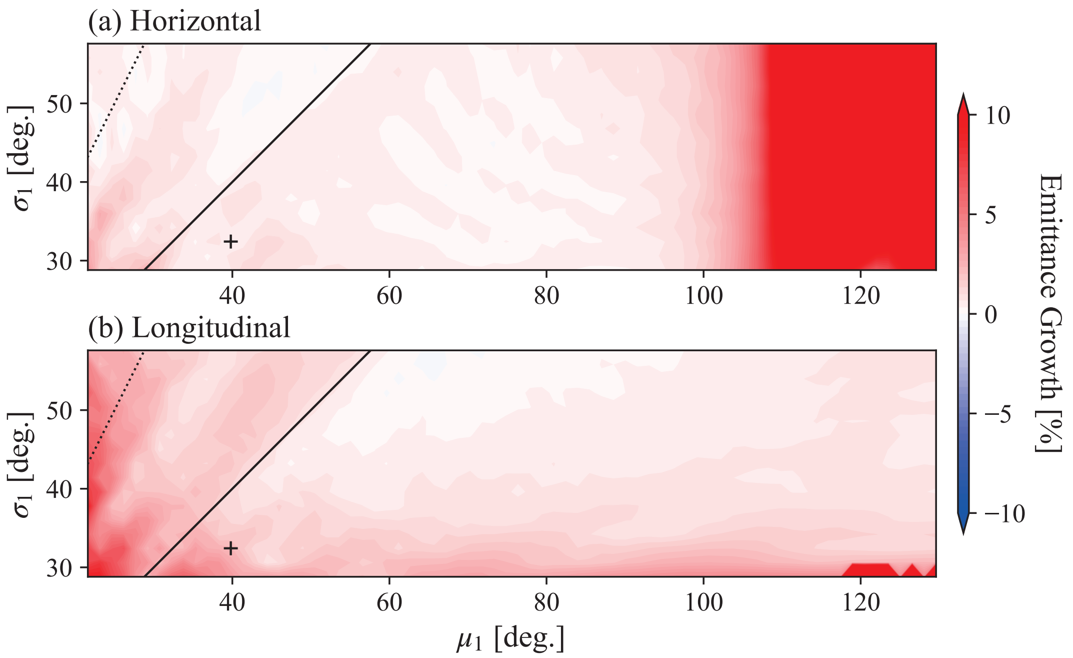

Figure 4.14: Simulation results obtained with the waterbag beam in design-A. The growth rates of the (a) horizontal and (b) longitudinal normalized emittances evaluated at the exit of the DTL are color-coded in μ_1-σ_1 plane. The initial transverse emittances are fixed at 0.220 πmm·mrad, while the initial longitudinal emittance is chosen so as to meet the equipartitioning condition in Eq. (4.22).

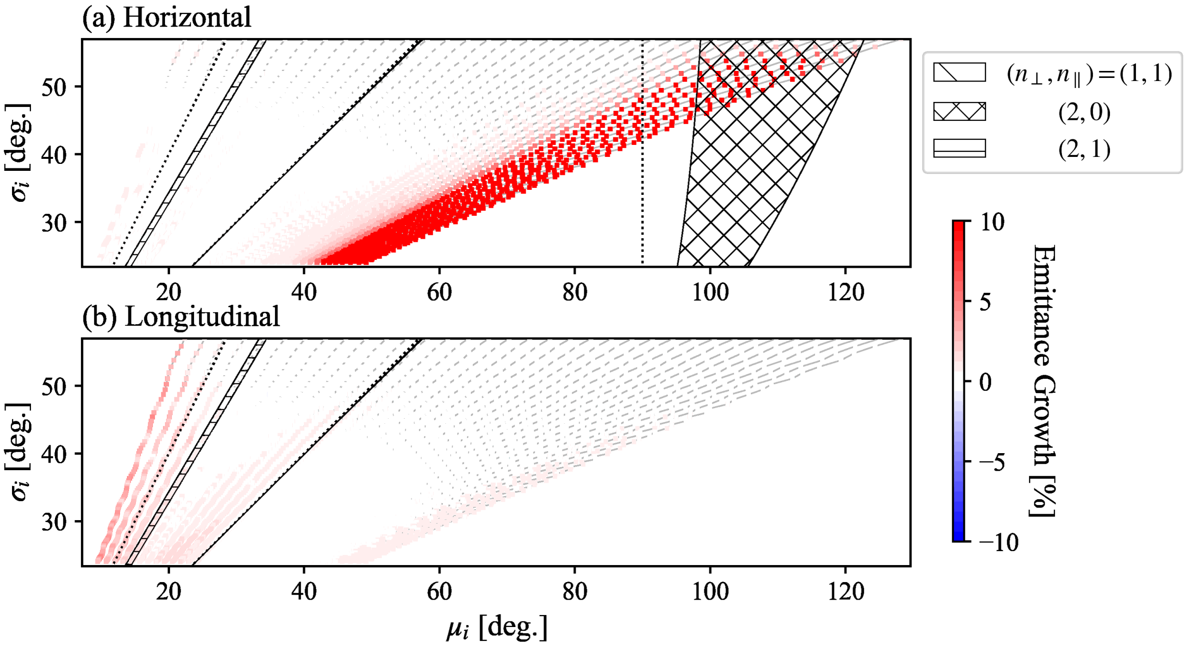

Figure 4.15: Stability tune diagram and simulation results obtained with the waterbag beam in design-A. The initial longitudinal emittances for each simulation are chosen so that the equipartitioning condition in Eq. (4.22). Other conditions are the same as employed in Fig. 4.12.

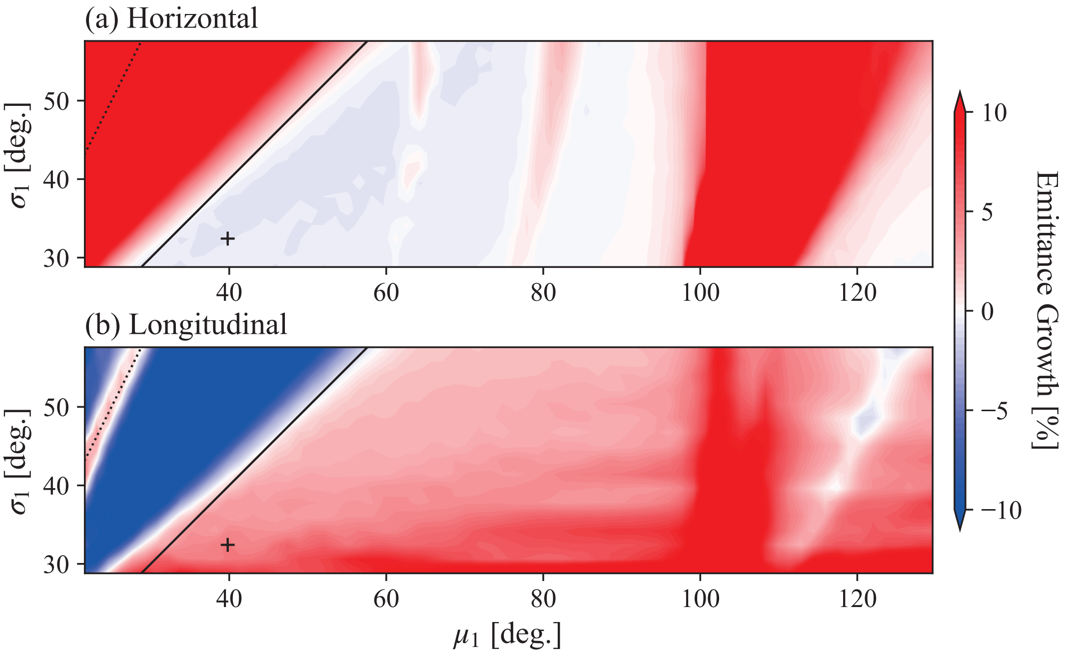

Figure 4.16: Simulation results obtained with the waterbag beam in design-B. The growth rates of the (a) horizontal and (b) longitudinal normalized emittances evaluated at the exit of the DTL are color-coded in μ_1-σ_1 plane. Main simulation parameters are given in Table 4.1.

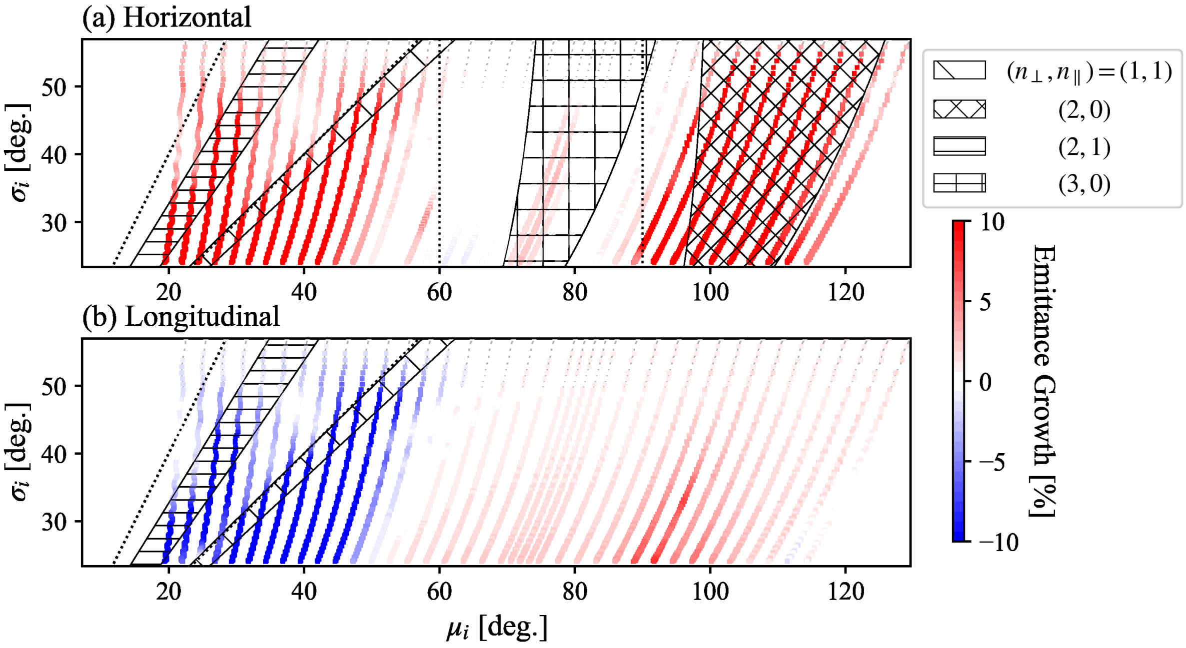

Figure 4.17: Stability tune diagram and simulation results obtained with the waterbag beam in design-B. Except for the channel design, all conditions are the same as employed in Fig. 4.12.

4.7 Summary

We have investigated resonant instabilities in high-intensity bunched beams propagating through linear accelerators. The self-consistent numerical simulations are conducted for this purpose over a wide parameter range employing an analytic model. The IMPACT simulation results assuming the design parameters of J-PARC DTL suggest that the low-order resonance crossing of operating points leads to the emittance growth or emittance exchange in transverse and longitudinal directions. It is also confirmed that the emittance exchange can be significantly mitigated by choosing the proper ratio of the initial emittances of transverse and longitudinal directions as well as the 2D case discussed in Chapter 3.

The equipartitioning setting is found to automatically give the proper emittance ratio and is preferable to broaden the usable operating region in tune space. However, the equipartitioning setting may not be essential. For example, the simulation results under the constant transverse phase advance settings also show that the beams can be accelerated with a sufficiently low emittance growth in three directions. Therefore, we have to not adhere to the equipartitioning setting but be flexible in pursuing the optimum linac design from a practical point of view.

We have also proposed a 3D generalized coherent resonance condition. The comparison of simulation results and the stability tune diagram constructed on the basis of the coherent resonance condition shows good agreement. On the other hand, the effects of self-field-driven parametric resonances may be underestimated in our simulations due to the low distortion of the initial particle distribution. Further investigations should be needed to provide more reliable information without overlooking dangerous resonant instabilities.

Bibliography

[1] S. Y. Lee, *Accelerator Physics* (World Scientific, Singapore, 1999).

[2] E. D. Courant and H. S. Snyder, Theory of the alternating-gradient synchrotron, Annals of Physics **3** (1), 1 (1958).

[3] Liouville, J. Math. Pures Appl. **3**, 342 (1838).

[4] H. Wiedemann, *Particle Accelerator Physics* (Springer-Verlag, 1993).

[5] A. W. Chao, M. Tigner (Eds.), *Handbook of Accelerator Physics and Engineering* (World Scientific, Singapore, 1999) and references therein.

[6] M. Conte and W. M. MacKay, *An Introduction to the Physics of Particle Accelerators* (World Scientific, Singapore, 1991).

[7] F. J. Sacherer, RMS envelope equations with space charge, IEEE Trans. Nucl. Sci. **NS-18**. 1105 (1971).

[8] F. J. Sacherer, Ph.D Thesis, Lawrence Radiation Laboratory, 1968; Report No. UCRL-18454, 1968.

[9] H. Bartosik, F. Asvesta, A. Huschauer, Y. Papaphilippou, and F. Schmidt, Space charge induced losses in the CERN injector complex, J. Instrum. **15**, P07021 (2020).

[10] F. Asvesta, H. Bartosik, A. Huschauer, Y. Papaphilippou, and G. Sterbini, Resonance identification studies at the CERN PS, J. Phys. Conf. Ser. **1067**, 062021 (2018).

[11] M. Bassetti and G. A. Erskine, Closed expression for the electrical field of a two-dimensional Gaussian charge, CERN-Report, CERN-ISR-TH/80-06 (1980).

[12] I. Hofmann, Stability of anisotropic beams with space charge, Phys. Rev. E **57**, 4713 (1998).

[13] M. Reiser, *Theory and Design of Charged Particle Beams* (John Wiley & Sons, New York, 2008) and references therein.

[14] R. L. Gluckstern, Oscillation modes in two-dimensional beams, in *Proceedings of the 1970 Linear Accelerator Conference*, edited by M. R. Tracy (Fermilab, Batavia, Illinois, 1970), p. 811.

[15] L. Smith, Effect of gradient errors in the presence of space charge forces, Proceedings of the 4 th International Conference on High-Energy Accelerators, edited by A. A. Kolomenskij and A. B. Kuznetsov (Dubna, USSR, 1963), p. 1232.

[16] J. Struckmeier and M. Reiser, Theoretical studies of envelope oscillations and instabilities of mismatched intense charged-particle beams in periodic focusing channels, Part. Accel. **14**, 227 (1983).

[17] S. Machida, Space charge effects in low-energy proton synchrotrons, Nucl. Instrum. Meth. A **309**, 43 (1991).

[18] S. M. Lund and R. C. Davidson, Warm-fluid description of intense beam equilibrium and electrostatic stability properties, Phys. Plasmas **5**, 3028 (1998).

[19] M. Venturini and R. L. Gluckstern, Resonance analysis for a space charge dominated beam in a circular lattice, Phys. Rev. ST Accel. Beams **3**, 034203 (2000).

[20] H. Okamoto and K. Yokoya, Parametric resonances in intense one-dimensional beams propagating through a periodic focusing channel, Nucl. Instrum. Meth. A **482**, 51 (2002).

[21] A. V. Fedotov, I. Hofmann, R. L. Gluckstern, and H. Okamoto, Parametric collective resonances and space-charge limit in high-intensity rings, Phys. Rev. ST Accel. Beams **6**, 094201 (2003).

[22] I. Hofmann, G. Franchetti, J. Qiang, and R. Ryne, Self-consistency and coherent effects in nonlinear resonances, AIP Conf. Proc. **693**, 65 (2003).

[23] R. Baartman, Betatron resonances with space charge, AIP Conf. Proc. **448**, 56 (1998).

[24] T. H. Stix, *Waves in Plasmas*, (Springer, 1992).

[25] R. C. Davidson, *Physics of Nonneutral Plasmas*, (World Scientific, Singapore, 2001).

[26] K. Ito, M. Matsuba, and H. Okamoto, Effect of quadrupole focusing-field fluctuation on the transverse stability of intense hadron beams in storage rings, Prog. Theor. Exp. Phys. **2018**, 023G01 (2018).

[27] J. Struckmeier, J. Klabunde, and M. Reiser, On the stability and emittance growth of different particle distributions in a long magnetic quadrupole channel, Part. Accel. **15**, 47 (1984).

[28] A. V. Fedotov, R. L. Gluckstern, S. S. Kurennoy, and R. D. Ryne, Halo formation in three-dimensional bunches with various phase space distributions, Phys. Rev. ST Accel. Beams **2**, 014201 (1999).

[29] D. P. Grote, A. Friedman, G. Craig, I. Haber, and W. Sharp, Progress toward source-to-target simulation, Nucl. Instrum. Meth. A **464**, 563 (2001).

[30] I. Hofmann, *Space charge physics for particle accelerators*, (Springer, 2017) and references therein.

[31] K. Fukushima, K. Ito, H. Okamoto, S. Yamaguchi, K. Moriya, H. Higaki, T. Okano, and S. M. Lund, Experimental verification of resonance instability bands in quadrupole doublet focusing channels, Nucl. Instrum. Meth. A **733**, 18 (2014).

[32] K. Ito, H. Okamoto, Y. Tokashiki, and K. Fukushima, Coherent resonance stop bands in alternating gradient beam transport, Phys. Rev. Accel. Beams **20**, 064201 (2017).

[33] H. Okamoto and M. Ikegami, Simulation study of halo formation in breathing round beams, Phys. Rev. E **55**, 4694 (1997).

[34] I. Hofmann and J. Struckmeier, Generalized threedimensional equations for the emittance and field energy of high-current beams in periodic focusing structures, Part. Accel. **21**, 69 (1987).

[35] S. M. Lund, T. Kikuchi, and R. C. Davidson, Generation of initial kinetic distributions for simulation of long-pulse charged particle beams with high space-charge intensity, Phys. Rev. ST Accel. Beams **12**, 114801 (2009).

[36] H. Sugimoto, *Multi-Particle Simulation Studies on the Generation and Stability of High-Density Coulomb Systems*, PhD thesis, 2011.

[37] S. Ohtsubo, M. Fujioka, H. Higaki, K. Ito, H. Okamoto, H. Sugimoto, and S. M. Lund, Experimental study of coherent betatron resonances with a Paul trap, Phys. Rev. ST Accel. Beams **13**, 044201 (2010).

[38] H. Okamoto, K. Fukushima, H. Higaki, D. Ishikawa, K. Ito, T. Iwai, K. Moriya, T. Okano, K. Osaki, and M. Yamaguchi, Beam dynamics studies with non-neutral plasma traps, in *Proceedings of the 5th International Particle Accelerator Conference (IPAC2014)*, Dresden, Germany (JACoW, Geneva, 2014), FRXAA01, p. 4052.

[39] H. Takeuchi, K. Fukushima, K. Ito, K. Moriya, H. Okamoto, and H. Sugimoto, Experimental study of resonance crossing with a Paul trap, Phys. Rev. ST Accel. Beams **15**, 074201 (2012).

[40] K. Moriya, M. Ota, K. Fukushima, M. Yamaguchi, K. Ito, and H. Okamoto, Double stop-band structure near half-integer tunes in high-intensity rings, Phys. Rev. Accel. Beams **19**, 114201 (2016).

[41] H. Okamoto, K. Ito, K. Fukushima, and T. Okano, Recent results from the S-POD trap systems on the stability of intense hadron beams, in *Proceedings of the 54th ICFA Advanced Beam Dynamics Workshop on High-Intensity, High-Brightness and High-Power Hadron Beams (HB2014)*, Michigan, USA (JACoW, Geneva, 2015), TUO2LR03, p. 178.

[42] H. Okamoto, M. Endo, K. Fukushima, H. Higaki, K. Ito, K. Moriya, S. Yamaguchi, and S. M. Lund, Experimental simulation of beam propagation over long path lengths using radio-frequency and magnetic traps, Nucl. Instrum. Meth. A **733**, 119 (2014).

[43] I. M. Kapchinskij and V. V. Vladimirskij, Limitations of proton beam current in a strong focusing linear accelerator associated with the beam space charge, in *Proceedings of the International Conference on High-Energy Accelerators*, CERN, Geneva (1959), p. 274.

[44] I. Hofmann, L. J. Laslett, L. Smith, and I. Haber, Stability of the Kapchinskij-Vladimirskij (K-V) distribution in long periodic transport systems, Part. Accel. **13**, 145 (1983).

[45] S. M. Lund and B. Bukh, Stability properties of the transverse envelope equations describing intense ion beam transport, Phys. Rev. ST Accel. Beams **7**, 024801 (2004).

[46] H. Okamoto, M. Aoki, C. Ichikawa, K. Kojima, T. Kurauchi, and Y. Yamane, "Coherent and incoherent space-charge effects in high-intensity hadron rings", Journal of Instrumentation **15**, P07017 (2020).

[47] W. Montague. Fourth-order coupling resonances excited by space-charge forces in a synchrotron, CERN/ISR/68-38, 1968.

[48] I. Hofmann, G. Franchetti, J. Qiang, and R. Ryne, Dynamical effects in crossing of the Montague resonance, in Proceedings of the 9th European Particle Accelerator Conference (EPAC2004), Lucerne, Switzerland (JACoW, Geneva, 2004), WEPLT053, p. 1960.

[49] Y. Yamazaki *et al.*, KEK Report No. 2002-13 JAERI-Tech Report Nos. 2003-44, J-PARC-03-01, (2003).

[50] H. Hotchi, H. Harada, N. Hayashi, M. Kinsho, P. Saha, Y. Shobuda, F. Tamura, K. Yamamoto, Mz. Yamamoto, M. Yoshimoto, S. Kato, Y. Irie, T. Koseki, Y. Sato, K. Satou, and M. Shirakata, Beam commissioning and operation of the Japan Proton Accelerator Research Complex 3-GeV rapid cycling synchrotron, Prog. Theor, Exp. Phys. **2012**, 02B003 (2012).

[51] H. Hotchi, H. Harada, N. Hayashi, S. Kato, M. Kinsho, K. Okabe, P. K. Saha, Y. Shobuda, F. Tamura, N. Tani, Y. Watanabe, K. Yamamoto, M. Yamamoto, and M. Yoshimoto, Achievement of a low-loss 1-MW beam operation in the 3-GeV rapid cycling synchrotron of the Japan Proton Accelerator Research Complex, Phys. Rev. Accel. Beams **20**, 060402 (2017).

[52] L. Groening, W. Barth, W. Bayer, G. Clemente, L. Dahl, P. Forck, P. Gerhard, I. Hofmann, M. S. Kaiser, M. Maier, S. Mickat, T. Milosic, D. Jeon, and D. Uriot, Experimental evidence of the 90° stop band in the GSI UNILAC, Phys. Rev. Lett. **102**, 234801 (2009).

[53] D.-O. Jeon, Experimental evidence of space charge driven resonances in high intensity linear accelerators, Phys. Rev. Accel. Beams **19**, 010101 (2016).

[54] J. Qiang, R. D. Ryne, S. Habib, and V. Decyk, An object-oriented parallel particle-in-cell code for beam dynamics simulation in linear accelerators, Journal Computational Physics **163**, 434 (2000).

[55] J. Qiang, R. D. Ryne, M. Venturini, and A. A. Zholents, An object-oriented parallel particle-in-cell code for beam dynamics simulation in linear accelerators, Journal Computational Physics **163**, 434 (2000).

[56] J. Qiang, R. D. Ryne, M. Venturini, A. A. Zholents, and I. V. Pogorelov, High resolution simulation of beam dynamics in electron linacs for x-ray free electron lasers, Phys. Rev. ST Accel. Beams **12**, 100702 (2009).

[57] H. Okamoto, K. Kojima, and K. Ito, A compact Paul ion trap for the study of space-charge effects in drift-tube linear accelerators, Prog. Theor. Exp. Phys. **2019**, 093G01 (2019).

[58] P. M. Lapostolle, Proton linear accelerators: A theoretical and historical introduction, Los Alamos National Laboratory Report No. LA-11601-MS, 1989.

[59] T. Wangler, *RF Linear Accelerators* (John Wiley & Sons, New York, 1998) and references therein.

[60] R. D. Ryne, Finding matched rms envelopes in rf linacs: A Hamiltonian approach, Los Alamos Report No. LA-UR-95-391 (1995).

[61] R. A. Jameson, Beam-intensity limitations in linear accelerators, IEEE Trans. Nucl. Sci. **28**, 2408 (1981).

[62] K. Kojima, H. Okamoto, and K. Moriya, Construction of a multi-particle simulation model for the basic designs of high-intensity linear ion accelerators, Proc. 19th Meeting of Particle Accelerator Society of Japan, pp. 486 - 470 (2022).

[63] K. Halbach, Physical and Optical Properties of Rare Earth Cobalt Magnets, Nucl. Instrum. Methods Phys. Res. **187**, 109 (1981).

[64] M. Reiser and N. Brown, Proposed high-current rf linear accelerators with beams in thermal equilibrium, Phys. Rev. Lett. **74**, 1111 (1995).

[65] M. Ikegami, Beam commissioning and operation of the J-PARC linac, Prog. Theor. Exp. Phys. **2012**, 02B002 (2012).

[66] Y. Kondo, T. Morishita, and R. A. Jameson, Development of a radio frequency quadrupole linac implemented with the equipartitioning beam dynamics scheme, Phys. Rev. Accel. Beams **22**, 120101 (2019).

[67] Y. Yamane, H. Okamoto, and K. Kojima, Excitation and suppression of synchrobetatron resonances in high-intensity hadron linacs, Phys. Rev. Accel. Beams **24**, 084201 (2021).

[68] M. Goto, C. Ichikawa, K. Ito, K. Kojima, and H. Okamoto, Stability study of intense hadron bunches in linear accelerators using a Paul ion trap, Phys. Rev. Accel. Beams **25**, 054201 (2022).

[69] K. Kojima, H. Okamoto, and Y. Tokashiki, Empirical condition of betatron resonances with space charge, Phys. Rev. Accel. Beams **22**, 074201 (2019).

[70] See, e.g., K. Y. Ng, *Physics of intensity dependent beam instabilities* (World Scientific, Singapore, 2005).

[71] K. Kojima and H. Okamoto, Generating pseudo-equilibrium phase-space distributions of particles in intense bunched beams focused by an arbitrary periodic lattice, Proc. 18th Meeting of Particle Accelerator Society of Japan, pp. 473 - 477 (2021).

Appendix A

Incoherent tune

In many cases, the size of the tune spread is a primary interest of us. Now let us assume a coasting beam with the Gaussian distribution, and the density profile is given by

$$\varrho(x,y) = \frac{\lambda_p}{2\pi\sigma_x\sigma_y}\exp\left(-\frac{x^2}{2\sigma_x^2} - \frac{y^2}{2\sigma_y^2}\right), \tag{A.1}$$

where λ_p is the line density of the beam, and $\sigma_{x(y)}$ is the average rms beam size. The exponential can be expanded in a power series of x^2 or y^2 as

$$\varrho(x,y) \approx \frac{\lambda_p}{2\pi\sigma_x\sigma_y}\left[1 - \frac{x^2}{2\sigma_x^2} - \frac{y^2}{2\sigma_y^2} + \frac{1}{2}\left(\frac{x^4}{4\sigma_x^4} + \frac{y^4}{4\sigma_y^4} + \frac{x^2y^2}{4\sigma_x^2\sigma_y^2}\right) + \cdots\right]. \tag{A.2}$$

Substituting this equation into Poisson's equation, we obtain the space charge potential

$$\begin{aligned}\phi_{\mathrm{sc}}(x,y) \approx \frac{\lambda_p q}{4\pi\epsilon_0}\Bigg[&- \frac{x^2}{\sigma_x(\sigma_x+\sigma_y)} - \frac{y^2}{\sigma_y(\sigma_x+\sigma_y)} \\ &+ \frac{(2\sigma_x+\sigma_y)x^4}{12\sigma_x^3(\sigma_x+\sigma_y)^2} + \frac{(\sigma_x+2\sigma_y)y^4}{12\sigma_y^3(\sigma_x+\sigma_y)^2} + \frac{x^2y^2}{2\sigma_x\sigma_y(\sigma_x+\sigma_y)^2} + \cdots\Bigg].\end{aligned} \tag{A.3}$$

In general, the incoherent tune shift becomes greater for particles closer to the center of the beam core. Thus, the maximum incoherent tune shift can be evaluated by assuming that $x(y)$ is much lower than $\sigma_{x(y)}$; namely $x/\sigma_x \ll 1$ and $y/\sigma_y \ll 1$ [70]. Then we only need to consider the first two terms in Eq. (A.3), and the maximum incoherent tune can be obtained from Eq. (2.11) as

$$\max(\Delta\nu_x) = \frac{1}{2\pi}\int_{s_0}^{s_0+L} \frac{2\lambda_p r_p \beta_x \cos^2\psi_x}{\beta_{\mathrm{s}}^2\gamma_{\mathrm{s}}^3\sigma_x(\sigma_x+\sigma_y)}\,ds. \tag{A.4}$$

The smooth approximation $\beta_x = L/2\pi\nu_{0x}$ gives

$$\max(\Delta\nu_x) \approx \frac{r_p\lambda_p L^2}{4\pi^2\nu_{0x}\beta_{\mathrm{s}}^2\gamma_{\mathrm{s}}^3\sigma_x(\sigma_x+\sigma_y)}, \tag{A.5}$$

Then the tune depression is approximately given by

$$\eta_x \approx \frac{1}{\nu_{0x}}\sqrt{\left(\frac{2\pi\nu_{0x}}{L}\right)^2 - \frac{K_{\mathrm{sc}}}{2\sigma_x(\sigma_x+\sigma_y)}}\,. \tag{A.6}$$

Substituting this into Eq. (A.5) results in

$$\max(\Delta\nu_x) \approx (1-\eta_x^2)\nu_{0x}. \tag{A.7}$$

Appendix B

1-dimensional Vlasov model

Here we follow the discussion of the 1D Vlasov analysis studied by H. Okamoto and K. Yokoya [20]. The starting point is the 1D Hamiltonian with a small mismatch

$$H = H_0 + \frac{q}{p_0\beta_s c\gamma_s^2}\delta\phi, \tag{B.1}$$

where $\delta\phi$ is the perturbation scaler potential generated by the mismatch. The beam stationary motion is governed by the unperturbed Hamiltonian H_0 given by

$$H_0 = \frac{1}{2}\left[p_x^2 + K_x(s)x^2\right] + \frac{q}{p_0\beta_s c\gamma_s^2}\phi_0(x;s). \tag{B.2}$$

where ϕ_0 denotes the unperturbed self-field potential. Here we suppose that the focusing force is periodic and linear as in Chapter 3. We represent the distribution function f by the sum of the stationary part f_0 which satisfies $df_0/ds = 0$ and perturbing part δf; namely $f = f_0 + \delta f$. Leaving dominant linear terms of δf and $\delta\phi$, the linearized Vlasov equation can be written by

$$\frac{\partial\delta f}{\partial s} + p_x\frac{\partial\delta f}{\partial x} - \frac{\partial H_0}{\partial x}\frac{\partial\delta f}{\partial p_x} = \frac{q}{p_0\beta_s c\gamma_s^2}\frac{\partial f_0}{\partial p_x}\frac{\partial\delta\phi}{\partial x}\,. \tag{B.3}$$

It is necessary to analyze Eq. (B.3) that the stationary distribution f_0 is given. f_0 must satisfy the Poisson equation

$$\frac{\partial^2\phi_0}{\partial x^2} = -\frac{q}{\epsilon_0}\int f_0\, dp_x, \tag{B.4}$$

It can be solved analytically for the distribution having a uniform density in real space but is almost hopeless to solve for other general non-uniform distributions. In order to avoid the difficulty, we introduce linear approximation for the self-field potential as $\phi_0 \approx -qN\zeta(s)x^2/4\pi\epsilon_0$ where N is the number of particles per length. Then the Hamiltonian can be written by

$$H_0 = \frac{1}{2}\left[p_x^2 + Q(s)x^2\right], \tag{B.5}$$

where $Q(s) = K_x - K_{sc}\zeta(s)$. $K_{sc} = q^2N/2\pi\epsilon_0 p_0\beta_s c\gamma_s^2$ is generalized perveance. Then the Hamiltonian can be transformed canonically to $\hat{H}(\psi, J) = J/\hat{\beta}_x$ by the generating function as shown in Eq. (1.22)

$$F_2(x,\psi_x;s) = -\frac{x^2}{2\hat{\beta}_x}\left(\tan\psi_x - \frac{1}{2}\frac{d\hat{\beta}_x}{ds}\right). \tag{B.6}$$

where $\hat{\beta}_x$ satisfies

$$\frac{1}{2}\frac{d^2\hat{\beta}_x}{ds^2} + Q_x\hat{\beta}_x - \frac{1}{\hat{\beta}_x}\left[1 + \left(\frac{1}{2}\frac{d\hat{\beta}_x}{ds}\right)^2\right] = 0, \tag{B.7}$$

then $f_0(J)$ describes stationary distribution because J is a invariant.

Here, we adopt the waterbag model, which has a uniform density in phase space

$$f_0(J) = \frac{N}{2\pi\epsilon}\left[1 + \mathrm{sgn}\left(\frac{\epsilon}{2} - J\right)\right], \tag{B.8}$$

where ϵ denotes the area occupied by the distribution. Looking back over the Eq. (B.3), and using Eq. (B.8) we have

$$\frac{\partial\delta f}{\partial s} + \frac{1}{\hat{\beta}_x}\frac{\partial\delta f}{\partial\psi} = -\frac{2\epsilon_0 K_{\mathrm{sc}}}{q}\sqrt{\frac{\hat{\beta}_x}{\epsilon}}\delta\left(\frac{\epsilon}{2} - J\right)\delta E(\psi, J = \epsilon/2; s)\sin\psi, \tag{B.9}$$

where $\delta(z)$ is the Dirac delta function. δE is the perturbation space charge field and satisfies Poisson equation

$$\frac{\partial\delta E}{\partial x} = \frac{q}{\epsilon_0}\int \delta f\, dp_x. \tag{B.10}$$

Eq. (B.9) suggests that the action dependence of δf can be written by $\delta\left(\epsilon/2 - J\right)$. δf can be expanded in Fourier harmonics since it is a periodic function with respect to ψ.

$$\delta f(\psi, J; s) = \delta\left(\frac{\epsilon}{2} - J\right)\sum_{m=-\infty}^{\infty} g_m(s)\mathrm{e}^{im\psi}, \tag{B.11}$$

where $g_m(s)$ denotes the Fourier amplitude. We can obtain the following relation from Eqs (B.9) and (B.11).

$$\begin{gathered}\frac{dg_m}{d\theta} + im\nu_x g_m = -\frac{im\nu_x K_{\mathrm{sc}}}{2\pi\epsilon^{1/2}}\hat{\beta}_x^{3/2}\sum_{n=-\infty}^{\infty} F_{mn} g_n, \\ F_{mn} = \begin{cases} -\dfrac{32}{[(m-n)^2 - 1][(m+n)^2 + 1]} & \text{for} \quad m + n = \text{even} \\ 0 & \text{for} \quad m + n = \text{odd}. \end{cases}\end{gathered} \tag{B.12}$$

where the independent variable in now $\theta = \int dx/\nu_x\hat{\beta}_x$ with ν_x is the tune depressed by linear spaces charge force. Since $\hat{\beta}_x$ is a periodic function, the Floquet theorem provides the general solution

$$g_m(\theta) = \mathrm{e}^{-i\nu\theta} \sum_{\ell=-\infty}^{\infty} \hat{g}_m^{(\ell)} \mathrm{e}^{i\ell\theta} \ , \tag{B.13}$$

where ν is a constant. Then we reach the eigenvalue problem

$$\begin{cases} \displaystyle\sum_{n=-\infty}^{\infty} \sum_{\ell=-\infty}^{\infty} M_{mn}^{k\ell} \hat{g}_n^{(\ell)} = \nu \hat{g}_m^{(k)}, \\ M_{mn}^{k\ell} = (k + m\nu_x)\delta_{k\ell}\delta_{mn} + m\nu_x B_{k-\ell} F_{mn}, \\ \displaystyle B_k = \frac{K_{\mathrm{sc}}}{4\pi^2\epsilon^{1/2}} \int_0^{2\pi} \hat{\beta}_x^{3/2} \mathrm{e}^{-ik\theta}\, d\theta. \end{cases} \tag{B.14}$$

We may approximate the eigenvalue problem by considering only two modes $\hat{g}_{m_1}^{k_1}$ and $\hat{g}_{m_2}^{k_2}$ related to the resonant instability

$$\begin{pmatrix} k_1 + m_1\nu_x + m_1\nu_x B_0 F_{m_1m_1} & m_1\nu_x B_{k_1-k_2} F_{m_1m_2} \\ m_2\nu_x B_{k_2-k_1} F_{m_2m_1} & k_2 + m_2\nu_x + m_2\nu_x B_0 F_{m_2m_2} \end{pmatrix} \begin{pmatrix} \hat{g}_{m_1}^{(k_1)} \\ \hat{g}_{m_2}^{(k_2)} \end{pmatrix} = \nu \begin{pmatrix} \hat{g}_{m_1}^{(k_1)} \\ \hat{g}_{m_2}^{(k_2)} \end{pmatrix}. \tag{B.15}$$

We obtain the eigenvalue

$$\nu = \frac{1}{2}\left[(k_1 + m_1\nu_x + m_1\nu_x B_0 F_{m_1m_1}) + (k_2 + m_2\nu_x + m_2\nu_x B_0 F_{m_2m_2})\right] \pm \sqrt{D} \ , \tag{B.16}$$

where

$$\begin{aligned} D = \frac{1}{4}\left[(k_1 + m_1\nu_x + m_1\nu_x B_0 F_{m_1m_1}) - (k_2 + m_2\nu_x + m_2\nu_x B_0 F_{m_2m_2})\right]^2 \\ + m_1 m_2 |B_{k_1k_2}|^2 (\nu_x F_{m_1m_2})^2 \ . \end{aligned} \tag{B.17}$$

As is obvious from Eq. (B.13), $g_m(\theta)$ grows exponentially if the imaginary part of ν is not zero. Thus, the modes become unstable when D is negative. From Eq. (B.17) the range of the resonant depressed tune can be given by

$$\nu_c - \delta\nu_x < \nu_x < \nu_c + \delta\nu_x \ , \tag{B.18}$$

where

$$\begin{aligned} \nu_c &= -\frac{1}{m_1 - m_2}\left[k_1 - k_2 + \nu_x B_0 (m_1 F_{m_1m_1} - m_2 F_{m_2m_2})\right] , \\ \delta\nu_x &= \frac{2\nu_x\sqrt{|m_1 m_2|}}{|m_1 - m_2|} |B_{k_1-k_2}||F_{m_1-m_2}|. \end{aligned} \tag{B.19}$$

We can also solve Eq. (B.12) numerically. Taking the sinusoidal focusing model introduced in Chapter 3, Fig. B.1 shows the numerical integration of Eq. (B.12). The abscissa ν_{0x} is bare tune determined solely by K_x, and the tune depression $\eta_x \equiv \nu_x/\nu_{0x}$ is set at 0.8. $\mathrm{Im}(\nu)$ shown

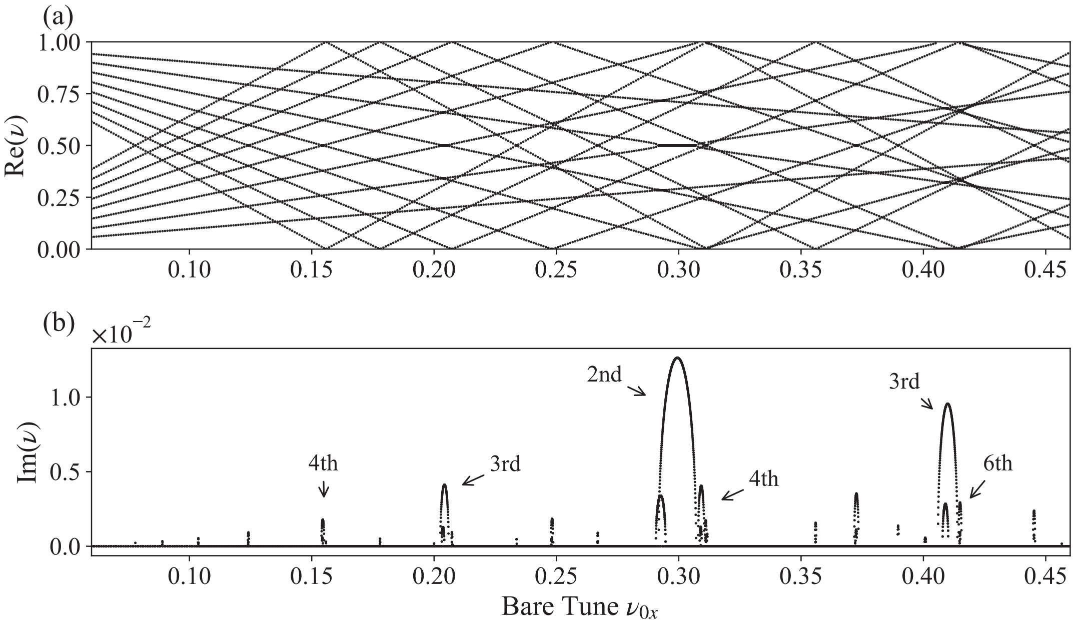

Figure B.1: Bare tune dependence of the eigenvalues numerical evaluated from Eq. (B.13) with the cutoff $m_c = 8$. The tune depression is maintained at 0.8.

in the lower panel locates the stopband position of the coherent instabilities.

By comparing the upper and lower panels in Fig. B.1, we can see that the severe instabilities are caused when the eigenvalues Re(ν) of the same orders approach each other. Thus, we focus on the case where $m_1 = -m_2 (\equiv m)$, and then the resonance condition can be given by

$$m\nu_x(1 + B_0 F_{mm}) = \frac{k}{2} \tag{B.20}$$

By taking the smooth aproximation to B_0, we can write the above resonance condition as

$$m[\nu_{0x} - C_m(1 - \eta_x)\nu_{0x}] \approx \frac{k}{2} \tag{B.21}$$

where $C_m = 1 - F_m/4\pi$. From Eq. (B.19), the band width can be approximately wirtten by

$$\delta\nu_x \approx (1 - C_m)\frac{1 - \eta_x}{\eta_x}\nu_{0x} \tag{B.22}$$

Appendix C

PIC method

The PIC method enables us to integrate the Hamiltonian self consistently taking into account the space charge effect in reasonable computing time. In order to avoid the direct calculation of Coulomb interaction, which needs processes of the square of the number of simulation particles, and shorten the computing time, the PIC method has a unique algorithm. The algorithm proceeds as follows with macro particles representing several hundreds of real particles and a mesh that covers whole the simulation region in real space.

(1) Assign the macro particles to the mesh grid and estimate the density profile in real space.

(2) Based on the density profile obtained in (1), solve Poisson's eq. numerically using the finite difference method.

(3) Update coordinates and velocities of each macro particle, taking into account the self and the external fields.

The processes are schematically shown in Fig. C.1. This indirect calculation of Coulomb repulsive force is superior to the direct calculation in that the number of processes increases roughly linearly with the number of macro particles. Considering that several millions of macro particles are used to describe the density profile with proper precision, this feature is essential to shorten the computing time.

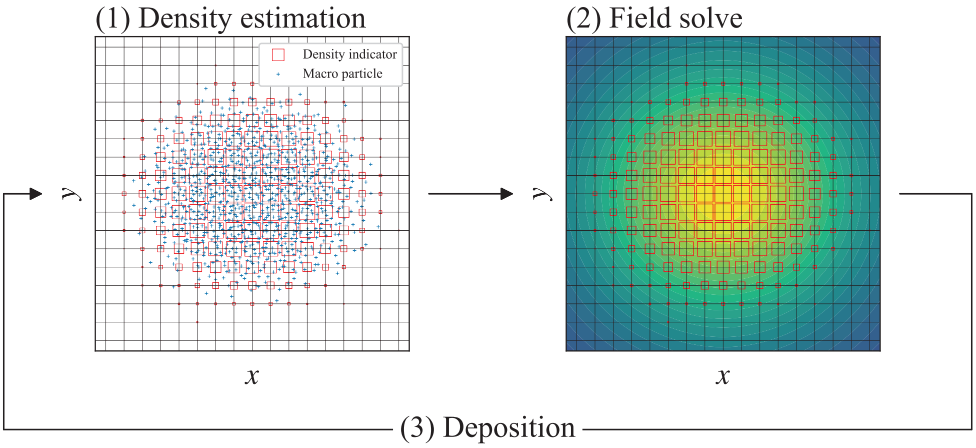

Figure C.1: Schematic of the PIC simulation.

The PIC method should not be adopted for extremely high-intensity beams such as Coulomb crystals, since Coulomb collisions can not be taken due to the algorithm (1). It can be seen by the following quantity whether Coulomb collisions predominate or not.

$$N_{\mathrm{D}} = \frac{4}{3}\pi \varrho_0 \lambda_{\mathrm{D}}^3, \tag{C.1}$$

where λ_{D} is the Debay length and ϱ_0 is the particle density. N_{D} represents the number of particles contained in a sphere of radius λ_{D}; to employ the PIC method, N_{D} must be much greater than one.

In order to guarantee high resolution and good statics of the PIC method, both the mesh size and the number of macro particles have to be optimized properly. The large mesh size relative to the beam radius leads to the deterioration of the resolution of density profile estimation. The insufficient number of macro particles also causes statistical noise in density profile estimation. It is, however, undesirable to waste computing time with too many macro particles or too small a mesh size. These simulation parameters thus should be carefully optimized to balance the accuracy of the calculation and the computing time [29].

Appendix D

Pseud-equilibrium 6-dimensional phase space distributions

We here outline the generalization of the pseudo-equilibrium concept proposed by Steven *et al.* to the 3D case [35, 71]. Similarly to the 2D case in Eq. (3.3), the piecewise constant focusing strength is defined as

$$\kappa_b = \frac{3\lambda_3\Gamma}{2a_b^3}\int_0^\infty \frac{d\zeta}{(1+\zeta)^{5/2}} + \frac{\varepsilon_b^2}{a_b^4}\,, \tag{D.1}$$

where $a_b = (l^3\beta_\mathrm{s}\hat{X}\hat{Y}\hat{T})^{1/3}|_{z=0}$ and $\varepsilon_b = (\varepsilon_x\varepsilon_y\varepsilon_z)^{1/3}$ are the initial rms beam radius and emittance averaged over three degrees of freedom, and $\hat{X}$, $\hat{Y}$, and $\hat{T}$ become a stationary solution of Eq. (4.18). We assume the Hamiltonian with κ_b as

$$H_b(x,y,z,p_x,p_y,p_z;s) = \frac{p_x^2+p_y^2+p_z^2}{2} + \frac{\kappa_b R^2}{2} + \frac{2\pi\epsilon_0\Gamma}{qN_p}\phi_\mathrm{sc}(R), \tag{D.2}$$

where $R = \sqrt{x^2+y^2+z^2}$, and N_p represents the number of particles per bunch. Then, the arbitrary function $f(H_b)$ satisfies the Vlasov equation and describes the stationary beam distribution, since H_b becomes a constant of motion. The self-field potential ϕ_sc of the stationary beam satisfies the Poisson's equation

$$\frac{1}{R^2}\frac{d}{dR}\left(R^2\frac{d}{dR}\phi_\mathrm{sc}\right) = -\frac{q}{\epsilon_0}\int\int\int f(H_b)dp_xdp_ydp_z. \tag{D.3}$$

We here, for example, consider the two types of distribution functions, namely, the thermal equilibrium (TE) and waterbag (WB), and their distribution functions are shown in Table 3.1. The combination of the distribution function and Eq. (D.3) gives

$$\frac{1}{\rho_\mathrm{TE}^2}\frac{d}{d\rho_\mathrm{TE}}\left(\rho_\mathrm{TE}^2\frac{d\psi}{d\rho_\mathrm{TE}}\right) = 1+\Delta-\exp(-\psi). \tag{D.4}$$

for the TE distribution with $\psi \equiv \kappa_b R^2/2 + 2\pi\epsilon_0\Gamma/qN_p\phi_\mathrm{sc}$ and $\Delta \equiv 3p_\mathrm{s}\beta_\mathrm{s}\gamma_\mathrm{s}^2 c\kappa_b\epsilon_0/q^2\varrho_0 - 1$. Here the radial coordinate R is scaled to be dimensionless with $\sqrt{T\epsilon_0/q^2\varrho_0}$; namely $\rho_\mathrm{TE} \equiv$

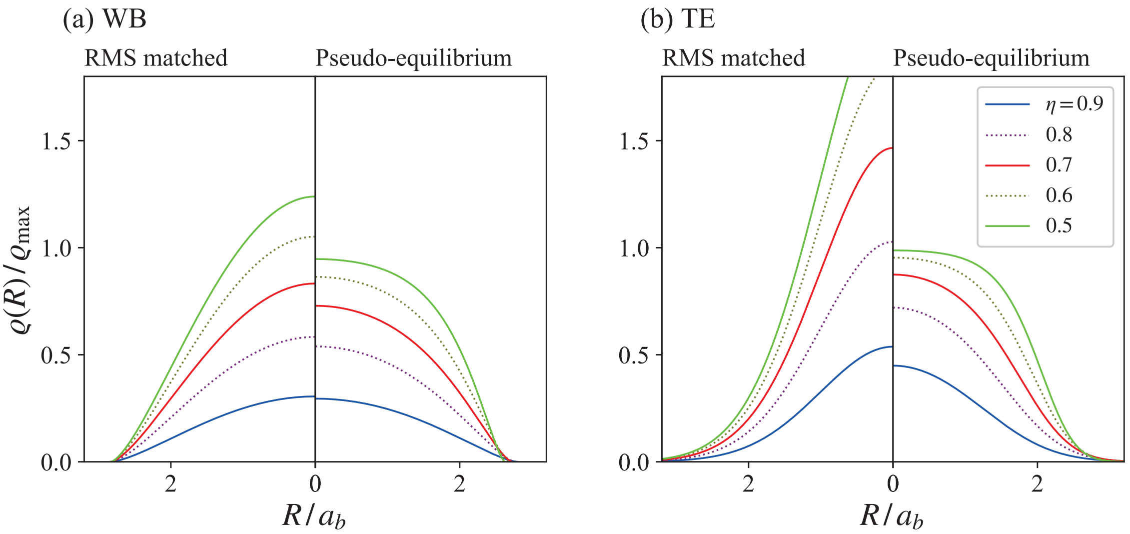

Figure D.1: Radial density profiles of the rms matched beams and spherical distributions given by $f(H_b)$.

$R/\sqrt{T\epsilon_0/q^2\varrho_0}$. Likewise, we obtain

$$\frac{d^2P}{d\rho_{\mathrm{WB}}^2}-\frac{1}{3P}\left(\frac{dP}{d\rho_{\mathrm{WB}}}\right)^2+\frac{2}{\rho_{\mathrm{WB}}}\frac{dP}{d\rho_{\mathrm{WB}}}=\frac{q^2\varrho_0 P^{4/3}}{3\kappa_b\epsilon_0 p_{\mathrm{s}}\beta_{\mathrm{s}}\gamma_{\mathrm{s}}^2 c}-P^{1/3}\,, \tag{D.5}$$

for the WB distribution with $P=\varrho(R)/\varrho_0$ and $r_{\mathrm{s}}=\sqrt{(3\varrho_0/4\pi f_0)^{2/3}/9\kappa_b}$. $\rho_{\mathrm{WB}}\equiv R/r_{\mathrm{s}}$ is a scaled radial coordinate. The set of two constants (T and ϱ_0 for TE, r_{s} and ϱ_0 for WB) can be chosen so that the rms radius and particle number given with $f(H_b)$ correspond to a_b and N respectively. Figure D.1 shows the R dependence of the density profile $\varrho(R)$ in real space. $\varrho_{\max}$ represents the maximum beam density given by

$$\varrho_{\max}=\frac{3qN_p\kappa_b}{2\pi\Gamma}\,. \tag{D.6}$$

In principle, the density profile of the rms matched beam is independent of the beam intensity. On the contrary, it is shown for pseudo-equilibrium distributions that the profiles are more homogenized because of the Debay screening effect as the beam gets higher intensity ($\eta\to 0$). Finally, the canonical variables of an individual particle are transformed so that 2nd-moments of the beam are adopted to the AG lattice at $s=0$ as follows:

$$\begin{aligned} w &\longrightarrow \left(\frac{\hat{a}_w}{a_b}\right)_{s=0} w,\\ p_w &\longrightarrow \left(\frac{a_b\varepsilon_w}{\hat{a}_w\varepsilon_b}\right)_{s=0} p_w+\left(\frac{1}{a_b}\frac{d\hat{a}_w}{ds}\right)_{s=0} w. \end{aligned} \tag{D.7}$$

where $\hat{a}_w$ is matched rms beam size in w direction. Needless to say, the pseudo equilibrium distribution is not a self-consistent solution to the Vlasov-Poisson system. Due to the approximation in Eq. (D.2), the mismatch of the pseudo-equilibrium distribution should be enhanced in a bunch whose aspect ratio is far from unity and also under the comparably strong AG focusing.

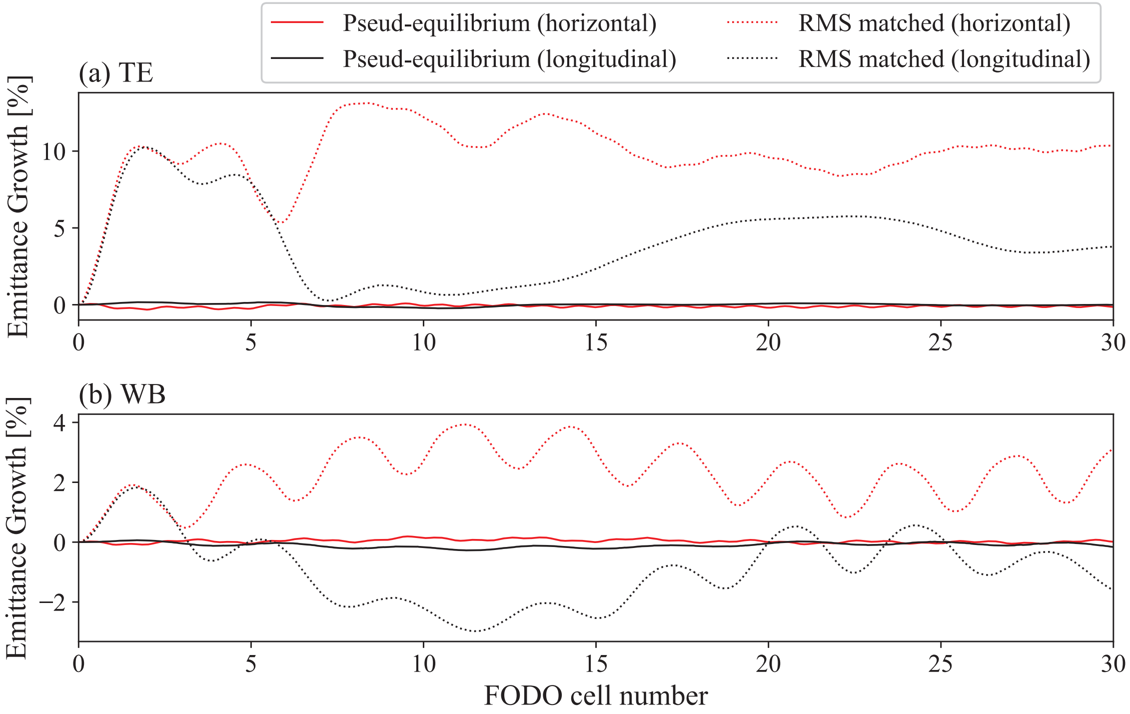

Figure D.2: Time evolution of the longitudinal and horizontal emittance growths.

Figure D.2 shows an example of the rms emittance evolution. For simplicity, the accelerating gradient is set at zero, and the operating point is kept at $(\mu_i, \sigma_i) = (39.8°, 32.4°)$ through the DTL. The other main parameters are listed in Table 4.1. Then, the initial horizontal and longitudinal tune depressions become 0.55 and 0.51 respectively. The emittances of rms matched beams jump considerably right after the injection. On the other hand, such an emittance jump is well suppressed in the case of pseudo-equilibrium beams.

The phase space distributions corresponding to the simulation in Fig. D.2 are shown in Figs. D.3 and D.4. Comparing the results in the left panel (a) for the rms matched beams to the results in the right panel (b) for pseudo-equilibrium beams, it is obvious that the pseudo-equilibrium beams are better adapted for both cases of TE and WB. The rms matched beams seem to be deformed into rectangle-like shapes due to the nonlinear nature of space charge force and redistributed into similar configurations of the pseudo equilibrium distributions.

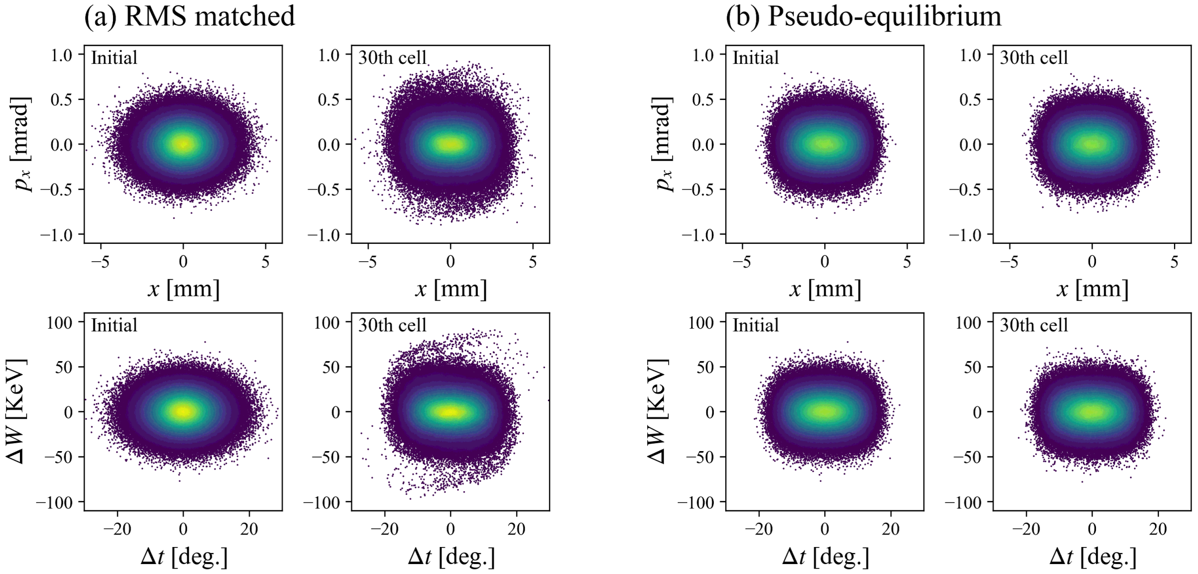
(a) RMS matched

(b) Pseudo-equilibrium

Figure D.3: Particle distributions in the horizontal and longitudinal phase space at the entrance and exit, corresponding to the simulations in Fig. D.2. The initial distribution is TE type.

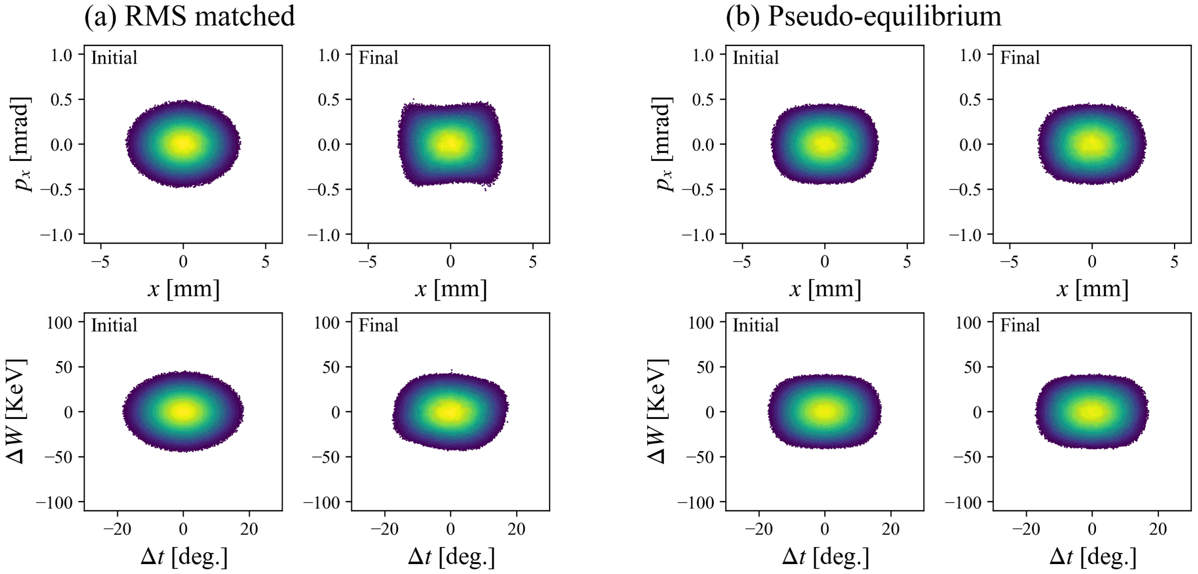
(a) RMS matched

(b) Pseudo-equilibrium

Figure D.4: Particle distributions in the horizontal and longitudinal phase space at the entrance and exit, corresponding to the simulations in Fig. D.2. The initial distribution is WB type.